UNIVERSIDADE FEDERAL DE MINAS GERAIS
INSTITUTO DE GEOCIÊNCIAS
PROGRAMA DE PÓS-GRADUAÇÃO EM GEOLOGIA

TESE DE DOUTORADO

Isotopic, fluid inclusion and LA-ICP-MS studies on the world-class Cuiabá gold deposit, Rio das Velhas greenstone belt, Quadrilátero Ferrífero, MG: implications for the mineralizing fluid reservoirs

AUTOR Carolin Kresse

ORIENTAÇÃO Lydia Maria Lobato

CO-ORIENTAÇÃO Rosaline C. Figueiredo e Silva; Steffen G. Hagemann

AREA DE CONCENTRAÇÃO Geologia Econômica e Aplicada

N° 40

BELO HORIZONTE
DATA (22/06/2018)

UNIVERSIDADE FEDERAL DE MINAS GERAIS
INSTITUTO DE GEOCIÊNCIAS
PROGRAMA DE PÓS-GRADUAÇÃO EM GEOLOGIA

TESE DE DOUTORADO

Isotopic, fluid inclusion and LA-ICP-MS studies on the world-class Cuiabá gold deposit, Rio das Velhas greenstone belt, Quadrilátero Ferrífero, MG: implications for the mineralizing fluid reservoirs

AUTOR Carolin Kresse

ORIENTAÇÃO Lydia Maria Lobato

AREA DE CONCENTRAÇÃO Geologia Econômica e Aplicada

N° 40

BELO HORIZONTE
DATA (22/06/18)

Tese de Doutorado

Isotopic, fluid inclusion and LA-ICP-MS studies on the world-class Cuiabá gold deposit, Rio das Velhas greenstone belt, Quadrilátero Ferrífero, MG: implications for the mineralizing fluid reservoirs

Estudos isotópicos, de inclusões fluidas e de LA-ICP-MS no depósito de classe mundial de ouro Cuiabá, greenstone belt Rio das Velhas, MG: implicações para os reservatórios de fluidos mineralizadores

Tese de doutoramento apresentada ao Programa de Pós-Graduação em Geologia do Instituto de Geociências da Universidade Federal de Minas Gerais.

Autor: MSc. Carolin Kresse

Orientador: Prof. Lydia Maria Lobato

Co-Orientador: Dr. Rosaline C. Figuerido e Silva

Prof. Steffen Hagemann

Belo Horizonte, Março 2019
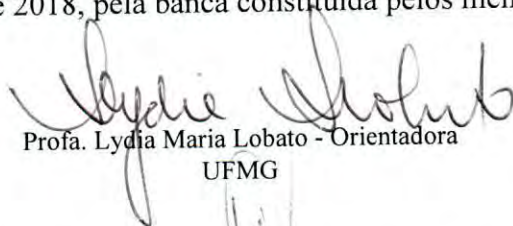
FOLHA DE APROVAÇÃO

Isotopic, fluid inclusion and LA-ICP-MS studies on the world-class Cuiabá gold deposit, Rio das Velhas greenstone belt, Quadrilátero Ferrífero, MG: implications for the mineralizing fluid reservoirs
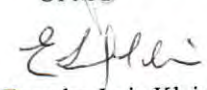
CAROLIN KRESSE

Tese submetida à Banca Examinadora designada pelo Colegiado do Programa de Pós-Graduação em GEOLOGIA, como requisito para obtenção do grau de Doutor em GEOLOGIA, área de concentração GEOLOGIA REGIONAL.

Aprovada em 22 de junho de 2018, pela banca constituída pelos membros:

Profa. Lydia Maria Lobato - Orientadora
UFMG

Prof. LUIS RODRIGUES ARMOA GARCIA
UFMG

Prof. Evandro Luiz Klein
Comp. Pesq. de Rec. Minerais//Serv. Geol. Brasil

Prof. Francisco Javier Rios
CDTN/CNEN

Profa. Lena Virgínia Soares Monteiro
USP

Belo Horizonte, 22 de junho de 2018.

Acknowledgment

Abstract

The world-class Cuiabá orogenic Au deposit in the Quadrilátero Ferrífero is hosted at the base of the Archean Rio das Velhas greenstone belt (RVGB) that contains an extensive volume of sedimentary rocks, being the largest underground mine in Brazil (5.78 Moz resources of 10.26 g/t). The main host to gold is a carbonaceous, carbonate banded iron formation (BIF), underlain by andesite and overlain by carbonaceous pelite (CP), along the reclined, isoclinal Cuiabá fold, with an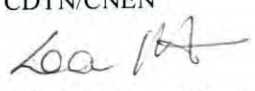 axis having a 116° azimuth dip direction and plunging between 35° and 12°. Andesite-hosted quartz vein mineralization constitutes recently discovered orebodies at the mine, and fluid inclusion data (microthermometry, Laser-raman, LA-ICP-MS, ion chromatography) of the VQZ orebody have constrained the physico-chemical nature of the ore-forming fluid. The data were obtained on quartz types (Qz1, Qz2, Qz3, Qz5) from veins classified in four main generations, V1 shear vein, and V2, V3, and V4 extensional veins (V1 and V2 mineralized), providing a chronological framework for the fluid evolutionary history. Three fluid types are distinguished: i) aqueous of low salinity (2-4 wt % NaCl equiv), mean homogenization temperature at 220°C; ii) aqueous of moderate salinity (6-12 wt % NaCl equiv), and mean homogenization temperature at ~260°C; and iii) aqueous-carbonic of moderate salinity (6-15 wt % NaCl equiv), with 30-91.4 mol. % CO_2 and 8.6-41.0 mol. % CH_4, and up 28 mol. % N_2 and mean decrepitation temperature at 300°C. Since only one fluid inclusion assemblage shows homogenization into vapour, and aqueous as well as aqueous-carbonic fluid inclusion assemblages are estimated to decrepitate into the vapor phase, supporting arguments for phase immiscibility are insignificant. As a result, temperature correction is applied, and calculated mean minimum trapping temperatures are 360°C in V1 shear veins, 330°C in V2 extensional veins, 300°C in V3 extensional array veins, and up to 270°C in late-stage V4 veins. All these temperatures are in the range of the arsenopyrite geothermometer calculated at 300 - 390°C. Ion chromatography analyses on Qz1-V1 veins reveal a Br/Cl range between 0.71 to 0.74 x 10^{-3}, 1.40 to 1.51 x 10^{-3} in Qz2-V2, 0.31 to 0.39 x 10^{-3} in Qz3-V3, and 0.73 to 0.85 x 10^{-3} in Qz5-V4 veins. Base metals (Zn, Pb and Cu) are relatively enriched in the order of 100 to 1,000 ppm in aqueous and aqueous-carbonic fluid inclusion assemblages trapped in all vein and quartz types at Cuiabá, similar to other orogenic gold deposits hosted in the Rio das Velhas greenstone belt. This sediment-rich greenstone belt may have acted as a potential base-metal source, explaining the elevated Zn and Pb signatures. Consideration of these physio-chemical fluid inclusion data indicates the compatibility with metamorphic fluids. Although geochemical and isotope analyses may implicate multiple fluid sources associated with the development of the Cuiabá deposit, the fluid inclusion data set does not differentiate them in an absolute sense. A two-step model of hydrothermal fluid flow and gold precipitation at the Cuiabá deposit is suggested to involve the development of the mineralised mineralized V1 shear veins up to V3 extensional array veins by an early- stage, aqueous-carbonic, high temperature fluid. It encompasses a minimum Th_{TRAP} at 290°C (Qz2-V3) to

maximum Th_{TRAP} at 360°C (Qz1-V1), and the V4 extensional veins associated with an evolved, aqueous-carbonic, lower temperature (mean Th_{TRAP} at 260°C), later-stage fluid, all developed during the Archaean D1 shear event. Fluid inclusion trapping mechanism and interpreted gold precipitation processes may include 1) intermittent phase immiscibilty, and 2) intermittent partial mixing of low and moderate saline, two or more fluids of aqueous and aqueous-carbonic nature.

Textural, chemical and multiple sulfur isotope analyses were conducted in sulfides from the BIF-hosted Fonte Grande Sul orebody to track distinct trace element (TE) signatures from syngenetic to epigenetic pyrite types in different host units, and to deduce the nature and source of the mineralizing fluids. Five pyrite types are classified based on textural relations as spongy, syngenetic (Py1, detected only in CP), porous early-(Py2, all 3 lithotypes), smooth main-(Py3, all 3 lithotypes) and smooth isolated and overgrown late-stage (Py4 and Py5, only BIF) variably present in metamorphosed CP, BIF and andesite. The TE abundance maps and LA-ICP-MS analyses display that Py1 yields high As, Co, Ni, Pb and Ag values, whereas Py2 (formed by agglomeration of Py1) maintains high TE with slightly less of those elements. The TE incorporation in Py3 is similar to Py1 in CP. The Py2 and Py3 in BIF and andesite have increased Co and Ni, but have less Au and As. BIF-hosted late-stage Py4 is characterized by lower TE concentrations, whereas Py5 is further enriched in As, Bi, Co, Ni and Pb. The study shows that CP is pre-enriched in Co, Ni and Pb, whereas certain elements like Ag, Au, Bi and As are only hydrothermally concentrated during advanced stages in BIF and andesite, supporting a syngenetic versus hydrothermal origin of distinct elements. Multiple sulfur isotopes suggest that mineralizing fluids reflect a complex mixing of sulfur evolved from three possible sources: seawater, mantle, and reduced elemental sulfur. Syngenetic Py1 yields $\Delta^{33}S$ values ranging from –2.28 to –0.25 ‰, separated into two ranges, (i) –2.28 to –1.97 ‰, (ii) –0.96 to –0.25 ‰, whereby (i) suggests the deposition in seawater environment. These pyrites probably mixed with later mantle sulfur or could have mixed with fluids sourced from sedimentary rocks at depth carrying a positive $\Delta^{33}S$ signature (ii). The second scenario is more common in sedimentary/diagenetic pyrite. Early-, main- and late-stage pyrites in CP, BIF and andesite present a continuous process of crustal assimilation towards positive $\delta^{34}S$ and $\Delta^{33}S$ values. This confirms evidence for a sedimentary-derived sulfur source as also indicated by FI data of the andesite-hosted VQZ orebody.

Finally we attempt to integrate the fluid-inclusion-based, two-step hydrothermal fluid evolution with that of the pyrite evolution at Cuiabá. Both Py2 and Py3 represent the peak of Archaean gold mineralization event, and considered part of the first hydrothermal pulse having evolved during the development of V2 and V3 veins, respectively. This takes into consideration: (i) higher As and Au concentrations in Py2 than in Py3; ii) lower As and Au in FIAs of V2 veins compared to V1 and V4 veins; and (iii) Ag values that increase in FIAs from V1/V2 to V3 veins, while Ag concentrations indicate a decreasing tendency from Py2 to Py3. Both Py4 and Py5 are attributed to the second hydrothermal pulse, and the non-

mineralized late-stage V4 veins by comparing the reverse trend of lower (decreasing) Pb and Mn concentrations in FIAs trapped in V4 and higher (increasing) Pb and Mn in Py5. Gold in FIAs in V4, and the lack of Au in BIF-hosted Py4 and Py5 suggest that Au remained in the fluid and its precipitation conditions were not attained at this stage.

Both studies show clear geochemical influences of the ore-forming fluid by the sedimentary units of the Archaean RVGB, indicated by 1) FIAs containing significant amounts of Pb and Zn; and 2) pyrite types that clearly demonstrate a sedimentary-derived sulfur signature.

Resumo

A jazida de classe mundial ouro orogênico Cuiabá, no Quadrilátero Ferrífero, encaixa-se na base do *greenstone belt* arqueano Rio das Velhas (RVGB) que inclui um volume extenso de rochas sedimentares. A principal rocha hospedeira do ouro é uma formação ferrifero bandada (FFB), carbonática e carbonosa, com andesito na base, recoberta por pelito carbonoso (CP), ao longo da dobra Cuiabá, que é reclinada e isoclinal. Corpos de minério recentemente descobertos na mina Cuiabá têm mineralização hospedada em andesito, e corpos associados a veios de quartzo. Estudos de inclusões fluidas (microtermometria, laser raman, LA-ICP-MS, cromatografia de ions) realizados no corpo de minério VQZ mostram a natureza físico-química do fluido responsável pela mineralização de ouro. Os dados foram obtidos em tipos de quartzo (Qz1, Qz2, Qz3, Qz5) das quatro gerações de veios (V1 controlados por zonas de cisalhamentos, V2 a V4 veios extensionais; sendo V1 e V2 mineralizados) que apresentam estrutura cronológica da história evolutiva do fluido hidrotermal. Foram encontrados três tipos de fluidos: i) aquoso de salinidade baixa (2-4 wt % NaCl equiv); temperatura de homogenização média de 220°C, ii) aquoso de salinidade moderada-alta (6-12 wt % NaCl equiv), temperatura de homogenização média de 260°C, e iii) aquo-carbônico de salinidade moderada (6-15 wt % NaCl equiv) com 30-91,4 mol. % CO_2 e 8,6-41.0 mol. % CH_4, até 28 mol. % N_2, e temperatura de homogenização média de 300°C. Considerando que apenas uma FIA mostra homogenização para a fase vapor, e FIAs aquosas e aquo-carbônicas são estimadas de decrepitar para a fase vapor, os argumentos para imiscibilidaden de fase são insignificantes. Como resultado, a correção de temperatura precisou ser aplicada, e as médias calculadas de temperatura mínima de aprisionamento ficam em 360°C para os veios de cisalhamento V1, 330°C para veios extensionais V2, 300°C para veios extensionais V3, e até 270°C para os veios tardios V4. Todas estas temperaturas estão na faixa do geotermômetro da arsenopirita, calculado entre 300 - 390°C. Análises de cromatografia iônica em Qz1-V1 revelam uma faixa de Br/Cl entre 0,71 a 0,74x10^{-3}, 1,40 a 1,51x10^{-3} em Qz2-V2, 0,31 a 0,39x10^{-3} em Qz3-V3, e 0,73 a 0,85x10^{-3} em Qz5-V4. Metais base (Zn, Pb e Cu) são relativamente enriquecidos, na ordem de 100 a 1.000 ppm, nas FIAs aquosas e aquo-carbônicas em todos os tipos de veios de quartzo em Cuiabá, similar a outros depósitos orogênicos de ouro hospedados no *greenstone belt* Rio das Velhas. O RVGB, rico em rochas sedimentares, pode ter atuado como potencial fonte desses metais base, explicando as assinaturas elevadas de Zn e Pb. Os dados físico-químicos das inclusões fluidas indicam compatibilidade com fluidos metamórficos. Embora análises geoquímicas e isotópicas possam implicar múltiplas fontes de fluidos associadas ao desenvolvimento da jazida Cuiabá, o conjunto de dados das inclusões fluidas não os diferenciam em sentido absoluto. Sugere-se que um modelo de dois estágios de fluxo de fluido hidrotermal e precipitação de ouro na jazida Cuiabá envolva desenvolvimento dos veios de cisalhamento V1 mineralizados até veios extensionais V3, por um fluido aquo-carbônico de alta temperatura em estágio inicial. Esse

envolve uma Th$_{TRAP}$ mínima de 290°C (Qz2-V3) até o máximo 360°C (Qz1-V1), enquanto os veios extensionais V4 são associados ao fluido de estágio tardio, aquo-carbônico evoluído, de temperatura baixa (Th$_{TRAP}$ médio a 260°C), sendo ambos desenvolvidos durante o evento arqueano D1. A interpretação acerca do mecanismo de aprisionamento por inclusões fluidas e precipitação de ouro podem incluir: 1) imiscibilidade intermitente de fase, e 2) mistura intermitente parcial de solução salina baixa a moderada, de dois ou mais fluidos de natureza aquosa e aquo-carbônica.

Estudos texturais, geoquímicos e múltiplos de isótopos de enxofre foram realizados em sulfetos do corpo de minério Fonte Grande Sul hospedado em FFB para monitar a assinatura de elementos traço em diferentes tipos de pirita nas rochas hospedeiras, de singenética a epigeneticas, para inferir a natureza e fonte do fluido mineralizado. Cinco tipos de piritas são classificadas com base em aspectos texturais em: esponjosa, singenética (Py1, apenas no pelito carbonoso-PC), cedo porosa (Py2, nos 3 litotipos), lisa principal (Py3, nos 3 litotipos), e lisas e isoladas, tardias (Py4 e Py5, apenas na FFB). Mapas de abundância de elementros traço mostram que a Py1 tem altas concentrações de As, Co, Ni, Pb e Ag, assim como Py2 (formada pela aglutinação da Py1 no PC). As Py2 e Py3 da FFB e do metandesito têm aumento de Co e Ni, mas menor Au e As. A Py4 é caracterizada por concentrações baixas de elementos traço, enquanto Py5 mostra novo enriquecimento. O estudo mostra que o CP é pré-enriquecido em Co, Ni e Pb, enquanto elementos determinados como Ag, Au, Bi e As são apenas concentrados hidrotermalmente durante estágios avançados na FFB e no andesito. Esse fato suporta origem singenética vs hidrotermal para elementos diferentes. Múltiplos isótopos de enxofre sugerem que os fluidos mineralizadores refletem mistura complexa de enxofre que evoluiu a partir de três fontes possíveis: água do mar, manto e enxofre elementar reduzido. A Py1 singenética do PC produz valores de Δ^{33}S variando de -2,28 a -0,25 ‰, separados em duas faixas: (i) -2,28 a -1,97 ‰, (ii) -0,96 a -0,25, sugerindo (i) deposição em ambiente marinho. Estas piritas provavelmente misturaram-se depois com enxofre mantélico, ou podem ter se misturado com fluidos provenientes de rochas sedimentares profundas de assinatura positiva de Δ^{33}S (ii). Esses segundo cenário é mais comum de se esperar para piritas sedimentares/diagenéticas. Piritas de estágio inicial, principal e tardio em CP, FFB e andesito indicam ter expwrimentado contínua assimilação crustal em direção a valores progressivamente mais positivos de δ^{34}S e Δ^{33}S. Isto confirma evidência de uma fonte de enxofre derivada de sedimentos, o que também é indicado pelos dados de inclusões fluidas obtidos no corpo de minério VQZ hospedado por andesito.

Finalmente deve-se tentar integrar a evolução proposta para do fluido hidrotermal, com base no estudo de incusões fluidas no corpo de minério de VQZ, com a evolução dos tipos de pirita do corpo de minério FGS hospedado por FFB em Cuiabá. Ambas Py2 e Py3 representam o evento de pico da mineralização arqueana, sendo considerado parte di primeiro puso hidrotermal que se desenvolveu durante a formação dos veios V2 e V3, respectivamente. Isso leva em consideração: (i)

concentrações mais altas de As e Au na Py2 do que na Py3; (ii) menores As e Au nas FIAs dos veios V2 em comparação aos veios V1 e V4; e (iii) valores de Ag que aumentam nas FIAs de V1/V2 a V3, enquanto que as concentrações de Ag indicam tendência decrescente de Py2 a Py3. Ambas Py4 e Py5 podem ser atribuídas ao segundo pulso hidrotermal, e aos veios V4 de estágio tardio não mineralizado comparando a tendência reversa de concentrações mais baixas (decrescentes) de Pb e Mn nas FIAs aprisionados em veios desse estágio final V4, com concentrações maiores (crescentes) de Pb e Mn nas Py5. Concentrações de ouro nas FIAs nos veios V4, e a ausência de Au nos tipos de Py4 e Py5 hospedados em FFB em estágio avançado sugerem que Au permaneceu no fluido e suas condições de recipitação não foram atingidas nesse estágio. Ambos os estudos mostram influência geoquímica claras do fluido mineralizador pelas unidades sedimentares do RVGB arqueano indicado i) por FIAs contendo quantidades significativas de Pb e Zn, 2) pelos tipos de pirita que demonstram claramente enxofre de derivação sedimentar.

Content

List of figures

Chapter 2

Chapter 3

List of tables

Chapter 2 : Updated with publication of 2020

Appendix tables

Chapter 3

Chapter 1

Introduction

Orogenic gold deposits are known for their variable host rocks, structures and geometries, and occur over a wide range of crustal depths from about three to more than 10 km (Groves et al., 1998). They show consistent chemical compositions of elevated Ag, As, Au, B, Bi, Sb, Te, and W (e.g., Goldfarb et al., 2005; Groves et al., 1998; Phillips and Groves, 1983). Typically shear-hosted deposits developed along strike-slip fault systems (Groves et al., 1998, 2000), and most of them are associated with greenschist facies rocks (Bierlein and Crowe, 2000).

The identification of the fluid sources for orogenic gold deposits is an enduring problem. Contrasting to other ore deposit types, where fluids have been identified from direct sampling of modern, active systems, it is not possible to sample fluids from actively forming orogenic gold systems. Nevertheless, extensive modern studies confirm the ubiquitous presence of low-salinity H_2O-CO_2 fluids associated with orogenic gold deposits (Yardley et al., 2014). Besides magmatic- and metamorphic-derived fluids (e.g., Kerrich and Fyfe, 1981), deeply circulating meteoric water (e.g., Nesbitt et al., 1986) have all also been suggested as the source of the ore-forming fluids, but a model based on fluids derived from metamorphic devolatilization has gained wide acceptance. According to Ridley and Diamond (2000), it remains difficult to differentiate between metamorphic dehydration-derived fluids or magmatic fluids derived from deep intrusions based only on fluid inclusion studies from orogenic Au deposits. Therefore, investigations of host rocks and ore minerals associated with the mineralization may provide detailed information on metal associations in sulfide minerals and the source of the mineralizing fluid.

The world-class Cuiabá orogenic Au deposit, located in the northern part of the Quadrilátero Ferrífero district (QF), near the town of Sabará, southeastern Brazil, is hosted in banded iron formation (BIF). The QF is an area of approximately 7,000 square kilometers centered about latitude 20" 15' S and longitude 43 O 30' W in the Brazilian state of Minas Gerais (Dorr, 1969). As of 2015, it has produced five million ounces (Moz), with a further 7 Moz in reserve (AGA, personal communication), making it the largest gold deposit in the QF. According to AGA, the deposit produces 1.2 million tonnes of ore per year, with an average grade of 7.96 g/t Au, and by-product Ag and H_2SO_4. The district is famous for its gold deposits hosted in an Archean greenstone belt sequence (RVGB), and its iron deposits within a Lower Proterozoic clastic-chemical sedimentary unit displaying Lake Superior-type BIF sequences (Minas Supergroup). The RVGB is special insofar that it is dominated by clastic, clastic-chemical and volcaniclastic sedimentary rocks (Baltazar and Zucchetti, 2007).

Despite the voluminous material of research on Cuiabá, questions regarding its genesis remain. For the preparation of this work, contributions by Ribeiro-Rodgrigues (1998), Costa (2000), Martins (2000), Lobato et al. (2001a, b, c) and Ribeiro-Rodgrigues et al. (2007) were the main source of information throughout. Most of these address structural, petrographic, and geochemical studies, although fluid inclusion on BIF-hosted ores, and isotope data (stable and radiogenic) are also provided by some.

To advance on the question of genesis, this work covers systematic studies on fluid inclusions and sulfide minerals, integrating these data to contemplate a fluid model for Cuiabá, which may perhaps be extended to other Archean-hosted gold deposits of the QF.

The present thesis is presented in form of two publications. The first comprises the comprehensive fluid inclusion study of the andesite-hosted VQZ orebody. The second work considers the investigated BIF-hosted FGS orebody, including detailed sulfide mineral and multiple sulfur isotope studies. In the final discussion and conclusion, both studies are linked to show their importance for the Cuiabá orogenic Au deposit.

i. Motivation and Background

Although, the Cuiabá orogenic Au deposit is studied by many authors in past years, a systematic fluid inclusion study including LA-ICP-MS analyses, and a detailed geochemical and isotopic study on sulfide minerals substantially contribute to the understanding of the hydrothermal fluid evolution and gold mineralization at Cuiabá.

The PhD project emphasizes the Fonte Grande Sul (FGS) Footwall and VQZ orebody of the Cuiabá deposit. The andesite-hosted VQZ orebody with its detailed quartz vein classification by Vitorino et al. (2017) supplies a thorough basis for extensive fluid inclusion studies and interpretation. Detailed quartz and fluid inclusion petrography are essential for microthermometry and LA-ICP-MS studies to integrate these results in relation to the ore-forming fluid. The interesting aspects regarding the FGS orebody is the presence of gold-hosting massive sulfide orebodies associated with BIF, andesite and carbonaceous pelites. Description including mineral paragenesis and textural features of main sulfide minerals such as pyrite, pyrrhotite and arsenopyrite is required. This part includes basic macroscopically and microscopically petrography, electron microprobe mapping, LA-ICP-MS analyses on sulfides and multiple sulfur isotope studies. The combination of modern analytical methods with results from both orebodies help constrain the metal source and fluid reservoir to felsic magmas, mantle-sourced, or metamorphic fluids. Further, multiple sulfur isotope analyses support to constrain the sulfur source as essential processes such as mixing and interaction with the mantle, crustal magmas, hydrothermal fluids, and

country rocks control isotopic signatures, and result in sulfide minerals with variable sulfur isotope compositions. Findings of both studies build up a framework for the developement of the Cuiabá orogenic Au deposit.

ii.   Detailed methical description of Secondary Ion Mass Spectroscopy (SIMS)

The advance of in situ analytical techniques using large geometry secondary ion mass spectrometry (SIMS; see Farquhar et al., 2013; Ireland et al., 2014; Ushikubo et al., 2014; Whitehouse, 2013) allows high-precision isotopic analysis of multiple sulfur isotopes with spot sizes nearing ten microns. Since data on some sulfur isotopes are still relatively new in metallogenetic studies, particularly orogenic gold, a brief review on this technique is presented.

Due to its ultra-high sensitivity, it is possible to measure the least common stable isotopes of sulfur, ^{33}S (0.75%) and ^{36}S (0.02%), together with the more abundant ^{32}S (95.02%) and ^{34}S (4.21%) isotopes, simultaneously, and enables to identify anomalous sulfur isotopic signatures, indicating mass independent fractionation process (MIF; $\Delta^{33}S$ and $\Delta^{36}S$) together with $\delta^{34}S$. Deviations from mass dependent fractionation (MDF) are typically caused by the presence of an oxygen-poor atmosphere that existed before the Great Oxidation Event at ca. 2.4 Ga in which ultraviolet radiation was the driver for mass independent photochemical separation of sulfur isotopes (e.g., Farquhar et al., 2000; Farquhar and Wing, 2003). For this reason, the measure of ^{33}S has become essential to evaluate the full suite of isotopic features of Archean rocks (e.g., Bühn et al., 2012; Farquhar et al., 2013), and those from younger terranes that might be sourcing Archean rocks (e.g., Cabral et al., 2013). The least abundant ^{36}S sulfur isotope behaves similarly to ^{33}S, and has also become important for fingerprinting Archean source rocks and understanding early Earth processes. The $\Delta^{36}S/\Delta^{33}S$ ratio can elucidate between MDFV and contributions from Archean MIF sources when magnitudes of MDF deviations are small (Farquhar et al., 2007; Johnston, 2011).

In-situ sulfur isotope measurements require careful standardization against a suitable matrix-matched reference material (Eiler et al., 1997; Stern, 2008). The majority of reference materials for analysing in-situ 3- or 4-sulfur isotopes have been acquired from the most common sulphide mineral, pyrite (Whitehouse, 2013; Ushikubo et al., 2014; Hauri et al., 2016). With growing interest in the application of in-situ sulfur isotope analysis to variable mineral systems, there is an increased need for reference material for a variety of common sulfide minerals, which presently remain scarce.

For sample preparation, sample mounts were made by coring 3 mm diameter pucks from rock fragments using a drill press fitted with diamond drill bits, then mounted and cast in the central portion of a 25 mm in diameter epoxy mount (LaFlamme et al., 2016). Standard blocks were made by mounting 1–2 grain fragments of pyrite, and 1mm diameter pucks of rock fragments host to pyrrhotite. Reference materials were cast in epoxy ~8 mm from the edge of a mount. Sample

mounts and standard blocks were trimmed to a thickness of 5 mm using a precision saw, coated with 30 nm of gold, and mounted together (after being appropriately trimmed) in the sample holder. It is important to set the surfaces of the standard and sample blocks at the same level in the sample holder. If necessary, a small amount of carbon paint has to be applied to provide good conductivity between both pieces. To ensure that results are not a product of analytical artefacts due to X-Y-Z positioning, a reference material is also mounted and cast with the sample block to compare with values generated from the standard block.

In the present PhD study, in-situ sulfur isotope ratios were measured using a CAMECA IMS-1280, and Sierra pyrite ($FeS2$) and Alexo pyrrhotite ($Fe(1-x)S$) as standard reference materials. The detailed measurement conditions are described in chapter 3 included in the work "Sulfur isotope and metal variations in sulphides in the BIF-hosted orogenic Cuiabá gold deposit, Brazil: implications for the hydrothermal evolution".

Data processing and error propagation of SIMS measurements is detailed described by LaFlamme et al. (2016) in two steps. At first, the Sierra pyrite standard is analysed once every five to eight analyses, regardless of whether the pyrite is being used as the primary standard for that particular session, allowing for the assessment of the stability of the instrument during the given analytical session, and correct for instrumental drift. At the second step, sample isotopic ratios are corrected for instrumental mass fractionation using the correction factor α, determined by normalising the mean of all measurements on the matrix matched reference material, R_{std}, to the isotopic ratio of the reference material R_{RM} as obtained by independent bulk methods (e.g. fluorination gas-source mass spectrometry). The propagated uncertainty for the $\delta^x S$ value of each sample spot takes into account the internal error on the raw isotopic ratios, the uncertainty on the drift correction where necessary and the uncertainty on the standard measurement, calculated as the standard deviation on the mean isotopic ratios measured in the standards.

ARTICLE

Fluid signature of the shear zone–controlled Veio de Quartzo ore body in the world-class BIF-hosted Cuiabá gold deposit, Archaean Rio das Velhas greenstone belt, Brazil: a fluid inclusion study

Carolin Kresse [1,2] · Lydia M. Lobato [2] · Rosaline C. Figueiredo e Silva [2] · Steffen G. Hagemann [3] · David Banks [4] · André L. A. Vitorino [2]

Abstract

The world-class Cuiabá gold deposit of the Archaean Rio das Velhas greenstone belt in Brazil is hosted in banded iron formation containing carbonaceous matter and carbonate, within the reclined, isoclinal Cuiabá fold. Mineralised quartz veins are hosted in andesite in the stratigraphic footwall of the banded iron ores and form some of the more recently discovered ore bodies. Fluid inclusion data of the quartz vein–associated "Veio de Quartzo" ore body are obtained from four quartz types (Qz1, Qz2, Qz3, Qz5) in gold-mineralised V1 shear vein and V2 extensional veins, barren V3 extensional vein array, and V4 breccia-style veins, all developed during the Archaean D1 event. Three fluid types are distinguished: (i) aqueous fluids of low salinity (1.8–3.8 wt% NaCl equiv), homogenisation (into liquid) at 220 to 230 °C; (ii) aqueous fluids of moderate salinity (5.3–12.7 wt% NaCl equiv), and homogenisation at 250 to 290 °C; and (iii) aqueous-carbonic fluids of moderate salinity (6.0–15.1 wt% NaCl equiv), with 30–91 mol% CO_2, 8–41 mol% CH_4 and up to 28 mol% N_2 and decrepitation (into vapour) at 280 to 310 °C. Based on an independent pressure estimate, a pressure correction was applied to aqueous fluid inclusions, resulting in minimum trapping temperatures at 360 °C for V1 veins, 330 °C for V2 veins, 300 °C for V3 veins and 270 °C for the late-stage V4 veins. Ion chromatography analyses reveal a Br/Cl ratio of 0.7×10^{-3} in Qz1-V1, from 1.4 to 1.5×10^{-3} in Qz2-V2, 0.3 to 0.4×10^{-3} in Qz3-V3 and 0.7 to 0.9×10^{-3} in Qz5-V4 veins. Zinc, Pb and Cu are relatively enriched with ~ 100 to 1000 ppm in aqueous and aqueous-carbonic fluid inclusion assemblages in all vein and quartz types, which is similar to other orogenic gold deposits hosted in the Rio das Velhas greenstone belt. The fluid inclusion data are consistent with a model invoking a metamorphic origin for the mineralising fluid. A two-step model of hydrothermal fluid flow and gold enrichment is suggested to have developed during the Archaean D1 event, with an early, aqueous-carbonic fluid pulse of relatively high temperature (from V1 up to V3) and an evolved, aqueous-carbonic fluid pulse of lower temperature (V4, breccia-style veins). The Rio das Velhas greenstone belt is dominated by regionally metamorphosed metasedimentary rocks, resulting in a complex hydrothermal fluid evolution and related gold mineralisation such as the shear zone–controlled Veio de Quartzo ore body.

✉ Carolin Kresse
  cakres@bgs.ac.uk

[1] British Geological Survey, Environmental Science Centre, Keyworth, Nottingham NG12 5GG, UK

[2] Instituto de Geociências, Universidade Federal de Minas Gerais, Belo Horizonte, Brazil

[3] Centre for Exploration Targeting, School of Earth and Environmental Sciences, University of Western Australia, Perth, Australia

[4] School of Earth and Environment, University of Leeds, Leeds, UK

⬡ Springer

Introduction

Orogenic lode-gold deposits are hosted in metamorphic terranes that typically contain rocks of lower to upper greenschist facies metamorphic grade (Groves et al. 1998). Textural and structural relationships are commonly well preserved allowing important constraints on the deposit formation. Fluid inclusion studies, summarised by Ridley and Diamond (2000) and Goldfarb and Groves (2015), suggest that ore formation occurred from aqueous-carbonic, CO_2/CH_4 fluids of low to moderate salinities. The source of gold is still debated (Goldfarb and Groves 2015). As pointed out by Gaboury (2013, 2019), the record of aqueous-carbonic and hydrocarbon gases in fluids from orogenic gold deposits confirms that organic matter–rich sedimentary rocks, containing possible gold-bearing pyrite, could be in part the source for gold in many world-class gold deposits. However, sedimentary rocks only form a small proportion of most Archaean greenstone belts (Goldfarb and Groves 2015). Compositional microanalysis of fluid inclusions using laser ablation inductively coupled plasma-mass spectroscopy (LA-ICP-MS) has the potential to provide new information on the origin and evolution

of crustal fluids (Marsala et al. 2013; Rauchenstein-Martinek et al. 2014, 2016; Morales et al. 2016; Wagner et al. 2016; Fusswinkel et al. 2017).

The Quadrilátero Ferrífero (QF) region is one of Brazil's most important gold provinces (e.g., Lobato et al. 2001a, b) and hosts a range of Archaean to Cainozoic gold deposits. The most productive deposits are hosted in banded iron formations (BIF) of the Archaean Rio das Velhas greenstone belt (Lobato et al. 2014) (Fig. 1). Some of the largest gold deposits, including Morro Velho, Cuiabá, São Bento, and Raposos, are located in the basal unit of this greenstone belt, referred to as the Nova Lima Group (Ladeira 1991; Vieira 1991; Lobato et al. 1998). The Cuiabá deposit, situated ~40 km northeast of Belo Horizonte (Fig. 1), is presently the major gold producer in the QF. The total of the Cuiabá mine's mineral resources, considering measured, indicated, and inferred resources, is 19.7 million tonnes grading 10.58 g/t Au (AngloGold Ashanti 2018).

Previous fluid inclusion studies of orogenic gold deposits hosted in the Rio das Velhas greenstone belt included those by Xavier et al. (2000), Lobato et al. (2001a, b, c), Ribeiro et al. (2015) and Morales et al. (2016). The study by Xavier et al. (2000) showed that the mineralising fluids were dominantly
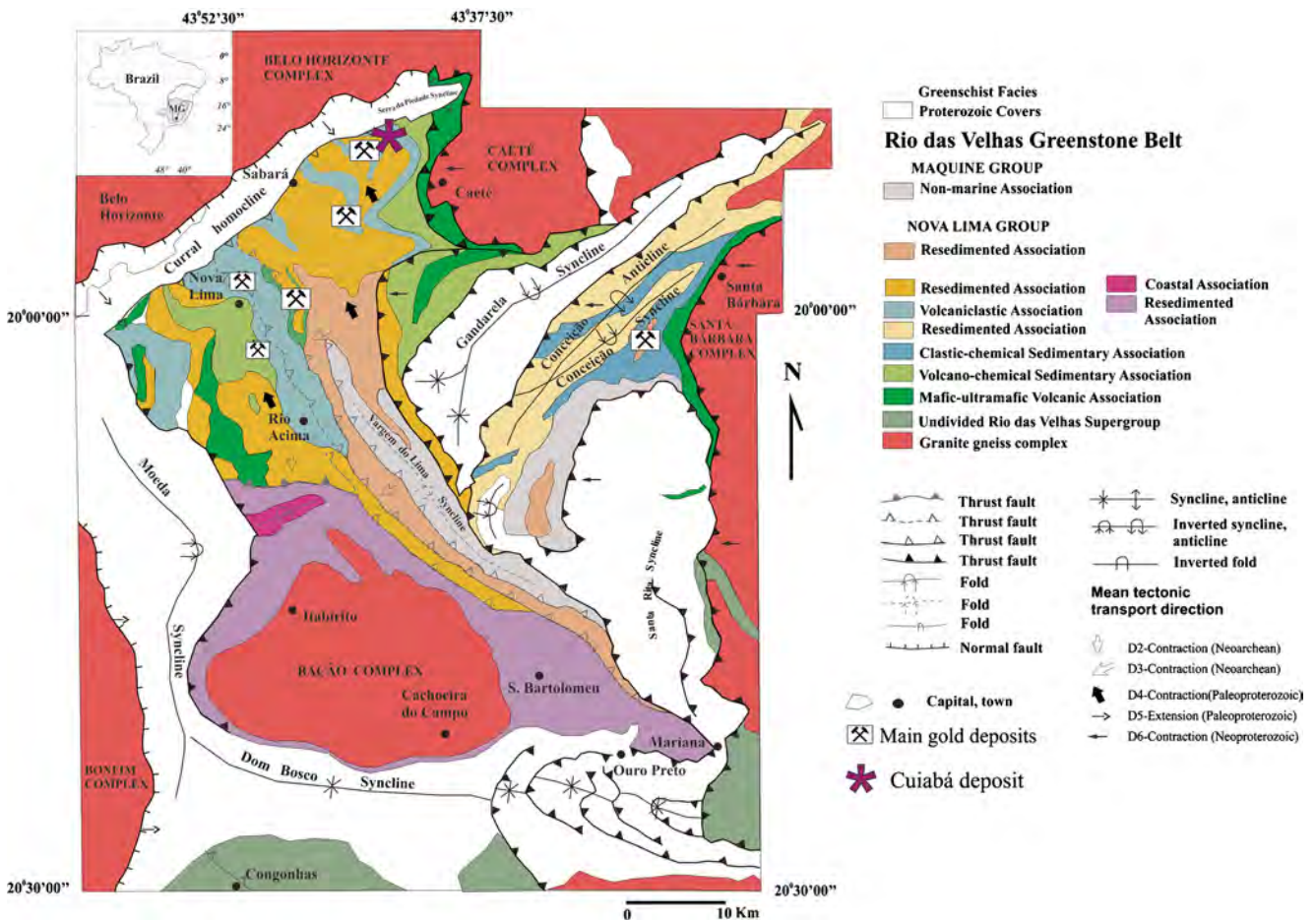
Fig. 1 Geological map of the Quadrilátero Ferrífero region. The inset shows the location of the Quadrilátero Ferrífero in Brazil (modified after Baltazar and Zucchetti 2007)

aqueous with a low salinity (3.0–6.0 wt% NaCl equiv) and variable concentrations of CO_2 (0–11.4 mol%), CH_4 (1.5–10.2 mol%), subordinate N_2 (0–0.7 mol%) and traces of H_2S and/or HS. The work of Lobato et al. (2001a, b, c) noted the occurrence of aqueous and aqueous-carbonic fluid inclusions with salinities ranging from 1.4 to 12.8 wt% NaCl equiv. and inconsistent volatile compositions of CO_2 (3.5–90.5 mol%), CH_4 (64.0–94.5 mol%), N_2 (1.5–21.5 mol%) and H_2S (~ 1.3 mol%).

This contribution reports on a study conducted to determine the chemistry of the hydrothermal fluids that formed the quartz vein–associated, andesite-hosted ore bodies at the Cuiabá gold deposit. In contrast to previous studies, fluid inclusion assemblages (FIAs) were studied to provide meaningful fluid inclusion data, as well as new geochemical data obtained by LA-ICP-MS. Based on the vein and quartz classification, new fluid inclusion data and spectroscopic investigations provide critical information on the mineralising processes at this world-class deposit.

Geology of the Quadrilátero Ferrífero including the Rio das Velhas greenstone belt

The Quadrilátero Ferrífero (QF) is located in the southern São Francisco Craton (Dorr 1969) and encompasses Archaean gneissic trondhjemite-tonalite-granodiorite (TTG) terranes, Archaean granite-greenstone belts of the Rio das Velhas Supergroup, and Proterozoic sedimentary units of the Minas and Espinhaço Supergroups (Dorr 1969; Toledo 1997; Noce 2013). Banded migmatite gneisses make up the largest proportion of the crystalline basement of the QF. They comprise four main lithostructural domains, consisting of 3.2 Ga granitoid gneisses and minor sedimentary rocks, which are intruded by 2.8–2.7 Ga old tonalites, andesites, granites, pegmatites and Proterozoic mafic dikes (Noce et al. 2005; Moreira et al. 2016).

The Rio das Velhas Supergroup contains the Archaean Rio das Velhas greenstone belt (3.0–2.7 Ga; Machado et al. 1989) which comprises the Nova Lima Group at the base and the overlying Maquiné Group (Fig. 1). The greenstone belt rocks are regionally metamorphosed to lower greenschist facies. The lower portion of the Nova Lima Group is composed of lower komatiitic to tholeiitic volcanic rocks interlayered with clastic and exhalative chemical sedimentary rocks (Vieira 1988). The middle mafic and felsic volcanic rocks are interlayered with carbonaceous sedimentary rocks, and BIF with felsic volcaniclastic rocks on the top. Clastic sedimentary rocks interlayered with mafic and felsic volcaniclastic rocks form the upper portion of the Nova Lima Group (Fig. 1). Radiometric ages (U-Pb SHRIMP) of detrital zircons yield a minimum age of 2.74 Ga for the volcaniclastic rocks (Schrank and Machado 1996; Lobato et al. 2001a).

The Paleoproterozoic Minas Supergroup (2.6–2.1 Ga; Babinski et al. 1991) represents a continental margin sequence and comprises clastic and chemical sedimentary rocks. More recently, however, Cabral et al. (2012) dated zircons (U-Pb LA-ICP-MS) from a volcanic layer within Minas Supergroup iron formation and proposed a 2.65 Ga Neoarchaean age for the deposition of these rocks.

Geology of the Cuiabá gold deposit

The Cuiabá deposit is an Archaean (U-Pb SHRIMP age of 2672 ± 14 Ma on monazite; Lobato et al. 2007) gold deposit, presently exploited in an underground mine. The host rock succession was first defined by Vial (1980) and consists of volcanic, volcaniclastic and sedimentary rocks that form part of the Nova Lima Group (Ladeira 1991).

At Cuiabá, the lowermost stratigraphic unit is characterised by alternating units of chloritized, mafic volcanic, and pelitic rocks, which are carbonate and sericite altered (Fig. 2c, ESM-1), as well as interbedded lenses of carbonaceous pelite. The volcanic and pelitic rocks are overlain by the Algoma-type Cuiabá BIF. The Cuiabá BIF consists of rhythmic alternation of dark, white, and ocher-coloured, millimetre- to centimetre-thick bands, rich in carbonaceous matter and fine-grained quartz and carbonate (ESM-1). Its lower portion is typically banded and rich in Fe carbonate and carbonaceous matter. The upper portion, separated by a 15-cm-thick mafic volcanic unit, is a highly deformed ferruginous chert also containing carbonaceous matter. Overlying these chemical sedimentary rocks is an upper mafic volcanic unit that displays a similar mineralogical composition as the lower, chloritized mafic volcanic rocks. Metamorphosed andesite at Cuiabá consists of albite, epidote, zoisite (clinozoisite), quartz, actinolite, carbonate and chlorite (Vieira 1991). The rocks are characterised by a light green colour and a fine-grain size, and are massive or foliated (ESM-1). The absence of hornblende indicates that peak metamorphic conditions did not exceed the greenschist-amphibolite facies transition (Spear 1995). This mineral assemblage is characteristic of metamorphic temperatures of 350 to 450 °C and is stable over a large pressure range of up to 4 kbars (Spear 1995). The stratigraphic column is completed by an ~ 1000-m-thick section of volcaniclastic rocks (Vieira 1991; Lobato et al. 1998; Xavier et al. 2000).

Structural setting

The rocks at the Cuiabá deposit underwent at least three deformation events (Ribeiro-Rodrigues et al. 2007). The first two, D1 and D2, developed under ductile to ductile-brittle conditions of SE-NW-directed compressive stress, with tectonic transport from SE to NW. The brittle-ductile D3 structures were formed due to E-W-oriented compressive stress (Ribeiro-
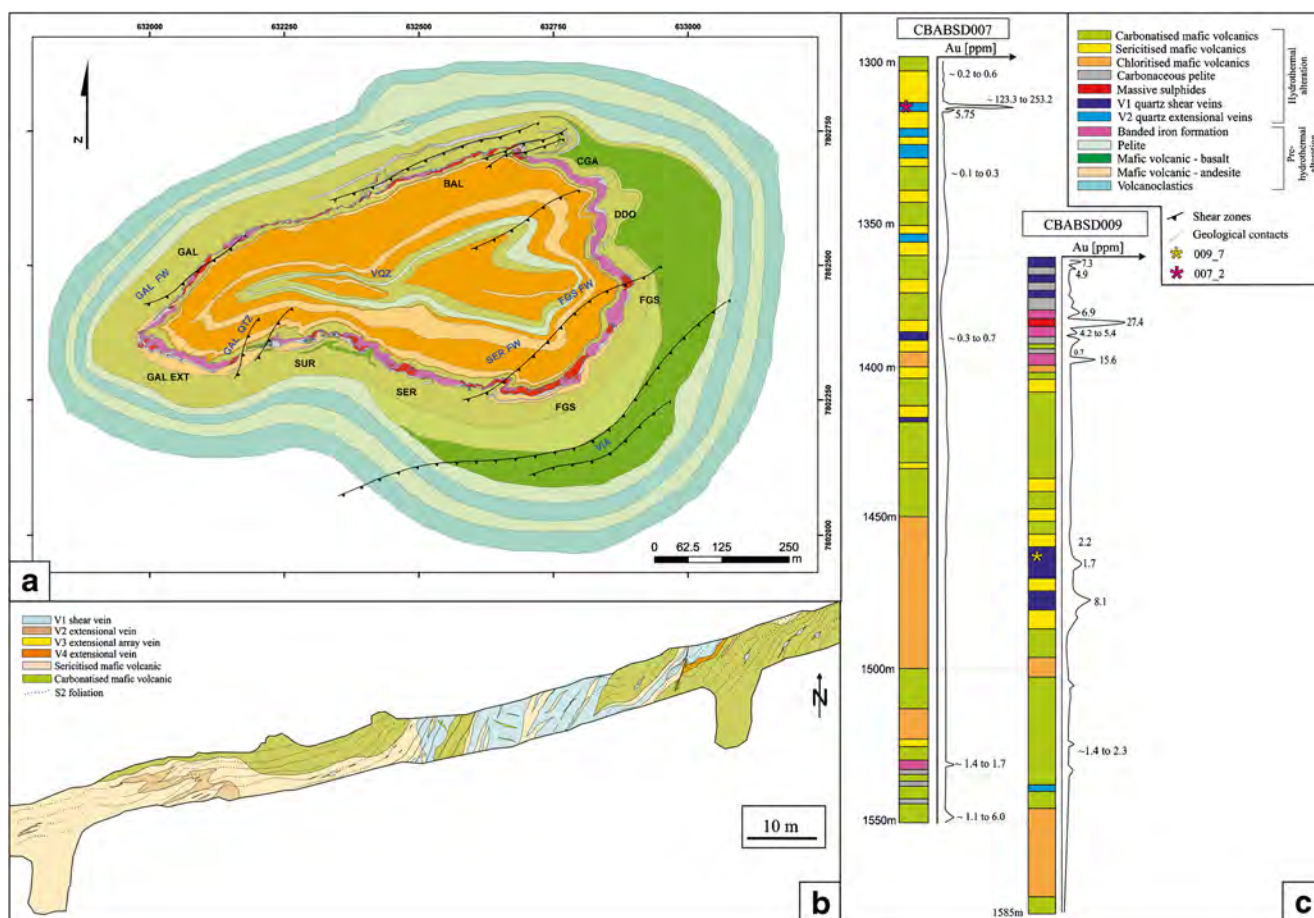
Fig. 2 Geology of the Cuiabá mine. **a** Geological map of the Cuiabá mine, Level 11, with location of the main orebodies. **b** Geological map of the VQZ orebody at Level 15. **c** Lithostratigraphic section of sampled drill cores with corresponding gold grades in ppm) (information provided by AngloGold Ashanti. Legend in **b** also valid for **a**. Abbreviations: BIF-hosted orebodies: FGS Fonte Grande Sul, SER Serrotinho, BAL Balancão, GAL Galinheiro, GAL EXT Galinheiro extenção, DDO Dom Domingos, CGA Cantagalo, SUR Surucu. Quartz vein–hosted bodies: VQZ Veio de Quartzo, GAL FW Galinheiro Footwall, Gal QTZ Galinheiro Quartzo, SER FW Serrotinho Footwall, FGS FW Fonte Grande Sul Footwall, VIA Viana

Rodrigues et al. 2007). All lithological units are overprinted by a pervasive axial planar foliation that is locally mylonitic (S_m = 135/45). They show a prominent mineral stretching lineation (LS = 126/22–35) indicated by the preferred orientation of elongated sericite, carbonates, and sulphide minerals. Late, northwest-verging, sigmoidal thrust faults reactivated pre-existing structures and caused folding, boudinage, and rotation of the host rocks of the Cuiabá deposit (Vitorino 2017).

The Cuiabá fold is an anticline with the rock succession inverted along the north limb (Fig. 2a). The N116° fold axis plunges from 35° in the upper portion to 12° below level 18. The plunge direction controls the geometry of the mineralised ore bodies. Studies by Vial (1980), Toledo (1997), Ribeiro-Rodrigues (1998) and Ribeiro-Rodrigues et al. (2007) considered the Cuiabá fold as a tubular structure, plunging southeast at 30°. Recently published data for the nearby Lamego gold deposit (Fig. 1) suggests that its fold geometry, which is comparable to that of the Cuiabá fold, represents a reclined, isoclinal, cylindrical and rootless fold (Martins et al. 2016).

Gold mineralisation

Gold mineralisation at Cuiabá is contained in six main BIF-hosted ore bodies (> 4 g/t Au) referred to as Balancão, Cantagalo, Fonte Grande, Fonte Grande Sul (FGS), Serrotinho, and Galinheiro (Fig. 2a). These ore bodies represent sulphide-rich segments of the Cuiabá BIF grading laterally into non-economic or barren iron formation. Quartz vein–hosted ore bodies are named Veio de Quartzo (VQZ), Galinheiro Footwall (GAL FW), Serrotinho Footwall (SER FW) and FGS Footwall (FGS FW) (Fig. 2). The three main mineralisation styles are (i) stratabound replacement with locally massive ores, commonly in BIF, (ii) disseminated in volcanic and sedimentary rocks, related to hydrothermal alteration in shear zones and (iii) quartz-carbonate-sulphide vein hosted, related to shear zone in volcanic and sedimentary rocks (Ribeiro-Rodrigues et al. 2007).

Decreases in gold grade from over 60 g/t Au to values below the detection limit of the fire assay in sulphide-poor

portions always indicate transitions from sulphide-rich to poor BIF. Gold, ranging in size from 10 to 80 μm, is intergrown with pyrite, pyrrhotite and arsenopyrite. It occurs in fractures or along grain boundaries of pyrite and arsenopyrite. Pyrite is the most common sulphide and accounts for > 90% by volume of all sulphides. Most of the pyrite form porous grains that may be zoned, displaying As-rich centres.

The Fonte Grande Sul ore body is located in the SE closure of the Cuiabá fold (Fig. 2a). It is the largest and highest grade ore body in the deposit. Resources are calculated at 4.91 million tonnes grading 13.87 g/t Au, with additional reserves of 0.8 million tonnes grading 8.11 g/t Au (AngloGold Ashanti 2018). The thickness of the ore body varies between 4 and 6 m. The mineralised BIF is intensely sulphidised (ESM-1), folded and disrupted, containing generally disseminated and massive ores that lack banding.

The recently discovered VQZ ore body (Fig. 2a) has significant gold grades associated with andesite-hosted quartz-rich shear veins and is located between levels 9 and 17 in the southeastern part of the Cuiabá fold hinge (Fig. 2b). Mineralisation is predominantly controlled by a strike slip, oblique shear zone, with native gold hosted in quartz-rich shear veins, and disseminated sulphide minerals in hydrothermally altered country rocks. The Au grade reaches up to ~ 500 g/t due to the presence of free coarse gold (Vitorino 2017).

Hydrothermal alteration studies at Cuiabá were carried out by Vieira (1988, 1991), Ribeiro-Rodrigues (1998), and Lobato et al. (1998, 2001a, b). These authors showed that the carbonaceous pelites are only locally altered by sulphide-quartz-carbonate veinlets and that the Cuiabá-BIF is strongly sulphidised. Mafic volcanic rocks are overprinted by pervasive alteration, where distal alteration comprises an assemblage of chlorite, carbonate ± sericite, and sulphide minerals, intermediate alteration is characterised by an assemblage of carbonates, chlorite, quartz, plagioclase and sulphide minerals, and the proximal alteration is composed of a quartz, sericite, sulphide mineral and gold.

Materials and methods

Quartz vein samples for fluid inclusion analyses were taken from drill cores CBABSD007 and CBABSD009 intersecting the VQZ ore body at Level 17 (Fig. 2c) and underground exposures of shear and extensional veins of the andesite-hosted VQZ ore body at Level 15 of the Cuiabá mine (Figs. 2b and 3g–i).

The fluid inclusion study was carried out on vein quartz of the S_m (mylonitic foliation)–related mineralised quartz-sulphide and barren quartz veins. Nine doubly polished thick sections were prepared and petrographically mapped in transmitted light. Four of them were chosen for microthermometry. Measurements were conducted using a Linkam THMSG 600 heating and freezing stage with a T95 temperature programmer at the Laboratory of Metallogeny, Institute of Geoscience, at the Federal University of Minas Gerais, Brazil. The stage was calibrated with synthetic inclusions. All measurements were collected by predetermined temperature profiles that include a sequence of step-by-step continuous heating or cooling rates. Heating sequences have been performed slowly to prevent decrepitation. Calculated salinity (wt% NaCl equiv) and bulk composition of all FIAs, as well as pressure and temperature values to construct isochores, were obtained using the MacFlinCor program (Brown and Hagemann 1995). Eutectic temperatures of aqueous FIAs range between − 45 and − 35 °C, indicating a mix of different salts (Borisenko 1977; Goldstein and Reynolds 1994). For measured FIAs that show final ice-melting temperatures above the eutectic for H_2O–NaCl ($< − 21.2$ °C), the equation of state by Bodnar and Vityk (1994) was used for the H_2O-NaCl-(KCl) system. In the case of clathrate-melting temperatures, (Tm_{Clath}) the equation of Jacobs and Kerrick (1981) for the H_2O-CO_2-CH_4-NaCl was applied due to the presence of CO_2 and/or CH_4. Measurement of homogenisation temperatures of the CO_2 phase (Th_{CO2}) is limited to inclusions larger than 10 μm. The $Th_{TOT(L-V)}$ values were obtained from Qz2 of V2 extensional and V3 extensional vein arrays, as well as Qz5 from V4 late-stage veins. Measurements on various aqueous-carbonic FIAs with probably higher proportions of volatile phases (CH_4, H_2S, N_2) did not allow salinity calculations with Tm_{Clath} above 10 to 16 °C.

Raman spectroscopy investigations were carried out at the Institute of Engineering at the Federal University of Minas Gerais, Brazil. Raman spectra were obtained using a JobinYvon/Horiba LABRAM-HR 800 spectrograph equipped with a He-Ne laser (632.8 nm) and linked to a N_2 liquid-cooled CCD (charge coupled device) detector. The excitation and collection of the scattered light were achieved using an Olympus BHX microscope focused on single-fluid inclusions at high magnification (× 50 or × 100 objectives). Acquisition times varied between 10 and 30 s depending on the background fluorescence of the fluid inclusions. Laser-Raman analyses were applied to several types of aqueous and aqueous-carbonic FIAs in different quartz types. Complex gas mixtures of CO_2, CH_4, and N_2 and a limited set of solutes have been detected within each non-aqueous phase at ambient P-T conditions. Data processing of all Raman spectra was conducted using the software LabSpec 5. Semiquantitative determination of gas species (CO_2, CH_4, and N_2) and their relative abundances (in mol%) used the method of Burke (2001). Wavelength-dependent relative Raman scattering cross-sections (σ 532 nm) for each gas species were determined by interpolation from Burke (2001). The instrumental efficiency for all components was set to 0.92 in all calculations based on Garofalo et al. (2014). Uncertainties in calculated mole fractions of species present in the carbonic phase of the inclusions are within 20% relative.
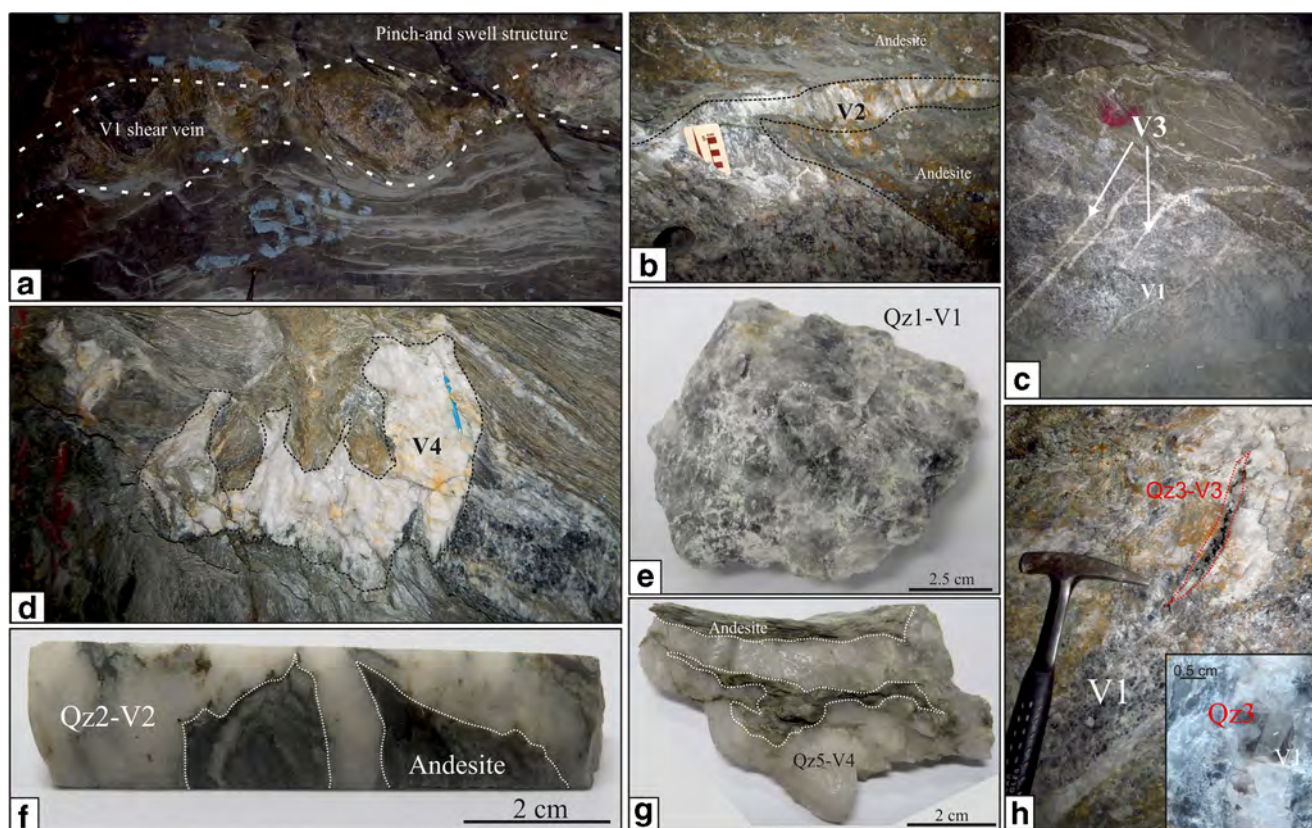
Fig. 3 Photographs of quartz veins, hand specimen, and drill core sections of the andesite-hosted quartz veins forming part of the Veio de Quartzoore body (after Vitorino 2017). **a** V1 shear vein, indicating pinch-and swell structure (Level 15, VQZ ore body). **b** V2 extensional vein (Level 15, VQZ ore body). **c** V3 extensional vein arrays within V1 shear vein (Level 15, VQZ ore body). **d** V4 extensional late-stage veins (Level 15, VQZ ore body). **e** Hand specimen of V1 shear veins consisting of Qz1 (Level 15). **f** Drill core sections of V2 extensional veins (Qz2) (drill core CBABSD07, Level 17). **g** Hand specimen of V4 extensional veins (Qz5) (Level 15). **h** Stope view and sample location of V3 extensional array veins consisting of Qz3 (Level 15, VQZ ore body)

Ion chromatography was performed on quartz samples of the andesite-hosted quartz shear and extensional veins at the School of Earth and Environment, University of Leeds. Quartz samples were reduced to a grain size of 0.5–1 mm and contaminant minerals removed by picking under a binocular microscope. Quartz types of V1 and V2 veins were separated. However, mixing of several fluid inclusion populations contained in the quartz cannot be ruled out. Samples and duplicates were cleaned three times with 18.2 MΩ Milli-Q water. Dry samples were crushed to a fine powder in an agate pestle and mortar and 7 mL of water was added to redissolve the contents of the fluid inclusions. The solution was filtered through a 0.2-μm nylon filter to remove any particles. Cl^-, Br^-, and SO_4^{2-} were determined by using ion chromatography. The leachates were analysed for cations such as Na^+, K^+, and Li^+ by atomic emission spectroscopy. As the amount of fluid inclusions leached is unknown, molar ratios are used.

Laser ablation ICP-MS analyses on FIAs trapped in quartz of shear and extensional veins were conducted at the School of Earth and Environment, University of Leeds. The calibration was performed using the standard NIST 610. Fluid inclusion and standard measurements were conducted by using the GeoLas Q Plus excimer laser (ArF, 193 nm, Microlas, Göttingen, Germany). The optical system permits visual observation of the ablation process through a built-in LED source and CCD camera. The material liberated during the ablation is carried by He, purging the ablation cell, into the Agilent 7500 quadrupole mass spectrometer. An octopole reaction cell was used for analyses of ^{40}Ca and ^{56}Fe. A detailed description of the LA-ICP-MS procedure is given in Allan et al. (2005). Elements including Na, K, Ca, Mg, Mn, Fe, Cu, Zn, Sr, Ag, Ba, Pb, As and Au were analysed. Arsenic and Au were measured separately for each vein type to avoid signal interference. Data reduction was conducted with the MATLAB-based SILLS program (Guillong et al. 2008). LA-ICP-MS intensity ratios for fluid inclusions were normalised to Na and converted to concentration ratios by external calibration against NIST 610 standard reference material. For the determination of Na concentration, the average salinity of each FIA was used. The analytical error of LA-ICP-MS measurements and data processed required the use of average salinity values for each analysed FIA. Detection limits vary according to inclusion volume, but for most elements were between 1 and 10 ppm.

The Cuiabá quartz veins

In Cuiabá, the quartz veins hosted in andesite can be classified as (i) fault-fill, (ii) extensional (oblique-extensional) and (iii) breccia veins according to the criteria of Passchier (2001) and Robert and Poulsen (2001) (Table 1; adapted from Vitorino 2017). Vein types are also subdivided based on their cross-cutting relationships, relative chronology, and mineralogical composition into V1 to V4 vein systems (Table 1). According to Vitorino (2017), all vein types are related to Archaean D1 brittle-ductile shear zones and located in the mineralised zones VQZ, SER FW and FGS FW. Shear veins are most common in the studied VQZ ore body.

The VQZ ore body (Fig. 2a, b) is made-up of four vein types (Table 1) with the following vein classification based on the structural model proposed by Vitorino (2017). Both shear and extensional veins show a similar paragenesis, but differ in terms of relative proportions of quartz types, carbonate, sulphide and accessory minerals (Table 1).

Vein type classification

Shear veins (V1), the most abundant in the VQZ ore body, were emplaced during D1 shearing and are parallel to slightly oblique to the main mylonitic S_m foliation (Fig. 3a). They extend ~ 30, 50-m-long strike and are up to 30 m in thickness. Their long axis coincides with the mineral lineation Lmin1. They mainly consist of anhedral, smoky quartz (Qz1; Fig. 3g), minor granoblastic, milky quartz (Qz2), ankerite, sericite, chlorite and albite and contain fragments of host rocks. Accessory minerals are pyrite, pyrrhotite, chalcopyrite, sphalerite and native gold. Wall rock fragments show ductile deformation, are typically sericite-altered and sulphide-rich and may contain significant gold.

The extensional V2 veins are hosted in andesite and controlled by the compositional banding S_b, occurring either at a high angle or subparallel with respect to the mylonitic S_m foliation (Fig. 3b). They represent the most abundant vein type in the centre of the Cuiabá fold and may occur tens to hundreds of meters from the D1 shear zone. Commonly continuous along strike, they can extend for 200 m and range between a few centimetres up to 2 m in thickness. There are mutual cross-cutting relationships between V1 and V2 types. The V2 veins are mainly composed of Qz2, ankerite, sericite, chlorite and minor pyrite, pyrrhotite and chalcopyrite (Fig. 3h).

The V3 extensional vein arrays are at a high angle with the mylonitic S_m foliation, having an average thickness from 5 to 30 cm. The V3 extensional vein arrays are mainly composed of euhedral quartz (Qz3) (Fig. 3f inset) and are immersed within the V1 shear veins (Fig. 3c, f; Table 1).

The V4 extensional veins (hereafter designated as V4 late-stage veins) show massive and tabular vein geometries (Fig. 3d, e). Wall rock fragments are located in the inner part of the veins and impose a brecciated structure. These are controlled by flanking structures (flanking folds and flanking shear bands, cf. Passchier 2001) and barren. They mainly consist of Qz5, carbonate (ankerite, calcite) and locally pyrrhotite and pyrite (Fig. 3d, i, Table 1); these sulphides are present as centimetre- up to 10 cm-sized agglomerates and locally as well-formed grains.

Quartz type classification

Four main quartz types (Qz1, Qz2, Qz3, and Qz5) are discriminated mainly based on morphological characteristics. The Qz1 is typically smoky, anhedral, medium- to coarse-grained, with strong wavy extinction; it is rich in fluid inclusions. The grain boundaries of Qz1 are interlobate (Fig. 4c, d). The polygonal granoblastic, fine- to medium-grained Qz2 developed at the expense of Qz1 (Fig. 4a–d), mainly along crystal boundaries. The proportion of fluid inclusions is relatively low compared with Qz1. Vitreous Qz3 is polygonal and shows well

Table 1 Classification of the Cuiabá quartz veins (adapted after Vitorino 2017)

Vein type Classification after Passchier (2001), Robert and Poulsen (2001)	Vein system	Controlled by	Mineralogical composition		Vein geometry
			Main	Accessory	
Fault-fill	V1 (shear)	S_m	Qz1, Qz2, cb, ser, chl, plg	py, po, cpy, sph, free gold	Folded, pinch and swell, boudins
a. Extensional b. Oblique extensional c. Fault-fill	V2 (a, b, c) (extensional)	S_b	Qz2, Qz1, cb, ser, chl	py, po, cpy, (free gold)	Tabular and folded; boudins and sigma shapes
Extensional vein array	V3 (extensional)	S_m	Qz3, Qz4	–	En-echelon
Extensional and brecciated	V4 (late-stage, extensional)	Flanking and cross-cutting S_m	Qz5, cb	py and po	Tabular and massive

qz quartz, *cb* carbonate, *ser* sericite, *chl* chlorite, *plg* plagioclase, *py* pyrite, *po* pyrrhotite, *cpy* chalcopyrite, *sph* sphalerite

Fig. 4 Photomicrographs of quartz types. **a** Qz1 and Qz2 of V1 shear veins (transmitted light) (sample 009_7). **b** Qz1 and Qz2 of V1 shear veins (transmitted light, crossed nicols) (sample 009_7). **c** Intergrowth of all quartz types of V1 shear and V3 extensional vein arrays (transmitted light) (sample FICU01). **d** Qz5 of V4 late-stage veins (transmitted light) (sample QZL_1)
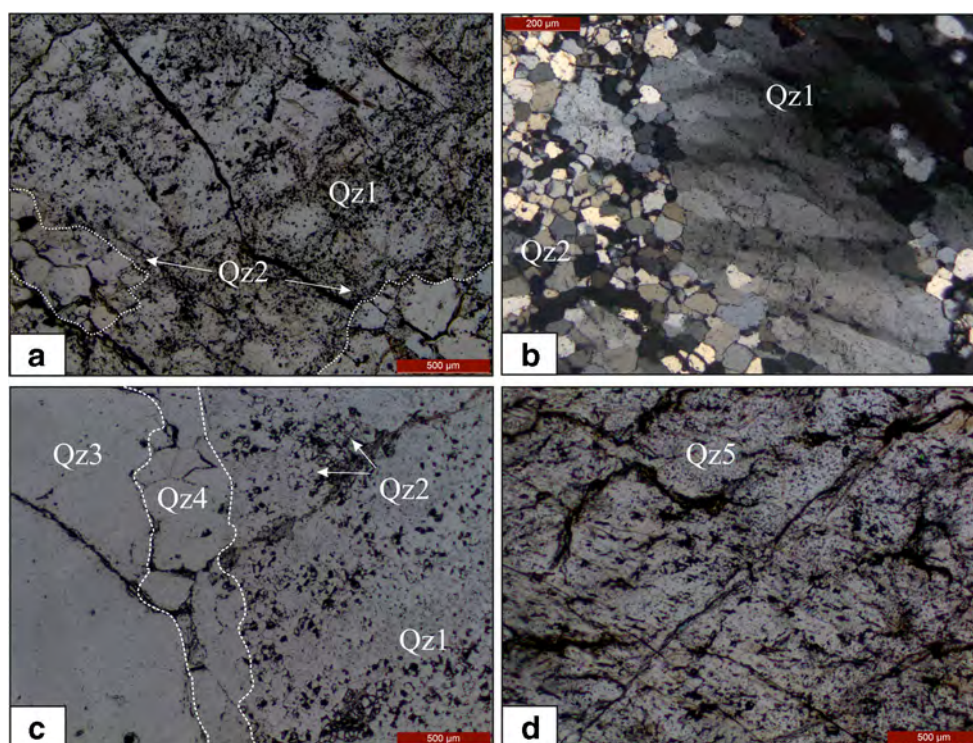
defined limits of coarse- to very coarse-grained transparent euhedral crystals that are locally transformed to granoblastic Qz4 (Fig. 4e). The Qz3 and Qz4 contain a moderate amount of fluid inclusions. Qz5 shows similar morphological features to Qz1.

Fluid inclusion data of the VQZ ore body

Fluid inclusion classification and description

The results of detailed petrography constraining the size, shape, and L/V phase ratio of fluid inclusions, their occurrence as groups, and trails or individual inclusions are provided in Table 2. Emphasis was placed on the identification of FIAs, which are defined as the most finely discriminated fluid inclusion trapping event that can be identified based on petrography (Goldstein and Reynolds 1994). In total, 20 distinct FIAs are observed and numbered (1–20, subscript is indicated by subscript characters). The FIAs in internal trails and three-dimensional groups, with respect to individual quartz grains, are pseudosecondary in nature, whereas trail cross-cutting quartz grain boundaries are determined as secondary in origin (Sterner and Bodnar 1984; Wilkinson 2001). Secondary FIAs and FIAs that appear randomly and cannot be constrained with respect to their relative timing of trapping, defined as indeterminate, are not further considered in this investigation.

This study focuses on primary and pseudosecondary FIAs, which are present in all vein and quartz types except Qz4 (Fig. 5, Table 2). Primary and pseudosecondary FIAs are defined by (i) aqueous-carbonic fluid inclusions, irregular to ovoid-shaped, 5–10 μm, locally up to 15 μm in size, and contain about 10 vol.% vapour; and (ii) aqueous fluid inclusions, regular to ovoid-shaped, about 5–10 μm in size and contain about 5–10 vol.% vapour.

Microthermometry results

V1 shear veins

Aqueous fluid inclusions in Qz1 show eutectic temperatures (T_e) between − 43 and − 39 °C; Tm_{ice} between (i) − 9.5 and − 5.1 °C, and (ii) − 3.5 and − 1.1 °C. The $T_{DECREP(L)}$ ranges between 220 and 250 °C (Fig. 6c, Table 3). Salinity values range from (i) 1.8 to 5.6 wt% NaCl equiv and (ii) 8.1 up to 13.4 wt% NaCl equiv (Fig. 6a).

Aqueous-carbonic fluid inclusions display Tm_{CO2} between − 61.7 and − 58.1 °C; Tm_{Clath} between (i) 1.2 and 3.6 °C and (ii) 6.1 and 6.6 °C; Th_{CO2} between 25.1 and 30.4 °C; and $T_{DECREP(V)}$ between 280 and 310 °C (Fig. 6c, Table 4). Aqueous-carbonic fluid inclusions indicate salinities ranging from 7.2 to 12.7 wt% NaCl equiv (Fig. 6c). The bulk density varies between 1.02 and 1.05 g/cm^3.

Table 2 Summary of FIAs and their characteristics (e.g., chemical system, L/V ratio, shape, size and occurrence) based on quartz and vein types[1]

Vein type	Sample ID	Qz type	FIA	N	Chemical system	L/V ratio	Shape	Size (in μm)	Occurrence
V1 shear veins	009_7	Qz1	7	5	Aq	10	Ovoid-shaped and negative crystal	5–10	Grouped
		Qz1	8_A	5	Aq	10	Irregular to ovoid-shaped	5–10	Grouped
		Qz1	8_B	3	Aq	10	Irregular to ovoid-shaped	5–10	Grouped
		Qz1	8_C	4	Aq-carb	10	Irregular to ovoid-shaped	5–10	Grouped
		Qz1	8_D	2	Aq	10	Irregular to ovoid-shaped	5–10	Grouped
		Qz1	8_E	2	Aq-carb	10	Irregular to ovoid-shaped	5–10	Grouped
V2 extensional veins	007_2	Qz1	10	3	Aq-carb	10	Negative crystal	5–10	Isolated
		Qz2	9	5	Aq	10	Regular to ovoid-shaped	5–10	Isolated
		Qz2	11_A	7	Aq	10	Regular to ovoid-shaped		Grouped
		Qz2	11_B	3	Aq	10	Regular to ovoid-shaped	5–10	Grouped
		Qz2	11_C	5	Aq	10	Regular to ovoid-shaped	5–10	Grouped
		Qz2	11_D	8	Aq	10	Regular to ovoid-shaped	5–10	Grouped
		Qz2	11_E	5	Aq	10	Regular to ovoid-shaped	5–10	Grouped
V3 extensional vein arrays	FICU01	Qz1	1_A	4	Aq	10	Irregular to ovoid-shaped	5–10	Grouped
		Qz1	1_B	7	Aq	10	Irregular to ovoid-shaped	5–10	Grouped
		Qz2	2_A	5	Aq	10*	Irregular to ovoid-shaped	5–10	Grouped
		Qz2	2_B	4	Aq	10	Regular to ovoid-shaped	5–10	Grouped
		Qz2	2_C	4	Aq	10	Regular to ovoid-shaped	5–10	Grouped
		Qz2	2_D	3	Aq	10	Regular to ovoid-shaped	5–10	Grouped
		Qz2	2_E	6	Aq	10	Regular to ovoid-shaped	5–10	Grouped
		Qz2	2_F	4	Aq	10	Regular to ovoid-shaped	5–10	Grouped
		Qz2	2_G	7	Aq	10	Regular to ovoid-shaped	5–10	Grouped
		Qz2	3	6	Aq	10	Regular	5–10	Isolated
		Qz3	4_A	3	Aq	10	Regular	5–15	Grouped
		Qz3	4_B	1	Aq-carb	10	Regular to ovoid-shaped	5–15	Isolated
		Qz3	4_C	2	Aq-carb	10	Regular	5–15	Isolated
		Qz3	4_D	3	Aq-carb	10	Ovoid-shaped to irregular	10–20	Isolated
		Qz3	5_A	5	Aq	10	Irregular	5–15	Grouped
		Qz3	5_B	4	Aq	10	Irregular	5–10	Isolated
		Qz3	6	5	Aq	10	Regular to ovoid-shaped	5–15	Internal trail
V4 late-stage veins	QZL_1	Qz5	12_A	6	Aq	10	Regular to ovoid-shaped	10–20	Grouped
		Qz5	12_B	2	Aq-carb	10	Regular to ovoid-shaped	10–15	Isolated
		Qz5	13	4	Aq	10	Irregular	10–15	Isolated
		Qz5	14	7	Aq	10	Regular ovoid-shaped	10–15	Grouped
		Qz5	15	5	Aq	10	Regular	5–15	Grouped
		Qz5	16_A	6	Aq	10	Ovoid-shaped to irregular	10–15	Isolated
		Qz5	16_B	5	Aq	10	Ovoid-shaped to irregular	5–15	Grouped
		Qz5	16_C	2	Aq-carb	10	Ovoid-shaped to irregular	5–15	Isolated
		Qz5	16_D	3	Aq	10	Ovoid-shaped to irregular	10–15	Grouped
		Qz5	17_A	2	Aq	10	Ovoid-shaped	5–10	Grouped
		Qz5	17_B	2	Aq-carb	10	Ovoid-shaped	10–15	Isolated
		Qz5	18	8	Aq	10	Ovoid-shaped to irregular	5–15	Grouped
		Qz5	19	2	Aq	10	Ovoid-shaped to irregular	5–10	Isolated
		Qz5	20	8	Aq	10	Ovoid-shaped to irregular	5–15	Grouped

Qz Quartz, *N* Number

[1] Sample FICU01 mainly consists of Qz3, but also describes Qz1 and Qz2, both corresponding to the V1 shear vein type
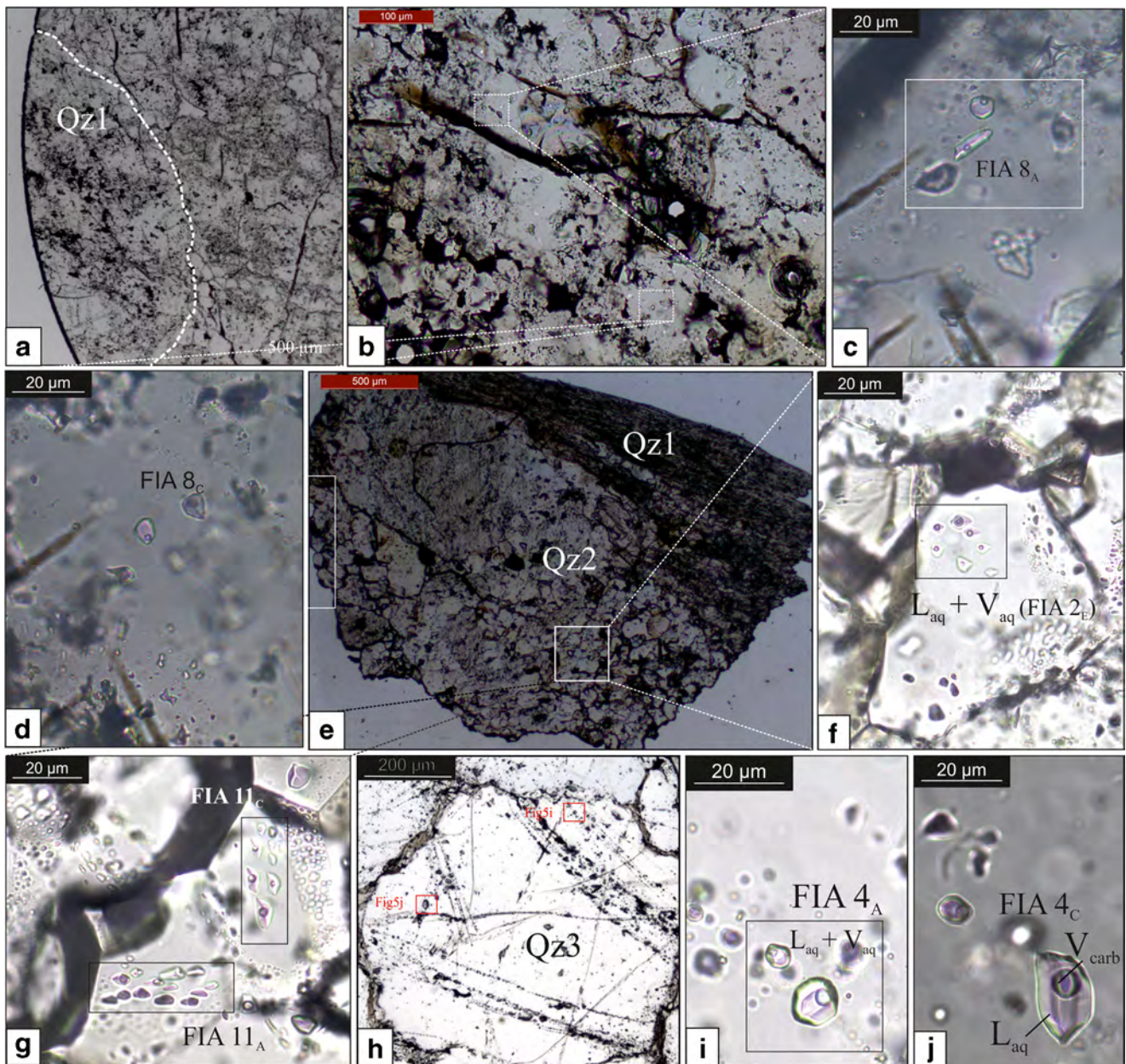
Fig. 5 Examples of representative FIAs of all vein types, Veio de Quartzo ore body. **a-d** Qz1-V1 shear veins with small-sized, two-phase aqueous (FIA8$_A$), and aqueous-carbonic (FIA8$_C$)–grouped FIAs. **e-g** Qz2-V2 and Qz2-V3 extensional veins showing, two-phase, aqueous, FIAs (FIA 2$_E$, FIA 11$_A$, FIA 11$_C$). **h-j** Qz3-V3 extensional vein arrays displaying two-phase, grouped aqueous fluid inclusion (FIA4$_A$) and two-phase, individual, aqueous-carbonic fluid inclusions (FIA 4$_C$) an internal trail of two-phase, aqueous fluid inclusions (FIA 6). Photomicrographs taken under transmitted light

V2 extensional veins

Aqueous fluid inclusions in Qz2 display T_e between (i) − 44 and − 42 °C and (ii) − 45 to − 35 °C; Tm$_{ice}$ between − 5.2 and − 3.3 °C, Th$_{TOT(L)}$ from 260 to 290 °C (FIA 11$_D$), and $T_{DECREP(L)}$ at 325 °C (Fig. 6b). Salinity values range from 5.0 to 8.5 wt% NaCl equiv (Fig. 6a Table 3). Aqueous-carbonic fluid inclusions in Qz1 show Tm$_{Clath}$ between 15.1 and 16.8 °C and $T_{DECREP(L)}$ from 215 to 275 °C (Table 4).

V3 extensional vein arrays

Aqueous fluid inclusions in (i) Qz1 and (ii) Qz2 show T_e between (i) − 43 and − 39 °C and (ii) − 39 and − 35 °C respectively; Tm$_{ice}$ between (i) − 8.9 and − 7.0 °C and (ii) − 5.5 and − 3.0 °C; and $T_{DECREP(L)}$ between (i) 190 and 230 °C. Average salinities of aqueous fluid inclusions in Qz1 range from 10.5 to 12.7 wt% NaCl equiv. Homogenisation into vapour of FIAs in Qz2 is observed at 220 °C and 230 °C (Fig. 6b). Average salinities of aqueous fluid inclusions in Qz2 range from 4.9 to
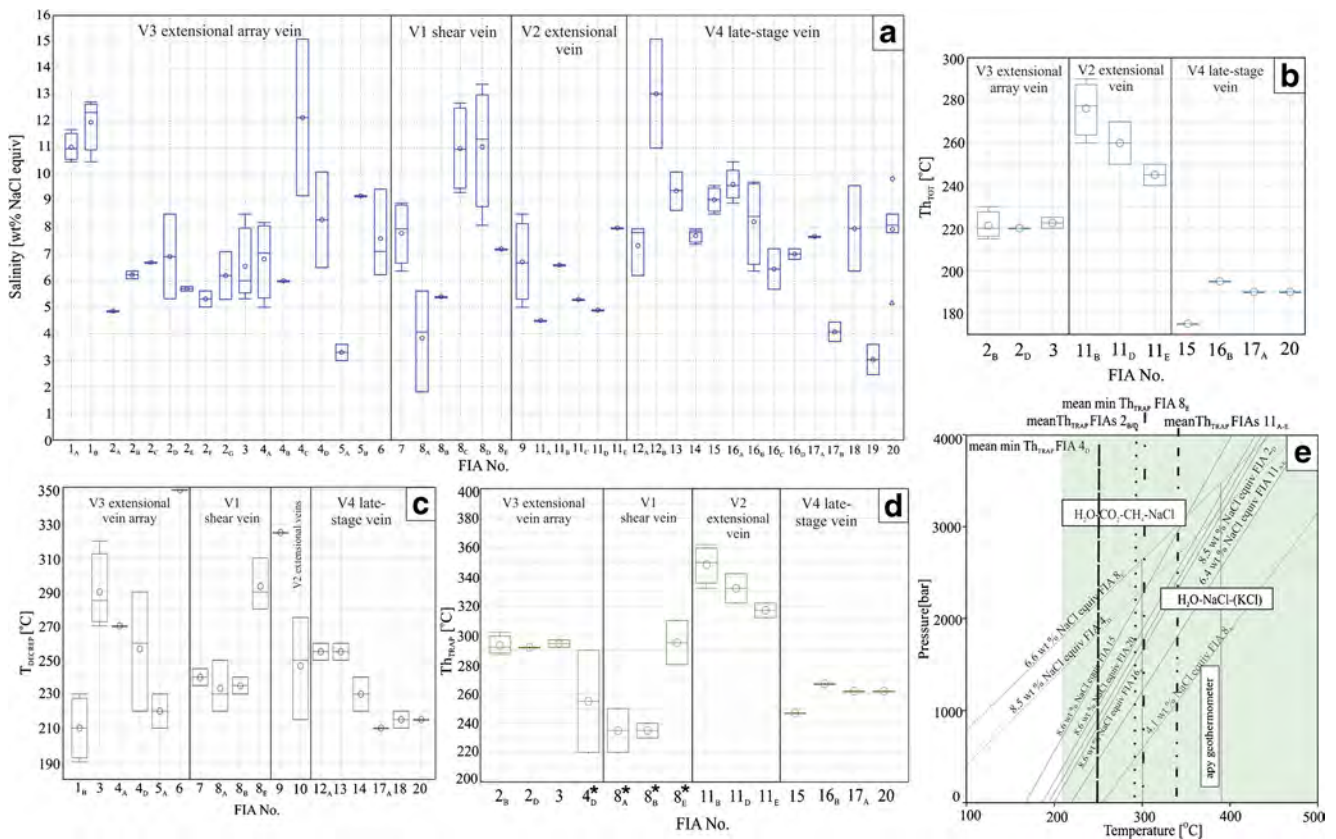
Fig. 6 Box and whisker plots of **a** salinity, **b** Th_{TOT}, **c** T_{DECREP}, and **d** Th_{TRAP} for analysed FIAs. The central box is the middle 50% of the data from 25% quartile (Q1) to 75% quartile (Q3); whiskers are extreme values that are not outliers. Circles indicate outlier values. **d** Isochore diagram of aqueous and aqueous-carbonic FIAs. The range of P_{min} and

P_{max} is calculated based on the intersection points with the mean Th_{TRAP} and calculated arsenopyrite formation temperature (Kresse 2018). The bluish area indicates metamorphic greenschist facies conditions (Spear 1995)

8.5 wt% NaCl equiv (Fig. 6a). Aqueous fluid inclusions in Qz3 show T_e between − 35 and − 30 °C, Tm_{ice} between − 6.3 and − 1.8 °C; $T_{DECREP(L)}$ between 210 and 270 °C, with outliers up to 350 °C(Table 3). Salinity values for range between 3.0 and 9.5 wt% NaCl equiv (Fig. 6a, Table 3).

Aqueous-carbonic fluid inclusions in Qz3 show Tm_{CO2} from − 61.0 to − 57.2 °C; values of Tm_{Clath} between 0.4 and 6.8 °C; and $T_{DECREP(V)}$ between 220° and 290 °C (Fig. 6c, Table 4). Salinity values of fluid inclusions vary from 6.0 to 10.1, with outliers up to 15.1 wt% NaCl equiv (Fig. 6a, Table 4). The bulk density of FIAs varies between 1.02 and 1.09 g/cm³.

V4 late-stage veins

Aqueous fluid inclusions display T_e between − 44 and − 38 °C, with Tm_{ice} ranging between − 7.0 and − 3.9 °C. Homogenisation temperatures (into L) vary from 175 to 195 °C (Fig. 6b). Decrepitation temperatures (into L) are observed between (i) 210 and 220 °C and (ii) 220 and 260 °C (Table 3). Salinity values range between (i) 6.2 and 8.0 wt% and (ii) 8.9 and 10.5 wt% NaCl equiv (Fig. 6a, Table 3).

Aqueous-carbonic fluid inclusions in Qz5 shows Tm_{CO2} between − 61.5 and − 59.9 °C; and Tm_{Clath} between (i) 0.3 and 3.6 and (ii) 6.1 and 8.1 °C (Table 4). The Th_{CO2} was not observed due to the small size of the fluid inclusions. The salinity ranges from 3.7 to 15.1 wt% NaCl equiv in fluid inclusions in Qz5 (Fig. 6a, Table 4). The bulk density of aqueous-carbonic fluid inclusions ranges from 1.01 up to1.08 g/cm³ (FIA 12$_B$).

Raman spectroscopy

The majority of non-aqueous phases of FIAs in all quartz and vein types are characterised by Raman bands of gaseous components such as CO_2, CH_4, and N_2. Methane shows a constant and single symmetric stretching band at approximately 2909 cm⁻¹ (± 5 cm⁻¹) (ESM-3). The presence of CO_2, located at 1281 cm⁻¹ (± 3 cm⁻¹) and 1384 cm⁻¹ (± 3 cm⁻¹), was detected in aqueous-carbonic fluid inclusions trapped in Qz1-V1 shear veins (ESM-3). Nitrogen (at 2324 ± 2 cm⁻¹) and dissolved $HS^−$ (at 2574 cm⁻¹) have been recorded only in low intensity in

Table 3 Summary of microthermometry results and calculated salinity values of aqueous FIAs trapped in quartz of andesite-hosted veins[1]

Sample ID	Vein type	Quartz type	FI phase	FIA	N	Min-max Tm_{ice}	Min-max Th_{TOT} (°C)	Min-max T_{DECREP} (°C)	Min-max salinity (wt% NaCl equiv.) (average salinity value)
009_7 3e	V1 shear veins	Qz1	Laq + Vaq	8_A	5	− 3.5 to − 1.1	–	220 to 250 (into L)	1.8 to 5.6 (3.8)
009_7 3b		Qz1	Laq + Vaq	8_B	3	− 3.4	–	230 to 240	5.4
009_7 3b		Qz1	Laq + Vaq	8_D	4	− 9.5 to − 5.2	–	–	8.1 to 13.4 (12.4)
009_73a		Qz1	Laq + Vaq	7	5	− 5.8 to − 4.2	–	235 to 245	6.4 to 8.9
007_2 1a	V2 extensional veins	Qz2	Laq + Vaq	9	5	− 5.2 to − 3.3	–	325	5.0 to 8.5 (6.7)
007_2 1		Qz2	Laq + Vaq	11_A	7	− 4.1 to − 3.5	260 to 290 (into L)	–	4.5 to 6.6 (5.8)
		Qz2	Laq + Vaq	11_B	3			–	
		Qz2	Laq + Vaq	11_C	4			–	
007_2 3		Qz2	Laq + Vaq	11_D	8	− 5.0 to − 3.0	250 to 270 (into L)	–	4.9
		Qz2	Laq + Vaq	11_E	5		230 to 250 (into L)	–	8.0
FICU4a	V3 extensional vein arrays	Qz3	Laq + Vaq	4_A	3	− 4.9 to − 2.9	–	270	4.8 to 7.8 (6.6)
FICU3a		Qz3	Laq + Vaq	6	5	− 6.2 to − 3.9	–	350	6.2 to 9.5 (8.3)
FICU3b		Qz3	Laq + Vaq	5_A	5	− 2.2 to − 1.8	–	210/220/230	3.0 to 3.6
FICU3c		Qz3	Laq + Vaq	5_B	4	− 6.3	–	–	9.2
FICU4d/e		Qz2	Laq + Vaq	3	6	− 5.5 to − 3.3	220 to 225 (into L)	270 to 320	5.5 to 8.5 (5.8)
FICU2a		Qz2	Laq + Vaq	2_A	5	− 3.0	–	–	4.9
FICU2b		Qz2	Laq + Vaq	2_B	4	− 4.0 to − 3.8	220 to 230 (into L)	–	6.1 to 6.4 (6.2)
FICU2c		Qz2	Laq + Vaq	2_C	4	− 4.2	–	–	6.7
FICU1a		Qz2	Laq + Vaq	2_D	3	− 5.5 to − 3.3	220 (into V)	–	5.8 to 8.5 (7.2)
FICU1b		Qz2	Laq + Vaq	2_E	6	− 3.6 to − 3.5	–	–	5.6 to 5.8
FICU1c		Qz2	Laq + Vaq	2_F	4	− 3.5 to − 3.1	–	–	5.0 to 5.6 (5.3)
FICU1d		Qz2	Laq + Vaq	2_G	7	− 4.6 to − 3.2	–	–	5.3 to 7.1 (6.5)
FICU1		Qz1	Laq + Vaq	1_A	4	− 8.0 to − 7.0	–	190 to 230	10.5 to 11.7 (11.0)
FICU1f			Laq + Vaq	1_B	7	− 8.9 to − 7.0	–		10.5 to 12.7
QZL 1a	V4 late-stage veins	Qz5	Laq + Vaq	12_A	6	− 5.1 to − 3.9	–	250 to 260	6.2 to 8.0
QZL 1a		Qz5	Laq + Vaq	13	4	− 6.7 to − 5.6	–		8.7 to 10.1 (9.4)
QZL 1b		Qz5	Laq + Vaq	14	7	− 5.1 to − 2.4	–	220 to 240	3.9 to 8.0 (7.0)
QZL 1c		Qz5	Laq + Vaq	15	5	− 6.3 to − 5.5	175 (into L)	–	8.5 to 9.6 (9.1)
QZL 2a		Qz5	Laq + Vaq	16_A	6	− 7.0 to − 5.8	–	–	8.9 to 10.5 (9.6)
QZL 2a		Qz5	Laq + Vaq	16_B	5	− 6.4 to − 4.0	195 (into L)	–	6.4 to 9.7 (8.2)
QZL 2a		Qz5	Laq + Vaq	16_D	3	− 4.4 to − 4.3	–	–	6.8 to 7.2
QZL 2b		Qz5	Laq + Vaq	17_A	2	− 4.9	190 (into L)	210	7.7
QZL 3		Qz5	Laq + Vaq	18	8	− 6.3 to − 4	–	210 to 220	6.4 to 9.6 (7.9)
QZL 3 g		Qz5	Laq + Vaq	20	8	− 5.5 to − 3.2	190 (into L)	215	5.2 to 8.5 (7.6)
QZL 3f		Qz5	Laq + Vaq	19	2	− 2.2 to − 1.5	–	–	2.5 to 3.6 (3.0)

Numbering of FIA's starts with FIA 8 in V1 shear veins due to preparation progress

[1] Sample FICU1 mainly consists of Qz3, but is in conjunction with Qz1 and Qz2 of V1 shear vein

aqueous-carbonic fluid inclusions in Qz3-V3 extensional vein arrays (ESM-3). Aqueous fluid inclusions in Qz2-V2 and Qz2-V3 extensional vein arrays show significant lower amounts of CH_4 and no CO_2. The Raman spectrum of molecular CO_2 shows two strong bands at 1281 cm^{-1} ($\pm$ 3 cm^{-1}) and 1384 cm^{-1} ($\pm$ 3 cm^{-1}) (ESM-3).

The calculations of the non-aqueous phase of individual fluid inclusions of FIA 8_{C+E}, in Qz1-V1 shear veins, resulted in 91.4 mol% CO_2 and 8.6 mol% CH_4, whereas the non-aqueous phase of individual fluid inclusions of FIA4_C in Qz3-V3 extensional vein arrays is composed of 30.0 mol% CO_2, 41.0 mol% CH_4 and 28.0 mol% N_2. The FIAs 11_{A-E} in Qz2-V2 extensional veins display CH_4

Table 4 Summary of microthermometry results and calculated clathrate salinity values of aqueous-carbonic FIAs trapped in quartz of andesite-hosted veins

Sample ID	Vein type	Quartz type	FI type	FIA	N	Min-max Tm_{CO_2}	Min-max T_C (°C)	Min-max Th_{CO_2}	Min-max T_{DECREP} (°C)	Min-max salinity (wt% NaCl equiv)
009_7 2	V1 shear veins	Qz1	Laq + Vcarb	8_C	4	− 61.7 to − 58.1	1.2 to 3.6	25.1 to 30.4	–	9.3 to 12.7
009_7 2		Qz1	Laq + Vcarb	8_E	3	− 61.1 to − 59.1	6.1 to 6.6	29.4 to 30.1	280 to 310 (into V)	7.2
007_2 2	V2 extensional veins	Qz1	Laq + Vcarb	10	3	–	15.2 to 16.8	–	215 to 275	–
FICU4b	V3 extensional vein arrays	Qz3	Laq + Vcarb	4_B	1	− 57.4	6.8	–	–	6.0
FICU4c		Qz3	Laq + Vcarb	4_C	2	− 57.4	0.4 to 3.6		–	9.2 to 15.1
FICU4c		Qz3	Laq + Vcarb	4_D	3	− 61.0 to − 57.2	3.0 to 6.5	28.4 to 30.1	220 to 290 (into V)	6.5 to 10.1 (8.2)
QZL 2b	V4 late-stage veins	Qz5	Laq + Vcarb	16_C	2	–	6.1 to 7.0	–	–	5.7 to 7.2 (6.4)
QZL 2c		Qz5	Laq + Vcarb	17_B	2	–	7.7 to 8.1	–	–	3.7 to 4.4
QZL 1a		Qz5	Laq + Vcarb	12_B	2	–	0.3 to 3.6	–	–	11.0 to 15.1

fluid inclusions only with count rates between 400 and 880.

Trapping conditions

No petrographic evidence for phase immiscibility (cf. Ramboz et al. 1982) has been observed in the samples analysed. Due to the lack of independent pressure estimate and without observing any homogenisation temperature for aqueous-carbonic fluid inclusions, the decrepitation temperatures are interpreted as minimum trapping temperatures (cf., Roedder 1984). In the case of the aqueous fluid inclusions, a temperature (pressure) correction can be applied using an independent pressure estimate, the Potter (1977) equation of state, and interactive graphs in the MacFlinCor program (Brown and Hagemann 1995). The independent pressure estimate of 1.5 kbars is derived from the metamorphic mineral assemblage that characterises the host rocks in

the Cuiabá gold deposit (Vieira 1991; Lobato et al. 2001c). These pressures are interpreted to reflect the approximate pressure conditions at the time of mineralisation, which are compatible with a mesozonal (1–2 kbars at 4–8-km paleodepth level assuming lithostatic pressure conditions) crustal setting for Cuiabá (cf. Hagemann and Brown 1996; Hagemann and Cassidy 2000; Ridley and Diamond 2000).

Homogenisation and decrepitation as well as calculated trapping temperatures of FIAs are shown in Table 5 and Fig. 6b/d. A possible indication for phase immiscibility is provided by one aqueous, FIA 2_D, trapped in Qz2-V3 vein. In this assemblage, vapour-rich fluid inclusions all homogenised into vapour at about 220 °C (Table 3). The majority of the FIAs in Qz1-V1 shear veins and Qz3-V3 extensional vein arrays decrepitated prior to homogenisation into vapour.

Based on the Th_{TRAP} of aqueous and minimum Th_{TRAP} of aqueous-carbonic FIAs, isochores were calculated for aqueous FIAs 11_{A-E} (5.8 wt% NaCl equiv), and aqueous FIA 9

Table 5 Homogenisation, decrepitation, and trapping temperatures based on pressure (temperature) correction of FIAs. Th_{TRAP} from 300 to 360 °C have a similar range as those of the arsenopyrite formation temperature (300–390 °C) obtained from geothermometry in BIF-hosted arsenopyrite (Kresse 2018)

Vein type	FIA	Homogenisation temperature	Trapping temperature (*decrepitation temperature)
Qz1-V1	FIA 8_{A-B}	–	220–250 °C*
	FIA 8_E	–	280–310 °C*
Qz2-V3	FIA 2	220–230 °C	290–300 °C
	FIA 3	220–225 °C	290–295 °C
Qz2-V2	FIA 11_{A-E}	230–290 °C	300–360 °C
Qz3-V3	FIA 4_D	–	220–270 °C*
Qz5-V4	FIA 15	175 °C	245–265 °C
	FIA 16_B	195 °C	
	FIA 17_A	190 °C	
	FIA 20	190 °C	

[*] Decrepitation temperature

(8.5 wt% NaCl equiv), both trapped in Qz2-V2 extensional vein, and from aqueous-carbonic FIA 8$_E$ (7.2 wt% NaCl equiv). Isochores were calculated based on the equation of state of Bodnar and Vityk (1994) for aqueous FIAs and Jacobs and Kerrick (1981) for aqueous-carbonic FIAs. Using the intersection of the "maximum" isochores of aqueous FIAs 11$_{A-E}$ and aqueous-carbonic FIA 8$_E$ with the crystallisation temperature of 300–390 °C for arsenopyrites in the proximal alteration zone (Kresse 2018), an average pressure between 1.1 and 3.2 kbars is estimated (Fig. 6e).

Ion chromatography

The ion chromatography data for all vein types show that fluid inclusions are dominated by Na and K, with lesser amounts of Li (Table 6). Chloride ion (Cl$^-$) and SO$_4^{2-}$ are the major anions in quartz-hosted fluid inclusions. Significant SO$_4$ values may be attributed to the presence of sulphides and their subsequent oxidation and/or leaching. Fluid inclusions of the V4 late-stage veins display maximum chloride values of up to 32,600 ppb. Bromide values are variable, but the highest are in fluid inclusions of the V2 extensional veins (Table 6).

Laser ablation ICP-MS

Analytical results for FIAs trapped in quartz from V1, V2, V3, and V4 veins show that Na$^+$, Ca^{2+}, K$^+$, and Mg^{2+} are the dominant cations and are discussed for each vein type below. Analyses of As and Au (Fig. 7) were conducted separately in aqueous FIAs trapped in Qz1-V1, Qz2-V2, and Qz5-V4 veins, because of possible interferences with other trace

element signals (ESM-4). This data set is discussed separately below. Sodium and K were measured simultaneously. The average LA-ICP-MS concentration data for all FIAs analysed are provided in ESM-5.

V1 shear veins

Quantitative LA-ICP-MS microanalysis of FIAs yielded one distinct population of data with a signature of Na > K > Ca > Mg (Fig. 8). The solutes of aqueous-carbonic fluid inclusions are elevated in Sr and Ba in comparison with aqueous inclusions (ESM-5). Base metal concentrations are in the order of 60–1600 ppm (Fig. 8). The maximum Fe concentrations are in the range of 218 to 788 ppm. Manganese concentrations range from 33 to 61 ppm in aqueous fluid inclusions, whereas aqueous-carbonics show a large range from 34 to 111 ppm (ESM-5).

V2 extensional veins

Aqueous fluid inclusions in Qz2-V2 veins have lower K and Na and higher Mg and Ca concentrations in comparison with aqueous and aqueous-carbonic fluid inclusions in Qz1-V1 shear veins. For example, Sr and Ba concentrations are elevated in aqueous fluid inclusions in Qz2 compared with fluid inclusions in Qz1-V1, Qz3-V3, and Qz5-V4 veins (Fig. 8). Base metal concentrations range between 200 and 600 ppm in aqueous fluid inclusions (Fig. 9), with Zn being below detection limit.

V3 extensional vein arrays

Fluid inclusions in Qz3-V3 veins show the dominance of Na-K (Na > K > Ca > Mg). Alkali elements and base metals of fluid inclusions in Qz1 and Qz2 coincide with values of fluid

Table 6 Ion chromatography analyses of fluid inclusions of quartz vein types of the andesite-hosted VQZ ore body

	V1 shear veins (Qz1)			V2 extensional veins (Qz2)		V3 extensional vein arrays (Qz3)		V4 late-stage veins (Qz5)	
Na	2120	2480	1010	7950	6680	7760	7040	9080	5240
K	525	894	426	2560	2410	2860	2770	3420	2450
Li	1	1	1	3	2	2	2	2	2
Cl	8550	10,800	4750	22,700	19,400	29,300	23,800	32,600	21,000
Br	14	18	8	71	65	25	17	61	34
SO$_4$	4130	n.d.	4660	661	677	n.d.	n.d.	1770	1120
M ratio Na/K	6.8	4.7	4	5.3	4.7	4.6	4.3	4.5	3.6
M ratio Cl/Br	1410	1370	1360	715	662	2580	3210	1180	1380
M ratio Br/Cl ($\times 10^{-3}$)	0.7	0.7	0.7	1.4	1.5	0.4	0.3	0.9	0.7
M ratio Cl/SO$_4$	5.6	–	2.8	93.2	77.3	–	–	49.8	50.6
M ratio Na/Br	539	487	443	386	352	1050	1470	508	531

Data are given in ppb; *n.d.* not detected, *M* molar; analysed values do not represent true concentrations in fluid inclusions

Fig. 7 Gold vs. As plot showing low to moderate saline, aqueous two-phase FIAs trapped in Qz1-V1 shear, Qz2-V2 extensional and Qz5-V4 late-stage veins. Error bars (SD) are given in both directions (dashed lines). The arrow indicates the development of increasing Au and As concentrations in fluid inclusions of Qz1-V1 shear veins, through Qz2-V2 extensional veins to maximum Au values of Qz5-V4 late-stage veins. A and B represent populations of V1 shear veins
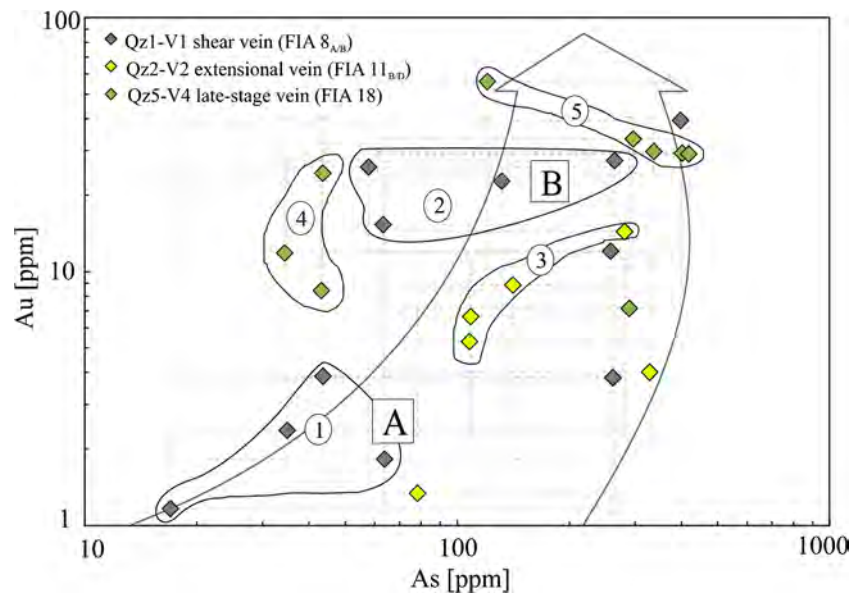
inclusions in Qz1-V1 veins (Fig. 8; ESM-5). Strontium and Ba in aqueous fluid inclusions in Qz1 reach concentrations up to 456 and 327 ppm, respectively (ESM-5). Fluid inclusions trapped in Qz3 yield less Sr and Ba than fluid inclusions in Qz1-V3 veins (ESM-5).

V4 late-stage veins

Aqueous fluid inclusions trapped in Qz5-V4 late-stage veins are characterised by much higher Na concentrations compared with aqueous and aqueous-carbonic fluid inclusions in Qz1-
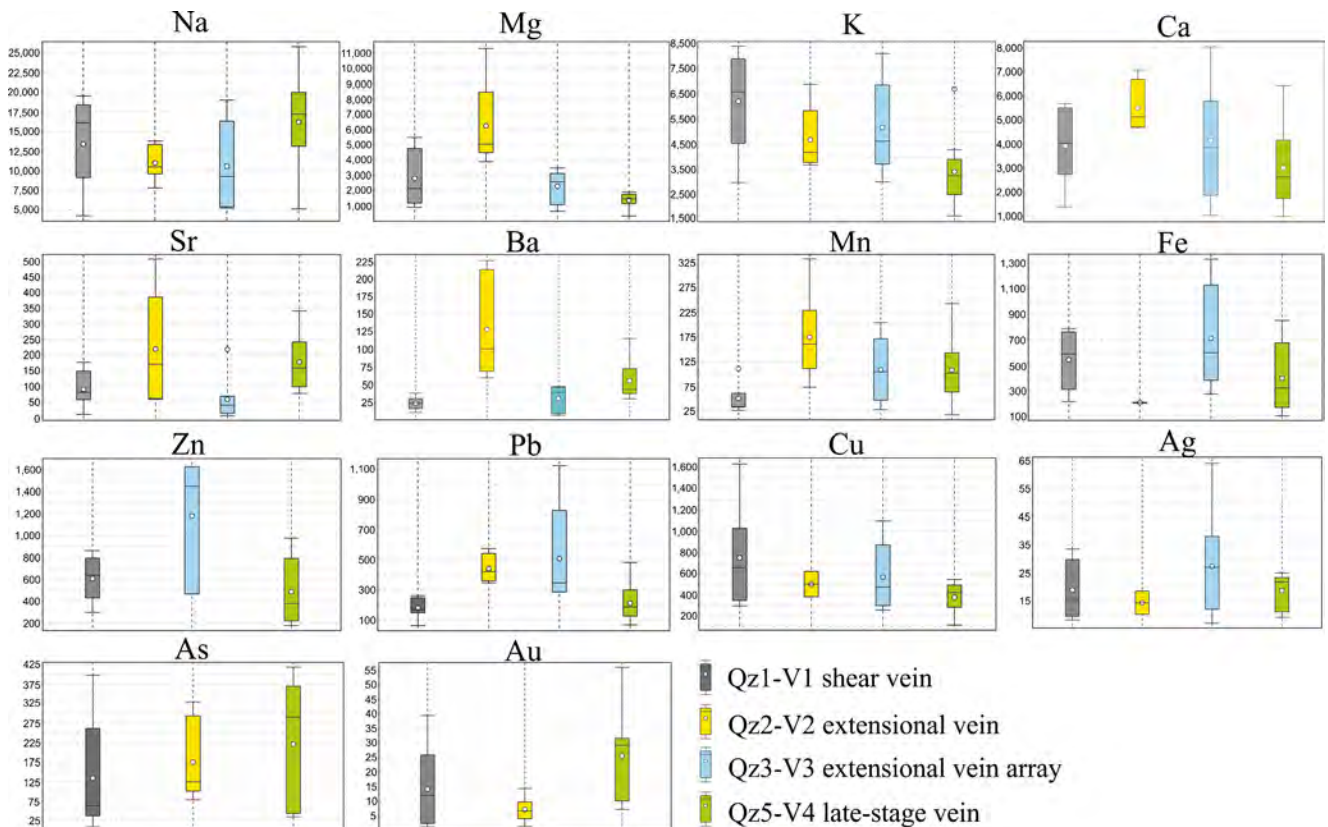
Fig. 8 Laser ablation ICP-MS results in ppm as whisker box plots for all different vein types analysed: Qz1-V1 shear, Qz2-V2 extensional, Qz3-V3 extensional vein array, Qz5-V4 late-stage veins. The central box is the middle 50% of the data from 25% quartile (Q1) to 75% quartile (Q3); whiskers are extreme values that are not outliers. Circles indicate outlier values

Fig. 9 Crushed-leach ion chromatography in fluid inclusions trapped in vein quartz of the andesite-hosted Veio de Quartzo ore body. **a** Cl/Br vs. Na/Br molar ratio. Qz2V2 veins lie close to the seawater evaporation line, whereas those of the Qz3-V3 are far above this line (inset), indicating that significant locally exchange of Na for other cations has taken place. Precipitation or dissolution of halite produces a trajectory parallel to the 1:1 line (inset). The field for the ultramafic-hosted Pampalo orogenic Au deposit (Fusswinkel et al. 2017), of low-salinity, aqueous fluids of Alpine quartz veins (Leisen et al. 2012) is also shown. Note that analyses are not charged balanced, and therefore data plot well to the left of the line in diagram. **b** Br/Cl (× 1000) molar ratio vs. Cl concentration. Greyish band shows the range of mantle/magmatic fluid ratios based on values by Jambon et al. (1995)
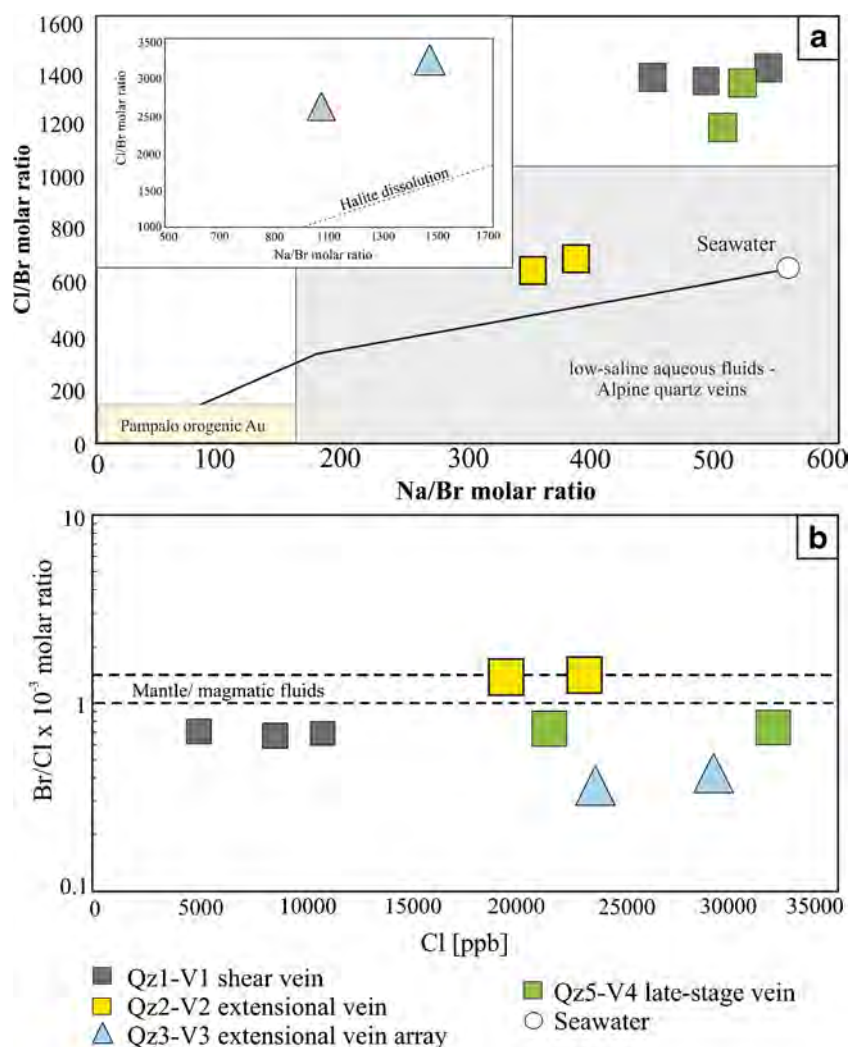
V1, Qz2-V2, and Qz3-V3 veins (Fig. 8). Strontium reaches values up to 342 ppm and Ba up to 93 ppm in aqueous fluid inclusions (ESM-5). Base metals display similar ranges compared with the other vein types.

Gold and arsenic concentration data

Figure 7 shows the correlation between As and Au of fluid inclusions trapped in V1, V2, and V4 veins. Aqueous fluid inclusions trapped in Qz1-V1 shear veins, characterised by a salinity range from of 8.1 to 13.4 wt% NaCl equiv, shows a positive correlation of As and Au, yielding two populations. Population A is characterised by relatively low As (20–200 ppm) and low Au (1–15 ppm) concentrations, whereas population B has higher As (up to 369 ppm) and Au concentrations (41 ppm) (Fig. 7; ESM-4). Moderately saline fluid inclusions (4.9 to 8.0 wt% NaCl equiv) trapped in Qz2-V2 veins show elevated As and Au concentrations (Fig. 7). These FIAs have lower Na concentrations, but an elevated K signature (ESM-4). Laser ICP-MS data of

aqueous fluid inclusions trapped in Qz5 with a salinity range from 6.4 to 9.6 wt% NaCl equiv plot at relatively elevated As and Au concentrations coinciding with the population B of V1 veins (Fig. 7) and a maximum Au value of 56 ppm (Fig. 7; ESM-4).

Discussion

Microthermometry and Raman spectroscopy

The CO_2-CH_4-rich FIAs in shear-related, andesite-hosted quartz veins of the VQZ ore body, Archaean Cuiabá gold deposit (Fig. 2a) indicate three different fluid types: (1) aqueous of low salinity (1.8–3.8 wt% NaCl equiv); (2) aqueous of moderate salinity (5.3–12.7 wt% NaCl equiv); and (3) aqueous-carbonic of low to moderate salinity (6.0–15.1 wt% NaCl equiv) with variable mol% CO_2 (30–91 mol%), CH_4 (8.6–41 mol%), N_2 (maximum values of 28 mol%) and trace concentrations of HS^- in the non-aqueous phase.

Many orogenic gold deposits hosted in metasedimentary rocks contain N_2 and/or CH_4 at concentrations similar to that of CO_2 (Bodnar et al. 2014). Overall, fluid inclusion microthermometry and Raman data are comparable to those compiled for metamorphic fluids by Ridley and Diamond (2000), Ribeiro et al. (2015) and Morales et al. (2016). Previous studies on Cuiabá by Xavier et al. (2000) and Lobato et al. (2001a, b) showed low salinity (3–6 wt% NaCl equiv), H_2O-CH_4-CO_2 ($\pm N_2 + HS$) ore-forming fluids. Methane-rich fluid inclusion types are abundant in quartz veins cross-cutting the organic carbon-bearing BIF of the Cuiabá deposit (Lobato et al. 2001c).

Ion chromatography

Three groups of ion chromatography results are depicted in Fig. 9a, with the highest Cl/Br ratios (Table 6) corresponding to fluid inclusions in the Qz3-V3 extensional vein array (inset in Fig. 9a). They all plot to the left of the seawater evaporation line, indicating that during water-rock interaction, Na in the fluid was partly exchanged for other cations (Lüders et al. 2005). This Na loss is in agreement with the LA-ICP-MS data, which demonstrate average Na concentration in FIAs decreasing from V1 shear to V2 extensional veins and V3 extensional vein arrays (Fig. 8), with renewed Na increase in FIAs trapped in Qz5-V4 late-stage veins (Figs. 8 and 9a). According to Lüders et al. (2005), Marsala et al. (2013), and Rauchenstein-Martinek et al. (2016), leaching of organic-rich sedimentary rocks increases Br and lowers the Cl/Br and Na/Br ratios, characterising data above the seawater evaporation line (as Qz2 of V2 veins; Fig. 9a). Given that in Cuiabá organic-bearing carbonaceous pelites (Fig. 2a) are associated with the Cuiabá BIF, itself containing carbonaceous matter, the low Cl/Br ratios (Table 6) may be interpreted similarly. An alternative for the low Cl/Br ratios is the mobilisation of Br during metamorphic devolatilisation of organic-rich sedimentary rocks (cf. Muramatsu and Wedepohl 1998).

Crush-leach and LA-ICP-MS studies by Leisen et al. (2012) and Fusswinkel et al. (2017) on euhedral fissure and cavity quartz samples from Alpine quartz veins and the Neoarchaean Pampalo orogenic gold deposit, respectively record lower molar Cl/Br ratios (9–150) than those of modern seawater. Low ratios are compatible with metamorphic fluids, whereby higher molar Cl/Br ratios are considered to be typical of magmatic-hydrothermal fluids (Fusswinkel et al. 2017) (500–1600). In the case of Cuiabá, there is no indication of magmatic activity associated with gold mineralisation. One alternative to explain the moderate fluid salinity (15.1 wt% NaCl equiv; Tables 3 and 4) and high Cl/Br ratios (Qz3, Fig. 9a inset) would be to invoke an evaporitic source.

For various orogenic gold deposits in Victoria, Australia, Fu et al. (2012) suggested that low-salinity, H_2O-CO_2 fluids, generated during transitional greenschist-amphibolite facies metamorphism of variably altered basalts, preserve their halogen signatures (Br/Cl ratio of $1.3 \pm 0.3 \times 10^{-3}$; Jambon et al. 1995). The Br/Cl ratios in Qz1-V1 shear and Qz5-V4 late-stage veins yield similar ranges (Table 6). The euhedral Qz3 has the comparably lowest Br/Cl ratios (Fig. 9b, Table 6). The Br/Cl ratios of fluid inclusions trapped in Qz1, Qz2, and Qz5 from V1, V2, and V4 veins are compatible with both magmatic and metamorphic fluid sources, as suggested by Böhlke and Irwin (1992) for the Oriental deposit in California ($1.2–2.4 \times 10^{-3}$). Similar Br/Cl ratios have been determined for fluid inclusions in samples of post-metamorphic gold quartz veins from the Monte Rosa gold district, NW Italy (Diamond 1993), and the Muruntau gold deposit, Uzbekistan (Graupner et al. 2006).

Major and trace element distribution in fluid inclusions

Most previous workers investigating orogenic gold deposits (Diamond 1993; McCuaig and Kerrich 1998; Ridley and Diamond 2000; Mernagh et al. 2007) have used microthermometric and spectroscopic methods of fluid inclusions to determine the composition of ore-forming hydrothermal fluids. However, there are limited LA-ICP-MS data for fluid inclusions of orogenic gold deposits and/or metamorphic fluids (Marsala et al. 2013; Rauchenstein-Martinek et al. 2014, 2016; Morales et al. 2016; Fusswinkel et al. 2017).

Chemical analysis of FIAs (Fig. 8) shows that the major elements are essentially constant for different FIAs in all vein types, suggesting that fluids were trapped under rock-buffered conditions. Alkali and alkali-earth element concentrations are similar to those obtained from other orogenic gold deposits (Diamond 1993; Wagner et al. 2016). Mono- and divalent cations such as Na, K, Ca, and Mg are responsible for lower eutectic temperatures in comparison with fluids containing only Na (Borisenko 1977). In low to moderate salinities, order of abundance Na > K > Ca > Mg, are typical in orogenic gold deposits (Yardley and Bodnar 2014; Ribeiro et al. 2015; Morales et al. 2016). Figure 8 shows a significant Na dominance in all vein types, with Mg and Ca increase in V2 veins (ESM-5). The concentrations of alkali-earth elements Sr and Ba are lower compared with alkali elements, varying among quartz vein types (Fig. 8). Carbonate alteration of andesite may have acted as a predominant process to influence fluid composition, resulting in significant Ca, Ba, and Sr concentrations, which further influenced the geochemistry of fluid inclusions in V1 shear, V2 extensional, and late-stage V4 veins (Kojonen et al. 1993; McCuaig and Kerrich 1998; Xavier et al. 2000). Alternatively, these elements may have been contributed to the fluid due to interaction with surrounding carbonaceous pelites, containing high contents of Sr (up to 183 ppm) and Ba (up to 279 ppm; Ribeiro-

Rodrigues 1998). Sodium and K metasomatism may have also been important, as well as formation of hydrothermal alteration minerals such as sericite that indicates K enrichment in the fluid (Ridley and Diamond 2000; Morales et al. 2016). In general, fluid-rock interaction resulted in Na decrease and Mg increase in V2 relative to V1 and V3 veins (Fig. 10a), whereas Sr increases in V2, V3, and V4 relative to V1 veins (Fig. 10b). A decrease of K from V1 to V2 and elevated Ca relative to Sr and K, in V2, veins compared with V1 shear veins (Fig. 10c), can be observed.

Figure 7 shows a continous As increase in FIAs from V1, through V2 and to V4 veins (ESM-3). During the early stage with V1 vein formation, As in hydrothermal fluids fluctuated from relatively low to high values (fields 1 and 2 in Fig. 7). During V2 and V4 formation, a fluid richer in As evolved (fields 3, 4, and 5; Fig. 7; ESM-4). It is noteworthy that As-rich pyrite, and not arsenopyrite, is the As-bearing sulphide phase of the hydrothermal alteration in the andesite hosting the VQZ ore body (Kresse et al. 2018).

According to Rauchenstein-Martinek et al. (2014, 2016), metamorphic fluids are commonly undersaturated in gold. Fluid inclusions trapped in quartz-tourmaline-carbonate veins of the Sigma orogenic gold deposit show a range between 0.5 and 5.0 ppm Au (Garofalo et al. 2014). The present results display median values from 12 ppm in V1, 7 ppm in V2, and up to 29 ppm Au in the V4 late-stage veins (ESM-4; Fig. 7), suggesting that peak gold precipitation took place during the V1 and V2 vein development. Formation of the pyrrhotite-dominated V4 vein may have resulted from a progressive decrease in sulphur fugacity, which enabled pyrrhotite and not pyrite to form in the late stage of hydrothermal alteration. Lower sulphur fugacity conditions may have hindered gold buffering and precipitation during V4 vein formation.

Although the lowest Au concentrations (1–4 ppm) are accompanied by low (17 ppm) to high (300 ppm) As concentrations in FIAs of the Qz1-V1 shear veins, all low, intermediate, and high Au values (7–14 ppm) in Qz2-V2 extensional veins plot in the intermediate to high As field (80–330 ppm). The Au-As correlation of V4 is highly variable, but the highest Au concentrations (56 ppm) is related to high (120 ppm) As values. During V1 development, As was partly supplied to form the early-stage As-rich pyrite only in andesite, but remained in the fluid, i.e., did not precipitate to form arsenopyrite during the V2 and V4 late-stage vein formation, which is evidenced by the absence of arsenopyrite.

Characteristics of the ore-forming fluids

Fluid precipitation processes Aqueous and aqueous-carbonic FIAs trapped in different quartz and vein types in the andesite-hosted VQZ ore body contain a vapour phase of ± 10 vol%, indicating homogenous fluids (miscible) at the time of trapping. Given that only fluid inclusions trapped in aqueous FIA 2_D, in Qz2-V2 extensional veins, display homogenisation into vapour, but decrepitate before final homogenisation, the evidence for intermittent-phase immiscibility as a possible fluid precipitation process is equivocal. According to Anderson et al. (1992), a positive correlation between Th_{TOT} and salinity is compelling evidence for fluid mixing of two or more distinct miscible fluids. Based on the distribution of data in Fig. 6a–c, the evidence for mixing is vague. Hydrothermal fluids at Cuiabá either unmixed at a deeper crustal level, with the low-density CO_2 vapour-rich fluid inclusions escaping to surface, or alternatively, heterogeneous fluids with varying CO_2 and/or CH_4 proportions moved up to fault zones and cooled according to the local geothermal gradient.
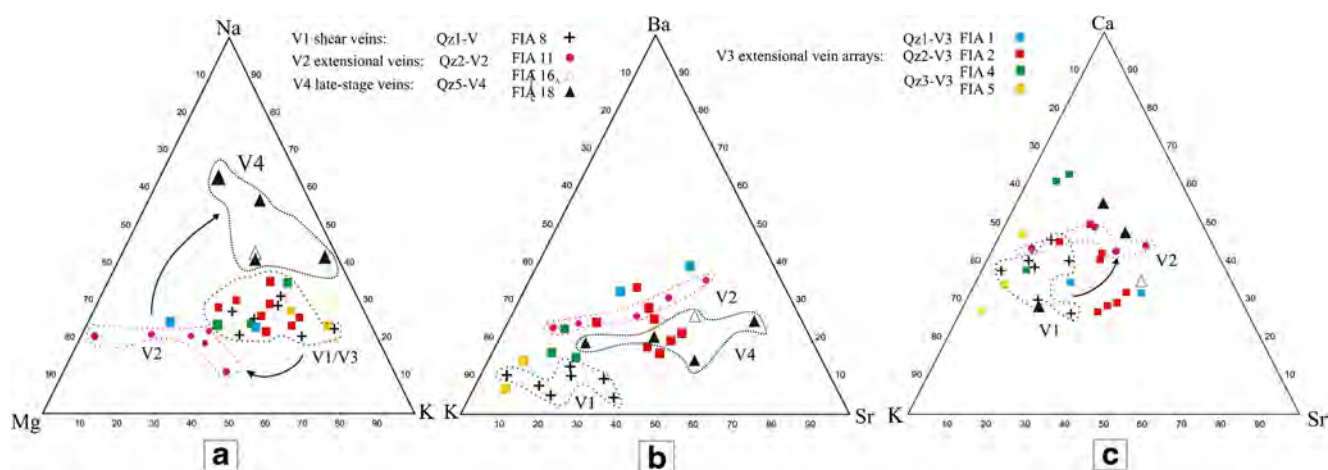
Fig. 10 Normative plots of alkali and alkali-earth elements of LA-ICP-MS analyses from aqueous and aqueous-carbonic FIAs of V1 shear, V2 extensional, V3 extensional vein array, and V4 late-stage vein: **a** Na-Mg-K, **b** Ba-K-Sr, and **c** Ca-K-Sr. The Na- and K-rich fluid (V1 shear veins) evolved to a Mg-Sr-Ca-rich and Na-poor fluid (V2 extensional veins). New Na- and K-rich fluid is related to the V4 late-stage vein. The V3 extensional array veins, immersed in the V1 shear vein type, show similar composition to V1

Evolution of volatiles in veins associated with wall rock reactions Laser Raman data and their quantification show variable amounts of CH_4 (8.6–41 mol%), CO_2 (30–91 mol%), and N_2 (28 mol%) in the non-aqueous phase of individual FIAs trapped in Qz1-V1, Qz3-V3, and Qz5-V4 (except CO_2 is lacking in Qz2-V2 veins). Methane and CO_2 trapped in fluid inclusions from gold-bearing veins are common in orogenic gold systems (Ho et al. 1985) and can be explained by either metamorphic reactions involving carbonates with H_2, as well as serpentinisation reactions (Xavier et al. 2000; Gaboury 2013, 2019). Nitrogen, in contrast, is only rarely detected and therefore, the significant amount of N_2 in aqueous-carbonic FIAs trapped in the Qz3-V3 extensional vein array requires an explanation. Various authors (e.g., Andersen et al. 1993) provided evidence that N_2 can be sourced by (i) breakdown of organic matter from sedimentary rocks where N_2 can be fixed in K-bearing silicates (mica), (ii) hydrothermal alteration of NH_4^+-bearing silicates and formation of N_2, or (iii) primary N_2 liberated from magma or through metamorphism of the lower crust.

Fluid source Low to moderate salinities (max 15 wt% NaCl equiv) and moderate to high homogenisation and decrepitation temperatures of up to ~ 380 °C (Fig. 6; Tables 4 and 5) of the ore-forming hydrothermal fluids are compatible with those associated with mesozonal orogenic gold deposits (Ridley and Diamond 2000; Goldfarb and Groves 2015; Groves et al. 2019). Existing Stable isotope data at Cuiabá are consistent with the hydrothermal fluids being dominantly of metamorphic origin (Lobato et al. 2001c) based on (i) oxygen isotope data on carbonates of the Cuiabá BIF and andesite range between + 9 and + 10 ‰, which are compatible with metamorphic fluids (Taylor 1987); (ii) $\delta^{34}S$ signature of pyrite and pyrrhotite ranges between 1.4 and 5.6 ‰ (Lobato et al. 2001c; Kresse et al. 2018), indicating a sedimentary sulphur source (Farquhar et al. 2000); (iii) carbon isotope data on carbonate minerals of the Cuiabá BIF and andesite are in the range of 0.7 to − 8.5‰ and − 5.5 to − 8.4 ‰, respectively, which are similar to other Archaean greenstone belt-hosted orogenic gold deposits worldwide (De Ronde et al. 1997), and those are interpreted of metamorphic origin. Kresse et al. (2018) conducted sulphur isotope analyses on hydrothermal pyrite and concluded that sedimentary rocks were a significant source for sulphur. Sedimentary rocks make up much of the local stratigraphy in the Rio das Velhas greenstone belt. Studies on the metasedimentary schist-hosted Macraes orogenic gold deposit in the Otago goldfield by Craw and MacKenzie (2016) have shown that this narrow range in oxygen isotope values is characteristic of hydrothermal fluids that have interacted with schistose host rocks and is widespread in hydrothermal systems throughout the Otago schist belt.

Significance of base metal concentrations

Cuiabá is low in base metal minerals, which is compatible with orogenic gold systems (Phillips and Powell 2010; Goldfarb and Groves 2015). Typical low-salinity metamorphic fluids are unlikely candidates for forming large base metal occurences and have average Zn, Pb, and Cu values in the range of 1–10 ppm (Phillips and Powell 2010; Wagner et al. 2016). The FIAs in the Cuiabá vein system have elevated Zn, Pb, and Cu concentrations in comparison with sedimentary systems. However, our data are compatible with the predominance of metamorphic fluids.

Anomalous base metal contents are also registered in pyrite hosted in BIF, andesite, and carbonaceous pelite within the Cuiabá deposit (Fig. 2) (Kresse et al. 2018), a feature equally reported by Oliver et al. (2015) for the Neoproterozoic Paracatu sedimentary rock (black shale)–hosted orogenic gold deposit. The sulphur isotope ratios obtained for pyrite and pyrrhotite by Kresse et al. (2018) indicate that the metamorphic hydrothermal fluids (Fig. 12) interacted and exchanged chemical components with the sedimentary rocks in the Cuiabá area during their ascent. Two scenarios may be envisaged: equilibration with the wallrocks, and/or mixing with basinal brines originating from sedimentary, as suggested by Pb and Sr isotope studies on pyrite at Cuiabá; however, the salinity data are not compatible with this latter hypothesis. Lead isotope analyses of sulphide minerals show a limited spread of data (Lobato et al. 2001b, c), indicating the formation of gold mineralisation during the late Neoarchaean between 2.75 and 2.70 Ga. Although the interpretation of Pb isotope data is uncertain (Lobato et al. 2001c), Pb values may imply a derivation from a mixture of old continental crust and greenstone belt sedimentary rocks (Noce et al. 2007). Existing Sr isotope data ($^{87}Sr/^{86}Sr$) of BIF-hosted pyrite from the Cuiabá deposit support the influence of the continental crust related to the fluid geochemistry (Lobato et al. 2001c). As Archaean fluids are typically characterised by low Sr isotope ratios, the recorded relatively high ratio of 0.707909 may indicate that Sr of the mineralising fluids was derived from the upper continental crust (Lobato et al. 2001a, b; Noce et al. 2007).

The geochemical data set of FIAs at Cuiabá, Lamego, and Córrego do Sítio in the QF (Fig. 1) demonstrate that the major and trace element compositions are nearly identical with few discrepancies such as Cu, Pb, Ag, and Au (Morales et al. 2016). The Lamego and Córrego do Sítio deposits show elevated base metal concentrations from 100 to 1000 ppm (Fig. 11; Table 7).

The Cuiabá Th_{TRAP} and moderate salinity data obtained in all vein types correlate positively with higher base metal concentrations than typically encountered in orogenic gold deposits (Table 7). Minimum Th_{TRAP} in similar salinity ranges are obtained for Lamego (200–370 °C) and Córrego do Sítio (310–395 °C) (Ribeiro et al. 2015; Morales et al. 2016).

Fig. 11 Correlation plot of Zn-Pb and Zn-Cu concentrations of different types of crustal fluids in comparison with fluid inclusion LA-ICP-MS data of the andesite-hosted quartz veins at the Cuiabá deposit. References: Lamego orogenic Au deposit and Córrego do Sítio orogenic Au district (Morales et al. 2016), El Teniente and Butte Porphyry Cu-Mo deposit, magmatic hydrothermal fluids (Klemm et al. 2007), Bingham Canyon Porphyry Cu-Au deposit, magmatic hydrothermal fluids (Seo et al. 2012), Central Alps, metamorphic fluids (Rauchenstein-Martinek et al. 2014, 2016), granite-hosted smoky quartz fissure vein, Binn Valley—mixed metamorphic-evaporitic fluids (Klemm et al. 2004). Low-temperature-saline brines of Sediment-hosted Pb-Zn deposits (Wilkinson et al. 2009). Range of crustal fluids from Yardley (2005). Abbreviation: QV quartz vein, CP carbonaceous pelite, MG metagreywacke, MD mafic dike
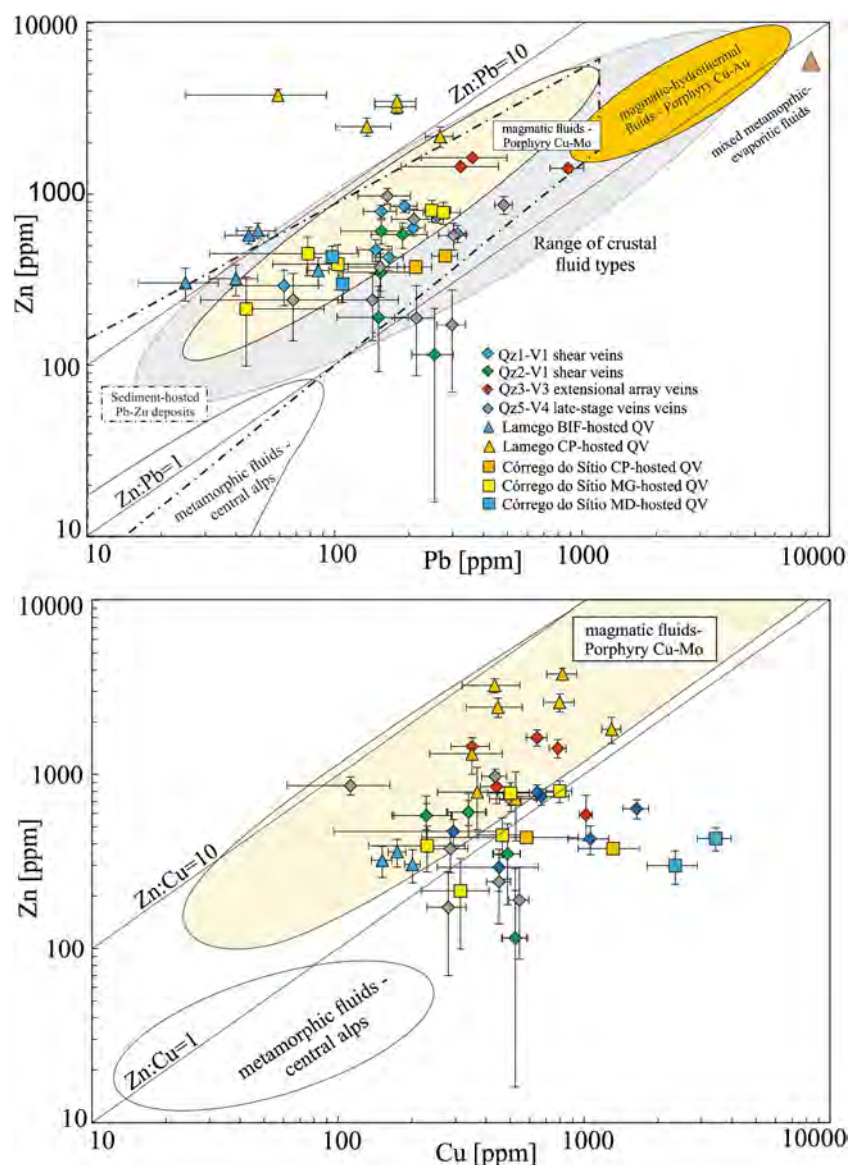
Taking these data into account (Fig. 11; Table 7), it appears that FIAs trapped in shear and extensional veins at Cuiabá, Lamego, and Córrego do Sítio display significant base metal concentrations in comparison with data of metamorphic fluids related to orogenic belts elsewhere (Marsala et al. 2013; Rauchenstein-Martinek et al. 2014, 2016; Wagner et al. 2016), and orogenic gold deposits in general (Fusswinkel et al. 2017).

Sedimentary rocks may be considered an essential source of gold and fluids (Pitcairn et al. 2006; Large et al. 2011), whereby the BIF-surrounding carbonaceous pelite may represent a possible source for base metals (Fig. 2a). Large et al. (2011) indicated that metalliferous black shales are commonly enriched in metals including Mo, V, Ni, Cr, Zn, As, Cu, and Pb. Xavier et al. (2000) and Lobato et al. (2001b) show that the relevance of carbonaceous pelite and fluidrock interactions

for some Rio das Velhas greenstone belt–hosted deposits, and Morales et al. (2016) highlight the carbonaceous pelites at the Córrego do Sítio district and Cuiabá deposits as a partial sources of metals; however, these units only amount to a minor portion of their rock packages. Whole-rock geochemical analyses of carbonaceous pelites at Cuiabá which yield Zn values up to 630 ppm, Pb in the order of 56 ppm, and As reach up to 162 ppm (Ribeiro-Rodrigues 1998). Andesite reveals Zn, Pb, and As concentrations of 218 ppm, 16 ppm, and 15 ppm, respectively. Gold concentrations in carbonaceous pelites and andesite are between 8 and 10 ppb. Based on data of Baltazar and Zucchetti (2007), Martins et al. (2016) calculated an approximate thickness of 5550 m of clastic, clastic-chemical, and volcaniclastic sedimentary rocks, making the Rio das Velhas a sedimentary-rich greenstone belt. The Archaean Cuiabá orogenic gold deposit is over- and underlain

Table 7 Median base metal concentrations and corresponding average salinity of aqueous and aqueous-carbonic FIAs of orogenic gold deposits in the QF and Telfer Cu-Au deposit

Deposit	Quartz veins	Average salinity (wt% NaCl equiv)	Median base metal concentrations (ppm)		
			Cu	Zn	Pb
Cuiabá–VQZ ore body	Qz1-V1 shear veins	9.3	864	637	190
		5.4	373	632	150
		2.7	312	292	62
		11.8	729	720	253
	Qz2-V1 shear veins	5.6	488	350	188
	Qz2-V2 extensional veins	6.6	501	–	403
	Qz3-V3 extensional vein arrays	5.8	474	–	286
		7.0	496	1540	342
		9.2	1020		977
	Qz5-V4 late-stage veins	3.2	545	190	214
		6.2	286	274	152
		8.0	443	644	186
Lamego, Cabeça de Pedra ore body	BIF-hosted Qv	2.4	176	313	29
		3.7	174	575	49
	CP-hosted Qv	9.8	446	2430	257
		10.4	527	2340	191
Córrego do Sítio, Carvoaria Velha deposit	CP-hosted Qv	5.8	1310	376	213
		8.6	583	435	280
	MG-hosted Qv	4.5	465	449	103
	MD-hosted Qv	15.0	2880	365	103
Telfer Intrusion-related Cu-Au deposit, Australia	Aqueous-carbonic FIAs	10.0	621	328	196
		15.0	–	354	405
	Aqueous FIAs	10.0	171	272	44
		14.5	1270	378	1200

Lamego and Corrego do Sitio dataset (Morales et al. 2016), Telfer (Schindler et al. 2016). *CP* carbonaceous pelite, *MG* Metagreywacke, *MD* Mafic dike, *Qv* Quartz vein

by these thick sequences of lithologically variable, supracrustal sedimentary rocks. Similar Archaean terrains, such as the Yellowknife Supergroup, are also dominated by sedimentary rocks (Helmstaedt and Padgham 1986), composed of widespread turbidites (Burwash-Wash Formations; Taylor and McLennan 1985). These contrast with other volcanic-dominated greenstone belts and associated orogenic gold deposits (Anhaeusser 2014).

Cuiabá vein and fluid model

The proposed model for hydrothermal fluid flow and precipitation of metals, including gold, at the Cuiabá deposit is based on the detailed investigation of the andesite shear zone–hosted quartz veins and the physico-chemical constraints obtained by the present fluid inclusion investigation. We propose a two-step hydrothermal model that involves the development of (1) V1 to V3 veins by an early-stage, aqueous-carbonic, high-temperature fluid, with minimum Th_{TRAP} at 290 °C (Qz2-

V3) to a maximum Th_{TRAP} at 360 °C (Qz1-V1) and (2) breccia-style V4 veins, which formed by an evolved, late-stage, aqueous-carbonic, low temperature fluid with a mean Th_{TRAP} at 260 °C. The evolution of the vein system, including the hydrothermal fluids and gold mineralisation, is illustrated in Fig. 12 and given in the following section. Overall, the two-step hydrothermal fluid model is interpreted to reflect four pulses of hydrothermal fluids during the evolution of the paleohydrothermal system. Fluid pulses 1 to 3 relate to the first hydrothermal stage, whereas fluid pulse 4 relates to the second hydrothermal stage (Fig. 12). The first hydrothermal stage contains:

1. Pulse 1: An early, first hydrothermal fluid pulse is represented by Na-K-rich, aqueous, and aqueous-carbonic FIAs of low and moderate salinity with $CO_2 > CH_4$ (N_2 free) (Fig. 12). These oxidised fluids have base metal contents between 60 to 1600 ppm and median As and Au values of 64 ppm and 12 ppm, respectively. They are trapped in Qz1-V1 shear and Qz1-V2 extensional

First hydrothermal stage

Initial shearing ⟶ *V1 and V2 veins emplacement*

① Andesite-hosted VQZ orebody

② Andesite-hosted VQZ orebody

Mineralized Qz1-V1 shear veins

<u>Salinity:</u> 2.0-4.0 wt % NaCl equiv aqueous, and 5.0-13.5 wt % NaCl equiv aqueous and aqueous-carbonic FIAs

<u>Temperature:</u> T_{DECREP} 280 to 310 °C; Th_{TRAP} 360 to 390 °C

<u>Volatiles:</u> $CO_2 + CH_4$

<u>Composition:</u> Na-K-rich; Zn, Pb and Cu content between 60 and 1,600 ppm; median As (64 ppm) and Au (12 ppm)

Fluid flow

Qz2-V2 extensional veins

<u>Salinity:</u> ~ 6.5 wt % NaCl equiv aqueous FIAs

<u>Temperature:</u> Th_{TOT} 260 to 290 °C; Th_{TRAP} 330 to 360 °C

<u>Volatiles:</u> negligible content of CO_2 and CH_4

<u>Composition:</u> Mg-Ca-Sr-Ba-rich and Na-K-poor fluid; Pb and Cu content between 200-600 ppm; higher median As (125 ppm) and lower Au (7 ppm) than FIAs of Qz1-V1

Progressive deformation/Boudinage and folding + V3 veins emplacement

③ Andesite-hosted VQZ orebody

Qz1 to Qz4 evolution of the first hydrothermal stage

Qz3-V3 extensional array veins

<u>Salinity:</u> ~3.0 wt % NaCl equiv aqueous, and 6.0-9.0 wt % NaCl equiv aqueous and aqueous-carbonic FIAs

<u>Temperature:</u> T_{DECREP} 270 to 350 °C; Th_{TRAP} 290 to 360 °C

<u>Volatiles:</u> $CH_4 + CO_2 + N_2$

<u>Composition:</u> Alkali and alkali-earth content similar to early-stage Qz1; elevated Zn, Pb and Ag content than in Qz1/Qz2

Second hydrothermal stage

④ Andesite-hosted VQZ orebody

Fluid flow

V4 veins emplacement

Qz5-V4 late stage veins
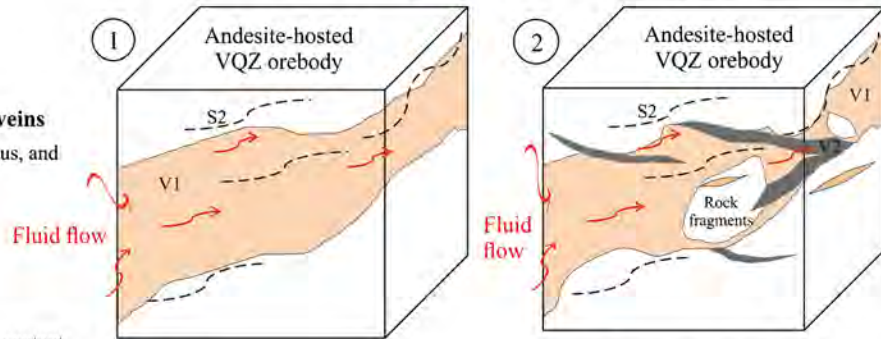
<u>Salinity:</u> 2.5-4.0 wt % NaCl equiv aqueous, and 6.5-11.0 wt % NaCl equiv aqueous and aqueous-carbonic FIAs

<u>Temperature:</u> Th_{TOT} 190 to 200 °C; Th_{TRAP} 240 to 270 °C

<u>Volatiles:</u> $CO_2 + CH_4$

<u>Composition:</u> Na-K-As-rich; elevated Ca, Sr and Ba content Zn, Cu, Pb content between 100 and 1,000 ppm; highest median As (290 ppm) and Au values (29 ppm)

Fig. 12 Schematic evolution model of the Cuiabá veins and VQZ orebody, including FIAs characteristics of mineralised Qz1-V1 shear vein, Qz2-V2, and Qz3-V3 extensional vein, corresponding to the first hydrothermal stage; Qz5-V4 late-stage vein of the second hydrothermal stage. The schematic reproduction of a photomicrography of quartz -type evolution shows Qz1, Qz2, and Qz3. The Qz4 is considered a recrystallisation product of Qz3 in V3 extensional array vein

veins (the veins with visible gold), with mean Th_{TRAP} between 350 and 380 °C. These temperatures are similar to the arsenopyrite formation temperature between 300 and 390 °C (Kresse 2018).

2. Pulse 2: The second hydrothermal fluid pulse is represented by aqueous FIAs of moderate salinity (Fig. 12). These are Mg-Ca-Sr-Ba-rich and Na-K-poor, with base metal contents between 200 and 600 ppm and median As (125 ppm) and medium Au (7 ppm) values. These are trapped in Qz2-V2 extensional veins, with Th_{TRAP} ranging from 290 to 360 °C.

3. Pulse 3: The third hydrothermal fluid pulse is base metal rich and represented by Na-K-Ca-rich, aqueous, and aqueous-carbonic FIAs of low and moderate salinity and $CH_4 > CO_2 = N_2$ (Fig. 12). The base metal content ranges from 300 to 1500 ppm, and FIAs trapped in Qz3-V3 extensional vein arrays, have Th_{TRAP} between 290 and 340 °C.

The second hydrothermal stage includes:

4. Pulse 4: The forth hydrothermal pulse is characterised by aqueous and aqueous-carbonic FIAs of low and moderate salinity (Figs. 6 and 12). It is Na-K-rich, displays elevated Ca, Sr, and Ba values, and shows base metal contents between 100 and 1000 ppm, with very high median As (290 ppm) and Au (29 ppm) values. Pulse 4 fluids are trapped in Qz5-V4 extensional, breccia-style veins with significant lower Th_{TRAP} between 240 and 270 °C when compared wtih the other fluid pulses.

The low to moderate saline, aqueous-carbonic fluid of Pulse 1 is suggested to represent the main mineralising fluid in V1 shear and V2 extensional veins, which led to gold precipitation. Since fluid inclusions in V1 shear veins, as well as in V2, V3, and V4 extensional veins, are very similar with regard to compositional types and physico-chemical conditions, the fluid chemistry probably did not change significantly from the first (Pulses 1–3) to the second (Pulse 4) hydrothermal stage during the Archaean deformation history. The Au concentration in FIAs trapped in each vein type (Qz1-V1 shear, Qz2-V2 extensional, Qz5-V4 late-stage veins) suggest the following: (1) an early precipitation of Au as native gold from a Na-K-As-rich hydrothermal fluid due to intermittent phase immiscibility at depth, and/or partial mixing, and (2) a late-stage Au-bearing Na-K-As-rich hydrothermal fluid, which was not able to precipitate gold in pyrrhotite-rich V4

late-stage veins probably due to insufficient total concentration of sulphur ($m_{\sum S}$).

Conclusions

The detailed investigations on hydrothermal fluids in the different vein types at Cuiabá revealed the following:

1. The Cuiabá quartz veins, hosted in the footwall andesite of the Veio de Quartzo ore body, encompass V1 shear, V2 extensional (V1 and V2 with visible gold), V3 extensional vein array and V4 extensional (breccia-style) veins. An early-stage, anhedral Qz1 evolves to a granoblastic Qz2, and a late-stage, euhedral Qz3 during a first hydrothermal stage, which is represented by V1, V2, and V3 veins. The breccia-style V4 veins are interpreted to be related to a second hydrothermal stage, during which the anhedral Qz5 develops, bearing morphological and fluid inclusion characteristics similar to Qz1.

2. Microthermometric data show that the ore-forming fluid has the signature of typical orogenic gold fluids, i.e., low to moderate salinity (4.0–10.0, locally up to 15 wt% NaCl equiv) containing variable amounts of CO_2, CH_4, N_2 and minor HS^-.

3. The geochemical data in FIAs display the following fluid-rock interactions inbetween quartz veins: (i) Na decreases in V2 relative to V1 and V3 veins; (ii) Sr increases in V3 and V2 relative to V1; (iii) K continously decreases from V1 to V4; and (iv) Ca is relatively higher to Na and K concentrations in V2 in comparison with V1, V3, and V4.

4. Possible intermittent-phase immiscibility as well as heterogeneous entrapment resulting from intermittent partial mixing of two or more ore fluids may be considered the principal fluid processes leading to the formation of the Cuiabá orogenic gold deposit.

5. A distinction to the typical orogenic gold fluids is the Cu, Zn, and Pb enrichment encountered in fluid inclusions of Cuiabá, which are also similar to other deposits hosted in the Rio das Velhas greenstone belt (Lamego and Córrego do Sítio). These values, in the range of 100 to 1000 ppm, may have been caused by interaction with: (i) metalliferous black shales and (ii) the (meta) sedimentary rocks that dominate the Rio das Velhas greenstone belt.

6. The fluid inclusion results provide an opportunity to classify shear and extensional veins and help in identifying the evolution of the fluids forming the different vein types in the orogenic gold deposits of the QF. The similar geochemical affinity of the Cuiabá veins, hosted in the footwall andesite, suggest they are all part of the same hydrothermal event. This event is characterised by two main stages, with the first displaying changing physico-chemical parameters due to fluid-rock reactions and fluid

dynamic processes. This is particularly apparent in the recorded Au concentrations of FIAs trapped in the main hosts for the mineralisation of the VQZ ore body (Qz1-V1 shear and Qz2-V2 extensional veins), but also in the Qz5-V4 late-stage veins, which may represent a paragenetically late and second Archaean hydrothermal fluid stage.

References

Allan MM, Yardley BW, Forbes LJ, Shmulovich KI, Banks DA, Shepherd TJ (2005) Validation of LA-ICP-MS fluid inclusion analysis with synthetic fluid inclusions. Am Min 90:1767–1775

Andersen T, Austrheim H, Burke EAJ, Elvevold S (1993) N_2 and CO_2 in deep crustal fluids: evidence from the Caledonides of Norway. Chem Geol 108:113–132

Anderson MR, Rankin AH, Spiro B (1992) Fluid mixing in the generation of mesothermal gold mineralisation in the Transvaal Sequence, Transvaal, South Africa. Eur J Mineral 4:933–948

AngloGold Ashanti (2018) Resources and Reserves Annual Report 2018, Cuiabá Mine https://www.anglogoldashanti.com/investors/annual-reports/

Anhaeusser CR (2014) Archean greenstone belts and associated granitic rocks–a review. J Afr Earth Sci 100:684–732

Babinski MF, Chemale JR, Van Schmus WR (1991) Geocronologia Pb/Pb em rochas carbonáticas do Supergrupo Minas, Quadrilátero Ferrífero, Minas Gerais. Congresso Brasil Geoquimica 3:628–631

Baltazar O, Zucchetti M (2007) Lithofacies associations and structural evolution of the Archean Rio das Velhas greenstone belt, Quadrilátero Ferrífero, Brazil: a review of the setting of gold deposits. Ore Geol Rev 32:471–499

Bodnar R, Vityk MO (1994) Interpretation of microthermometric data for H_2O-NaCl fluid inclusions: fluid inclusions in minerals: methods and applications, Short course, pp 117–130

Bodnar RJ, Lecumberri-Sanchez P, Moncada D, Steele-MacInnis M (2014) Fluid inclusions in hydrothermal ore deposits. Treatise on Geochemistry, 2nd edn. Elsevier, Oxford, pp 119–142

Böhlke JK, Irwin JJ (1992) Laser microprobe analyses of Cl, Br, I, and K in fluid inclusions: implications for sources of salinity in some ancient hydrothermal fluids. Geochim Cosmochim Acta 56:203–225

Borisenko A (1977) Study of the salt composition of solutions in gas-liquid inclusions in minerals by the cryometric method. Sov Geol Geophys 18:11–18

Brown PE, Hagemann SG (1995) MacFlinCor and its application to fluids in Archean lode-gold deposits. Geochim Cosmochim Acta 59:3943–3952

Burke EAJ (2001) Raman microspectrometry of fluid inclusions. Lithos 55:139–158

Cabral AR, Zeh A, Koglin N, Gomes AAS, Viana DJ, Lehmann B (2012) Dating the Itabira iron formation, Quadrilátero Ferrífero of Minas Gerais, Brazil, at 2.65 Ga: depositional U Pb age of zircon from a metavolcanic layer. Precambrian Res 204-205:40–45

Craw D, MacKenzie D (2016) Macraes orogenic gold deposit (New Zealand): origin and development of a world class gold mine. Springer. https://doi.org/10.1007/978-3-319-35158-2_7

De Ronde CEJ, Der Channer DM, Spooner ETC (1997) Archaean fluids. In: De Wit MJ, Ashwal LD (eds) Greenstone belts. Clarendon Press, Oxford, pp 309–335

Diamond LW (1993) Post-metamorphic gold-quartz veins from NW Italy: the composition and origin of the ore fluid. Mineral Mag 57:407–422

Dorr JVN (1969) Physiographic, stratigraphic, and structural development of the Quadrilátero Ferrífero. Minas Gerais, Brazil, pp 2330–7102

Farquhar J, Bao H, Thiemens M (2000) Atmospheric influence of Earth's earliest sulfur cycle. Science 289:756–758

Fu B, Kendrick MA, Fairmaid AM, Phillips D, Wilson CJ, Mernagh TP (2012) New constraints on fluid sources in orogenic gold deposits, Victoria, Australia. Contrib Mineral Petrol 163:427–447

Fusswinkel T, Wagner T, Sakellaris G (2017) Fluid evolution of the Neoarchean Pampalo orogenic gold deposit (E Finland): constraints from LA-ICPMS fluid inclusion microanalysis. Chem Geol 450:96–121

Gaboury D (2013) Does gold in orogenic deposits come from pyrite in deeply buried carbon-rich sediments? Insight from volatiles in fluid inclusions. Geology 41:1207–1210

Gaboury D (2019) Parameters for the formation of orogenic gold deposits. Appl Earth Sci (Trans Inst Min Metall B). https://doi.org/10.1080/25726838.2019.1583310

Garofalo PS, Fricker MB, Günther D, Bersani D, Lottici PP (2014) Physical-chemical properties and metal budget of Au-transporting hydrothermal fluids in orogenic deposits. Geol Soc London Spec Publ 402:71–102

Goldfarb RJ, Groves DI (2015) Orogenic gold: common or evolving fluid and metal sources through time. Lithos 233:2–26

Goldstein RH, Reynolds TJ (1994) Systematics of fluid inclusions in diagenetic minerals. SEPM short course 31. The Mineralogical Association of Canada, Tulsa

Graupner T, Niedermann S, Kempe U, Klemd R, Bechtel A (2006) Origin of ore fluids in the Muruntau gold system: constraints from noble gas, carbon isotope and halogen data. Geochim Cosmochim Acta 70:5356–5370

Groves DI, Goldfarb RJ, Gebre-Mariam M, Hagemann S, Robert F (1998) Orogenic gold deposits: a proposed classification in the context of their crustal distribution and relationship to other gold deposit types. Ore Geol Rev 13:7–27

Groves DI, Santosh M, Deng J, Wang Q, Yang L, Zhang L (2019) A holistic model for the origin of orogenic gold deposits and its implications for exploration. Mineral Deposita:1–18. https://doi.org/10.1007/s00126-019-00877-5

Guillong M, Meier DL, Allan MM, Heinrich CA, Yardley BW (2008) Appendix A6: SILLS: a MATLAB-based program for the reduction of laser ablation ICP-MS data of homogeneous materials and inclusions. Mineral Assoc Can Short Course 40:328–333

Hagemann SG, Brown PE (1996) Geobarometry in Archean lode-gold deposits. Eur J Mineral 8:937–960

Hagemann SG, Cassidy KF (2000) Archean orogenic lode gold deposits. Rev Econ Geol 13:9–68

Helmstaedt H, Padgham WA (1986) Stratigraphic and structural setting of gold-bearing shear zones in the Yellowknife greenstone belt. Can Inst Min 38:322–345

Ho SE, Groves DI, Phillips GN (1985) Fluid inclusions as indicators of the nature and source of fluids and ore depositional conditions for Archaean gold deposits of the Yilgam Block, Western Australia. Trans Geol S S Afr 85:149–158

Jacobs GK, Kerrick DM (1981) Methane: an equation of state with application to the ternary system H_2O-CO_2-CH_4. Geochim Cosmochim Acta 45:607–614

Jambon A, Déruelle B, Dreibus G, Pineau F (1995) Chlorine and bromine abundance in MORB: the contrasting behaviour of the Mid-Atlantic Ridge and East Pacific Rise and implications for chlorine geodynamic cycle. Chem Geol 126:101–117

Klemm L, Pettke T, Graeser S, Mullis J, Kouzmanov K (2004) Fluid mixing as the cause of sulphide precipitation at Albrunpass, Binn Valley, Central Alps. Swiss Bull Mineral Petrol 84:189–212

Klemm LM, Pettke T, Heinrich CA, Campos E (2007) Hydrothermal evolution of the El Teniente deposit, Chile: porphyry Cu-Mo ore deposition from low-salinity magmatic fluids. Econ Geol 102: 1021–1045

Kojonen K, Johanson B, O'Brien HE, Pakkanen L (1993) Mineralogy of gold occurrences in the late Archean Hattu schist belt, Ilomantsi, eastern Finland. Spec Pap Geological Survey of Finland 17:233–271

Kresse C (2018) Isotopic, fluid inclusion and LA-ICP-MS studies on the world-class BIF hosted Cuiabá gold deposit, Rio das Velhas greenstone belt, Quadrilátero Ferrífero, MG: implications for the mineralizing fluid reservoirs. Dissertation, Universidade Federal de Minas Gerais

Kresse C, Lobato LM, Hagemann SG, Figueiredo e Silva RC (2018) Sulfur isotope and metal variations in sulfides in the BIF-hosted orogenic Cuiabá gold deposit, Brazil: implications for the hydrothermal fluid evolution. Ore Geol Rev 98:1–27

Ladeira EA (1991) Genesis of gold in QuadriláteroFerrífero: a remarkable case of permanency, recycling and inheritance: a tribute to DjalmaGuimarães, Pierre Routhier and Hans Ramberg. Brazil Gold 91:11–30

Large RR, Bull SW, Maslennikov VVA (2011) Carbonaceous sedimentary source-rock model for Carlin-type and orogenic gold deposits. Econ Geol 106:331–358

Leisen M, Boiron MC, Richard A, Dubessy J (2012) Determination of Cl and Br concentrations in individual fluid inclusions by combining microthermometry and LA-ICP-MS analysis: implications for the origin of salinity in crustal fluids. Chem Geol 330:197–206

Lobato LM, Vieira FWR, Ribeiro-Rodrigues LC, Pereira LM, Menezes MG, Junqueira PA, Pereira SL (1998) Styles of hydrothermal alteration and gold mineralization associated with the Nova Lima Group, Quadrilátero Ferrífero: part II, the Archean mesothermal gold-bearing hydrothermal system. Braz J Geol 28:355–366

Lobato LM, Ribeiro-Rodrigues LC, Zucchetti M, Noce CM, Baltazar O, da Silva L, Pinto C (2001a) Brazil's premier gold province. Part I: the tectonic, magmatic, and structural setting of the Archean Rio das Velhas greenstone belt, Quadrilátero Ferrífero. Mineral Deposita 36: 228–248

Lobato LM, Ribeiro-Rodrigues LC, Vieira F (2001b) Brazil's premier gold province. Part II: geology and genesis of gold deposits in the Archean Rio das Velhas greenstone belt, Quadrilátero Ferrífero. Mineral Deposita 36:249–277

Lobato LM, Ribeiro-Rodrigues LC, Costa MNS, Martins R, Lehne E, Alves JV, Tassinari CG, Vieira FWR, Biasi EE, Silva RCF, Pereira VCA, Noce CM (2001c) Geologia do depósito de ouro Cuiabá, Quadrilátero Ferrífero, Minas Gerais, Caracterização de depósitos auríferos em distritos minerais brasileiros, Departamento Nacional da Produção Mineral/Agência para o Desenvolvimento Tecnológico da Indústria Mineral Brasileira, pp 3–77

Lobato LM, Santos JOS, McNaughton N, Fletcher I, Noce CM (2007) U-Pb SHRIMP monazite ages of the giant Morro Velho and Cuiabá gold deposits, Rio das Velhas greenstone belt, Quadrilátero Ferrífero, Minas Gerais, Brazil. Ore Geol Rev 32:674–680

Lobato LM, Renger FE, Silva RCF, Rosière CA, Baars FJ, Rolim VK (2014) Metalogênese do setor meridional do Cráton São Francisco. In: Silva MG, MBR N, Jost H, Kuyumjian RM (eds) Metalogênese das Províncias Tectônicas Brasileiras. Companhia de Pesquisas de Recursos Minerais, Brasília, Brazil, Belo Horizonte, pp 119–140

Lüders V, Romer RL, Cabral AR, Schmidt C, Banks DA, Schneider J (2005) Genesis of itabirite-hosted au-Pd-Pt-bearing hematite-(quartz) veins, Quadrilátero Ferrífero, Minas Gerais, Brazil: constraints from fluid inclusion infrared microthermometry, bulk crush-leach analysis and U-Pb systematics. Mineral Deposita 40: 289–306

Machado N, Schrank A, Abreu FD, Knauer LG, Almeida-Abreu PA (1989) Resultados preliminares da geocronologia U-Pb na Serra do Espinhaço Meridional. Boletim do Núcleo Minas Gerais-SBG 10:171–174

Marsala A, Wagner T, Wälle M (2013) Late-metamorphic veins record deep ingression of meteoric water: a LA-ICPMS fluid inclusion study from the fold-and-thrust belt of the Rhenish Massif, Germany. Chem Geol 351:134–153

Martins BS, Lobato LM, Rosière CA, Hagemann SG, Santos JOS, Villanova FLDSP, Silva RCF, Ávila Lemos LH (2016) The Archean BIF-hosted Lamego gold deposit, Rio das Velhas greenstone belt, Quadrilátero Ferrífero: evidence for Cambrian structural modification of an Archean orogenic gold deposit. Ore Geol Rev 72: 963–988

McCuaig TC, Kerrich R (1998) P-T-t-deformation and fluid characteristics of lode gold deposits: evidence from alteration systematics. Ore Geol Rev 12:381–453

Mernagh TP, Bastrakov EN, Zaw K, Wygralak AS, Wyborn LAI (2007) Comparison of fluid inclusion data and mineralization processes for Australian orogenic gold and intrusion-related gold systems. Acta Petrol Sin 23:21–32

Morales MJ, Silva RCF, Lobato LM, Gomes SD, Gomes CC, Banks DA (2016) Metal source and fluid-rock interaction in the Archean BIF-hosted Lamego gold mineralization: microthermometric and LA-ICP-MS analyses of fluid inclusions in quartz veins, Rio das Velhas greenstone belt, Brazil. Ore Geol Rev 72:510–531

Moreira H, Lana C, Nalini HA (2016) The detrital zircon record of an Archean convergent basin in the southern São Francisco Craton, Brazil. Precambrian Res 275:84–99

Muramatsu Y, Wedepohl KH (1998) The distribution of iodine in the earth's crust. Chem Geol 147:201–216

Noce CM (2013) Geochronology of the Quadrilátero Ferrífero: a review. Rev Geonomos 8:15–23

Noce CM, Zuccheti M, Baltazar O, Armstrong R, Dantas E, Renger FE, Lobato LM (2005) Age of felsic volcanism and the role of ancient continental crust in the evolution of the Neoarchean Rio das Velhas Greenstone belt (Quadrilátero Ferrífero, Brazil): U-Pb zircon dating of volcaniclastic greywackes. Precambrian Res 141:67–82

Noce CM, Tassinari CC, Lobato LM (2007) Geochronological framework of the Quadrilátero Ferrífero, with emphasis on the age of gold mineralization hosted in Archean greenstone belts. Ore Geol Rev 32:500–510

Oliver NH, Thomson B, Freitas-Silva FH, Holcombe RJ, Rusk B, Almeida BS, Faure K, Davidson GR, Esper EL, Guimarães PJ, Dardenne MA (2015) Local and regional mass transfer during thrusting, veining, and boudinage in the genesis of the giant shale-hosted Paracatu gold deposit, Minas Gerais, Brazil. Econ Geol 110: 1803–1834

Passchier C (2001) Flanking structures. J Struct Geol 23:951–962

Phillips GN, Powell R (2010) Formation of gold deposits: a metamorphic devolatilization model. J Metamorph Geol 28:689–718

Pitcairn IK, Teagle DAH, Craw D, Olivo GR, Kerrich R, Brewer TS (2006) Sources of metals and fluids in orogenic gold deposits: insights from the Otago and Alpine Schists, New Zealand. Econ Geol 101:1525–1546

Potter RW (1977) Pressure corrections for fluid-inclusion homogenization temperatures based on the volumetric properties of the system NaCl-H2O. J Res U S Geol Surv 5:503–607

Ramboz C, Pichavant M, Weisbrod A (1982) Fluid immiscibility in natural processes: use and misuse of fluid inclusion data: II. Interpretation of fluid inclusion data in terms of immiscibility. Chem Geol 37:29–48

Rauchenstein-Martinek K, Wagner T, Wälle M, Heinrich CA (2014) Gold concentrations in metamorphic fluids: a LA-ICPMS study of fluid inclusions from the Alpine orogenic belt. Chem Geol 385:70–83

Rauchenstein-Martinek K, Wagner T, Wälle M, Heinrich CA, Arlt T (2016) Chemical evolution of metamorphic fluids in the Central Alps, Switzerland: insight from LA-ICP-MS analysis of fluid inclusions. Geofluids 16:877–908

Ribeiro Y, Silva RCF, Lobato LM, Lima LC, Rios FJ, Hagemann SG, Cliff J (2015) Fluid inclusion and sulfur and oxygen isotope studies on quartz-carbonate-sulfide veins of the Carvoaria Velha deposit, Córrego do Sítio gold lineament, Quadrilátero Ferrífero, Minas Gerais, Brazil. Ore Geol Rev 67:11–33

Ribeiro-Rodrigues LC(1998) Gold mineralization in Archean banded iron-formation of the QF, Minas Gerais, Brazil-The Cuiabá Mine. Dissertation, RTWH Aachen

Ribeiro-Rodrigues LC, de Oliveira CG, Friedrich G (2007) The Archean BIF-hosted Cuiabá Gold deposit, Quadrilátero Ferrífero, Minas Gerais, Brazil. Ore Geol Rev 32:543–570

Ridley JR, Diamond LW (2000) Fluid chemistry of orogenic lode gold deposits and implications for genetic models. Rev Econ Geol 13:141–162

Robert F, Poulsen KH (2001) Vein formationand deformation in greenstone gold deposits, in Richards JP, Tosdal RM, Structural Controls on Ore Genesis: Society of Economic Geologists, Rev Econ Geol 14:111–155

Roedder E (1984) Fluid inclusions: Washington. DC, MSA. Rev Mineral 12:644

Schindler C, Hagemann SG, Banks D, Mernagh T, Harris AC (2016) Magmatic hydrothermal fluids at the sedimentary rock-hosted, intrusion-related Telfer gold-copper deposit, Paterson Orogen, Western Australia: pressure-temperature-composition constraints on the ore-forming fluids. Econ Geol 111:1099–1126

Schrank A, Machado N (1996) Idades U-Pb em monazitas e zircões das minas de Morro Velho e Passagem de Mariana-Quadrilátero Ferrífero (MG). In SBG Congresso Brasileiro de Geologia 39:470–472

Seo JH, Guillong M, Heinrich CA (2012) Separation of molybdenum and copper in porphyry deposits: the roles of sulfur, redox, and pH in ore mineral deposition at Bingham Canyon. Econ Geol 107:333–356

Spear FS (1995) Metamorphic phase equilibria and pressure-temperature-time paths, Washington. MinSoc Am, pp 799

Sterner SM, Bodnar RJ (1984) Synthetic fluid inclusions in natural quartz I. Compositional types synthesised and applications to experimental geochemistry. Geochim Cosmochim Acta 48:2659–2668

Taylor BE (1987) Stable isotope geochemistry of ore-forming fluids. Min Assoc Can, Short Course Handbook 13:337–445

Taylor SR, McLennan SM (1985) The continental crust: its composition and evolution. Blackwell Scientific Publications, pp 312

Toledo C (1997) Controle estrutural da mineralização aurifera na mina de Cuiabá, setor noroeste do Greenstone Belt Rio das Velhas, Quadrilátero Ferrífero. Dissertation, Universidade Estadual de Campinas

Vial D (1980) Mapeamento Geologico do Nivel3 da mina de Cuiabá, Mineração Morro Velho. Internal Report

Vieira FWR (1988) Processos epigenéticos da formação dos depósitos auríferos e zonas de alteração hidrotermal do Grupo Nova Lima, Quadrilátero Ferrífero, Minas Gerais. SBG Congresso Brasileiro da Geologia, Belém 1:76–86

Vieira FWR (1991) Texturesand processes ofhydrothermalalterationandmineralization in the Nova Lima Group, Minas Gerais, Brazil. Brazil Gold 91:319–327

Vitorino LA (2017) Mineralização aurífera associada aos veios quartzo-carbonáticos hospedados na unidade máfica basal da jazida Cuiabá, Greenstone belt Rio das Velhas, Minas Gerais, Brasil. Dissertation, Universidade Federal de Minas Gerais

Wagner T, Fusswinkel T, Wälle M, Heinrich CA (2016) Microanalysis of fluid inclusions in crustal hydrothermal systems using laser ablation methods. Elements 12:323–328

Wilkinson JJ (2001) Fluid inclusions in hydrothermal ore deposits. Lithos 55:229–272

Wilkinson JJ, Stoffell B, Wilkinson CC, Jeffries TE, Appold MS (2009) Anomalously metal-rich fluids form hydrothermal ore deposits. Science 323:764–767

Xavier RP, Toledo CLB, Taylor B, Schrank A (2000) Fluid evolution and gold deposition at the Cuiabá mine, SE Brazil: fluid inclusions and stable isotope geochemistry of carbonates. Rev Bras Geogr 30:337–341

Yardley BWD (2005) Metal concentrations in crustal fluids and their relationship to ore formation, 100th anniversary special paper. Econ Geol 100:613–632

Yardley BWD, Bodnar RJ (2014) Fluids in the continental crust. Geochem Perspect 3:1–127
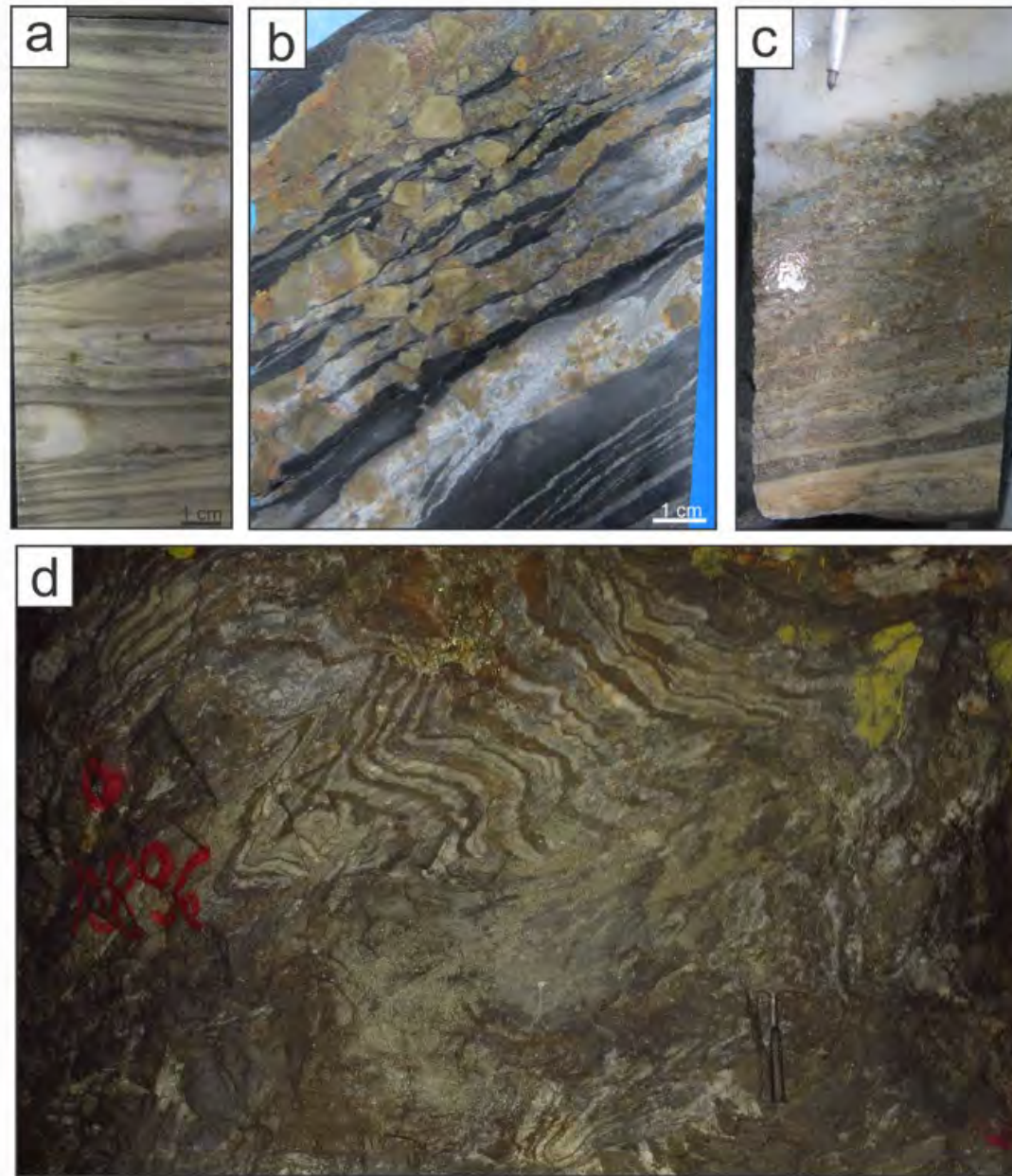
Photographs of mineralised host rocks at Cuiabá. **a** Sampled drill core section of sulfidised andesite (Level 17 of the Fonte Grande Sul ore body, drill core 03A, 1414.70–1414.84). **b** Sampled drill core section of sulfidised carbonaceous pelite (Level 17 of the Fonte Grande Sul ore body, drill core 009, 1378.24–1378.40). **c** Sampled drill core section of sulfidised BIF ((Level 17 of the Fonte Grande Sul ore body, drill core 03A, 1619.6–1619.85). **d** Stope view of sulfidised BIF (Level 15, Galinheiro ore body) (PNG 1737 kb)
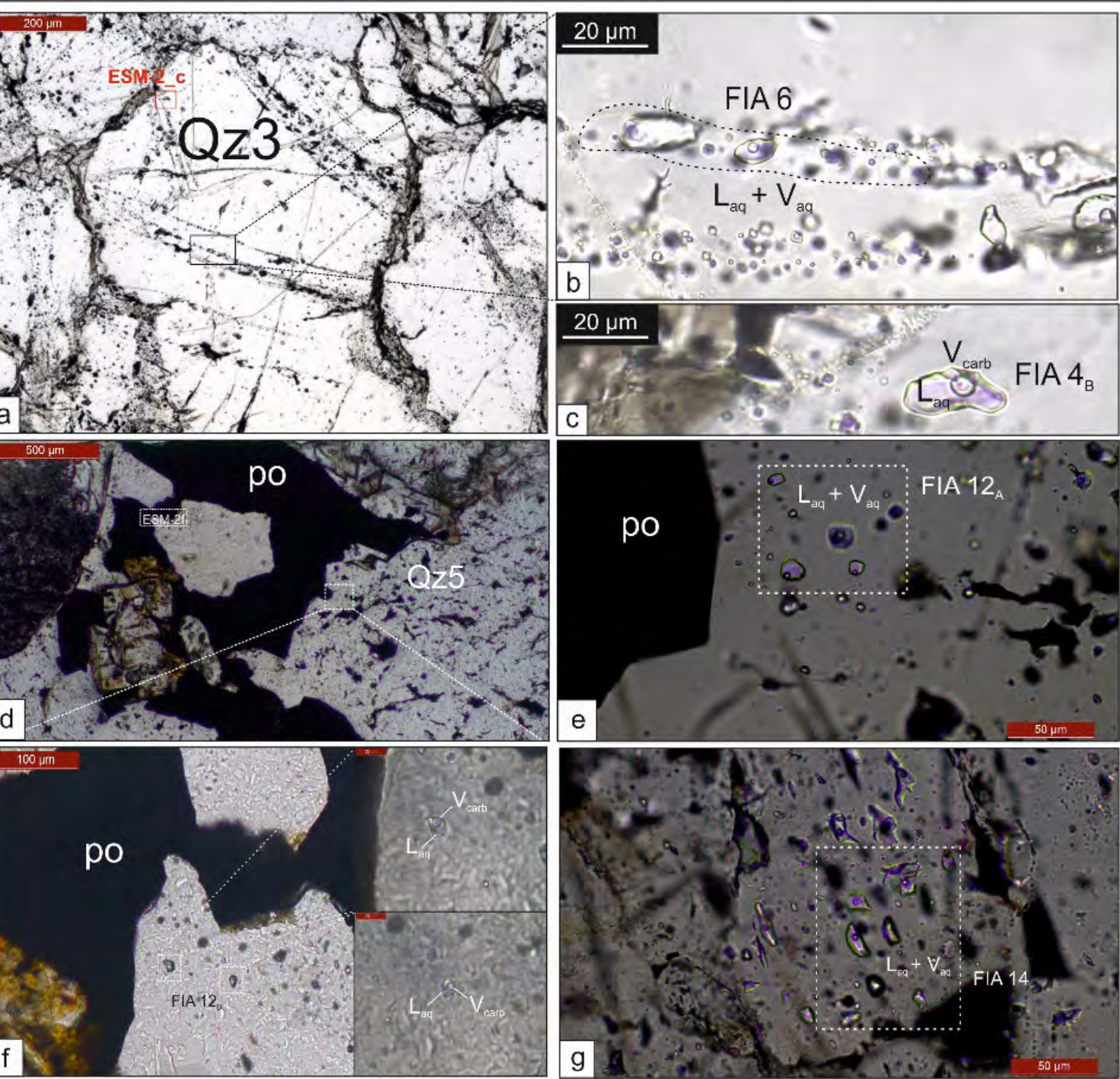
Examples of Representative FIAs of V3 and V4 vein types of the Veio de Quartzo ore body.

a-c Qz3-V3 extensional vein arrays displaying an internal trail of two-phase, aqueous fluid inclusions (FIA 6) and two-phase, isolated aqueous-carbonic fluid inclusion (FIA 4_B).

d-g Qz5-V4 late-stage veins, showing two phase, grouped, aqueous fluid inclusions (FIA 12_A), individual aqueous-carbonic fluid inclusions (FIA 12_B) and two phase, grouped, aqueous fluid inclusions (FIA 14). Photo-micrographs taken under transmitted light (JPG 18573 kb)
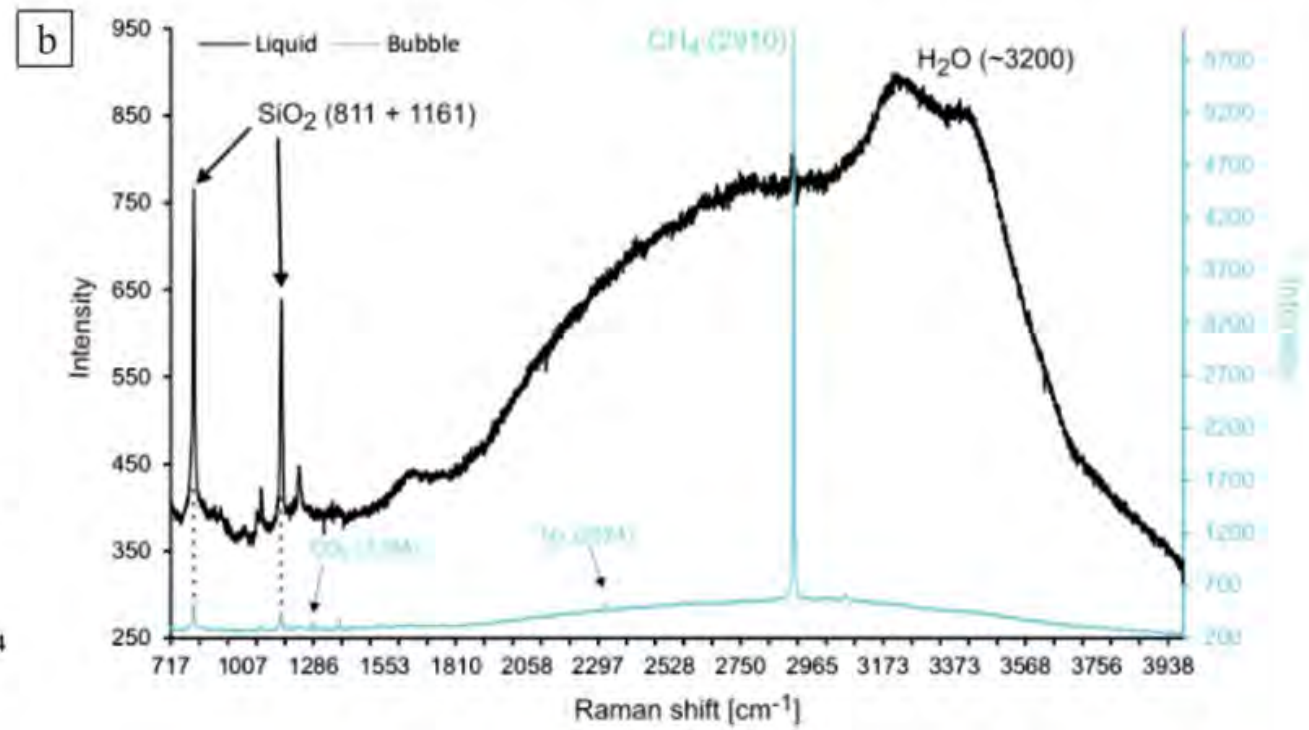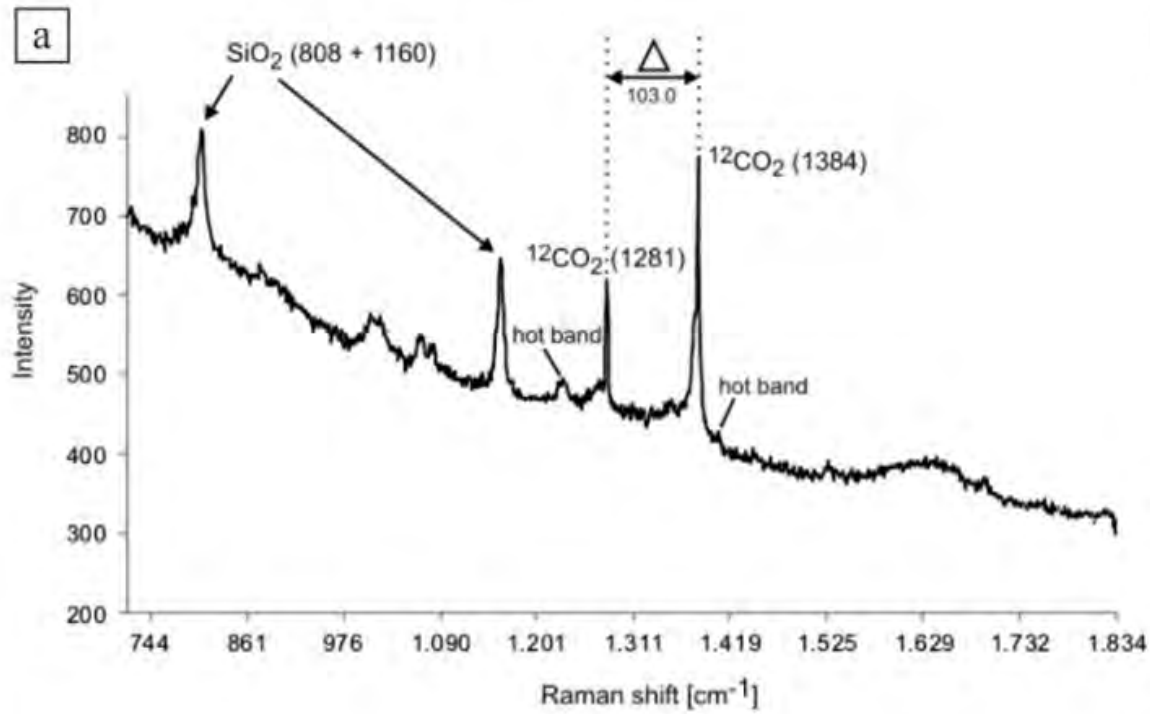
Raman spectra of individual fluid inclusions. a Raman spectra of FIAs trapped in Qz1-V1 shear veins. b Raman spectra of FIAs trapped in Qz3-V3 extensional vein arrays (PNG 204 kb)

ESM_4: Arsenic and gold composition (in ppm) of aqueous fluid inclusions trapped in quartz of V1 shear, V2 extensional and V4 late-stage veins measured by laser ablation-inductively coupled plasma-mass spectroscopy (DOCX 14 kb)

Sample ID	Vein type	Quartz type	FIA		Na [wt %]	K [wt %]	Fe [wt %]	As [ppm]	Au [ppm]
009_7	V1	Qz1	8_D (n=4)	Min	1.93	0.11	0.02	17	1
				Max	3.69	1,74	0.16	398	39
				Mean	2.64	1.01	0.10	134	14
				Median	2.60	1.05	0.11	64	12
007_2	V2	Qz2	11_D (n=6)	Min	0.61	0.84	0.26	78	1
				Max	1.16	1.96	0.95	329	14
				Mean	0.83	1.55	0.63	174	7
				Median	0.78	1.67	0.69	125	7
QZL_1	V4	Qz5	13 (n=4)	Min	2.42	0.15	0.06	34	7
				Max	3.88	0.86	1.04	419	56
				Mean	3.14	0.53	0.43	221	25
				Median	3.32	0.60	0.38	290	29

ESM_5:

Average laser ablation-inductively coupled plasma-mass spectroscopy concentration data (in ppm) for aqueous and aqueous-carbonic FIAs trapped in quartz (Qz1, Qz2, Qz3 and Qz5) of the andesite hosted shear and extensional quartz veins, Veio de Quartzo ore body (DOCX 30 kb)

Vein type	Sample ID	Quartz type	FIA	N	FI type	Salinity [wt % NaCl equiv]	Na	Mg	K	Ca	Mn	Fe	Cu	Zn	Sr	Ag	Ba	Pb
V1 shear veins	009_7 2a	Qz1			$L_{aq}+V_{carb}$		16100	5480	8440	535	34	670	669	-	75	17	25	173
	009_7 2b	Qz1	8_C	4	$L_{aq}+V_{carb}$	9.3	16600	4260	7980	4620	54	482	1630	746	88	10	19	261
	009_7 2c	Qz1			$L_{aq}+V_{carb}$		19500	4920	6900	2940	-	314	1060	637	178	30	16	208
	009_7 2d	Qz1			$L_{aq}+V_{carb}$		18400	2640	7590	5720	111	788	644	427	168	34	38	166
	009_7 3b	Qz1	8_B	3	$L_{aq}+V_{aq}$	5.4	9800	1630	4300	3520	34	590	294	793	60	8	24	154
	009_7 3c	Qz1			$L_{aq}+V_{aq}$		9130	1080	6340	2660	33	762	451	472	91	15	28	147
	009_7 3e	Qz1	8_A	3	$L_{aq}+V_{aq}$	2.7	4250	900	3020	1440	61	218	312	292	11	9	11	62
V2 extensional veins	007_2 1a	Qz2	9	4	$L_{aq}+V_{aq}$	5.0 to 8.5	13200	11300	-	-	334	-	-	-	508	-	226	-
	007_2 1	Qz2	11_A	5	$L_{aq}+V_{aq}$	4.5 to 6.6	13800	7500	3730	-	140	-	-	-	345	-	209	-
	007_2 1b	Qz2	11_B	2	$L_{aq}+V_{aq}$		10200	3900	4240	7060	194	-	-	-	143	-	79	-
	007_2 3a	Qz2	11_C	4	$L_{aq}+V_{aq}$	4.8 to 8.0	10400	4670	3940	5470	74	210	382	-	199	-	122	403
	007_2 3b	Qz2	11_D	6	$L_{aq}+V_{aq}$	6.6	7800	5230	6970	4810	124	-	621	-	58	10	73	348
	007_2 3c	Qz2	11_E	5	$L_{aq}+V_{aq}$		10600	4890	4890	4740	181	-	-	-	63	18	60	575
V3 extensional vein array	FICU1 4a	Qz3	4_A	3	$L_{aq}+V_{aq}$	6.6	10400	3480	4040	5700	190	731	642	1630	40	64	45	361
	FICU1 4b	Qz3	4_C	4	$L_{aq}+V_{carb}$	9.2	19000	2300	7060	3890	103	1330	1100	-	67	31	47	1120
	FICU1 4c	Qz3	4_D	3	$L_{aq}+V_{carb}$	6.5 to 10.1	9260	2490	4880	8060	116	277	350	1450	69	38	34	323
	FICU1 3a	Qz3	5_A	3	$L_{aq}+V_{aq}$	3.0 to 3.6	5400	650	3030	1270	28	385	256	463	17	12	11	287
	FICU1 3b	Qz3			$L_{aq}+V_{aq}$		5230	667	3640	1050	33	526	281	-	13	12	9	347
	FICU1 3c	Qz3	5_B	3	$L_{aq}+V_{aq}$	9.2	16300	2660	8110	5840	107	1130	948	-	40	27	46	829
	FICU1 4d	Qz2	3	7	$L_{aq}+V_{aq}$	5.5 to 8.5	8420	2780	6300	3860	204	-	534	-	6	-	7	-
	FICU1 4e	Qz2			$L_{aq}+V_{aq}$		9630	3230	4410	3720	90	599	414	-	218	7	48	286
	FICU1 2a	Qz2	2_A	2	$L_{aq}+V_{aq}$	4.9	8470	1420	4700	4050	39	280	355	36	81	25	62	2
	FICU1 2b	Qz2	2_B	4	$L_{aq}+V_{aq}$	6.2	8710	1620	3670	3820	75	464	599	-	148	14	73	318
	FICU1 2c	Qz2	2_C	4	$L_{aq}+V_{aq}$	5.0	9500	1330	3180	3970	179	-	673	-	98	-	85	496
	FICU1 1a	Qz2	2_D	2	$L_{aq}+V_{aq}$	6.1	8520	2290	4660	2380	327	55	488	350	179	-	107	153
	FICU1 1b	Qz2	2_E	4	$L_{aq}+V_{aq}$	6.1	8180	1610	4840	3210	211	-	339	608	243	39	78	154
	FICU1 1c	Qz2	2_F	4	$L_{aq}+V_{aq}$	4.9 to 5.7	9760	2730	3190	1870	109	670	228	581	140	-	41	188
	FICU1 1d	Qz2	2_{G1}	3	$L_{aq}+V_{aq}$	6.1	11800	2730	3920	3220	232	686	646	142	228	34	76	312
	FICU1 1e	Qz2	2_{G2}	4	$L_{aq}+V_{aq}$		10600	2410	4920	4710	335	286	-	235	191	32	64	185
	FICU1 1	Qz1	1	4	$L_{aq}+V_{aq}$	11.8	21500	9400	6310	5930	387	-	1020	588	456	49	327	314
	FICU1 1f	Qz1		3			20600	6040	10800	6570	526	-	441	851	259	31	249	192
V4 late-stage veins	QZL 1a	Qz5	12_A	5	$L_{aq}+V_{aq}$	6.2	15900	1390	3550	2540	113	112	280	173	150	21	36	298
	QZL 1b	Qz5	14	8	$L_{aq}+V_{aq}$	6.2	16800	1540	3260	1740	63	106	286	375	169	19	40	152
	QZL_2a	Qz5	16_B	5	$L_{aq}+V_{aq}$	8.2	19100	1790	4310	3950	139	348	503	714	295	24	115	209
	QZL 3a	Qz5		2	$L_{aq}+V_{aq}$		25800	1910	1670	1000	17	232	-	242	342	9	93	68
	QZL 3b	Qz5	18	3	$L_{aq}+V_{aq}$	6.4 to 9.6	17700	1650	3790	6450	153	-	112	865	150	22	52	483
	QZL_3c	Qz5		3	$L_{aq}+V_{aq}$		19700	329	6720	2750	243	618	-	573	105	25	66	302
	QZL 3d	Qz5		2	$L_{aq}+V_{aq}$		21000	1090	2940	4890	118	285	452	242	191	12	38	142
	QZL 3	Qz5	19		$L_{aq}+V_{aq}$	2.5 to 3.6	5500	698	2090	1750	64	733	434	977	83	9	41	163
	QZL_3f	Qz5		2	$L_{aq}+V_{aq}$		5140	645	2670	2080	83	852	545	190	78	22	30	214

Chapter 3

Publication in Ore Geology Review:

"Sulfur isotope and metal variations in sulfides in the BIF-hosted orogenic Cuiabá gold deposit, Brazil: implications for the hydrothermal fluid evolution"

Sulfur isotope and metal variations in sulfides in the BIF-hosted orogenic Cuiabá gold deposit, Brazil: Implications for the hydrothermal fluid evolution

Carolin Kresse[a],[*], Lydia M. Lobato[a], Steffen G. Hagemann[b], Rosaline C. Figueiredo e Silva[a]

[a] Institute of Geosciences, Federal University of Minas Gerais, Belo Horizonte, Brazil
[b] Centre for Exploration Targeting, School of Earth and Environmental Sciences, University of Western Australia, Perth, Australia

ABSTRACT

Textural, chemical and multiple sulfur isotope analyses of sulfides from the Archean world-class Cuiabá orogenic Au deposit, Quadrilátero Ferrífero district, Brazil, were conducted to track distinct trace element signatures from syngenetic to epigenetic-hydrothermal pyrite types in different host units, and to deduce the nature and source of the mineralizing fluids. Gold mineralization in Cuiabá is hosted in greenschist facies volcanic and sedimentary host rocks belonging to the Archean Rio das Velhas Supergroup, especially in association with quartz veins and sulfide minerals. The BIF-hosted Fonte Grande Sul orebody is controlled by quartz veins and disseminated gold-bearing pyrite, pyrrhotite and arsenopyrite in the wall rocks. Five pyrite types are classified based on textural relations as spongy, syngenetic (Py1), porous early-(Py2), smooth main-(Py3) and smooth isolated and over-grown late-stage (Py4 and Py5) types variably present in metamorphosed carbonaceous pelites, BIF and andesite. Besides pyrite, pyrrhotite and arsenopyrite are also defined according to textural and paragenetic differences, and they display significant trace element contents. Trace element abundance maps and LA-ICP-MS analyses display trace element incorporations in Py1 (present only in carbonaceous pelite), Py2 and Py3 (in all host rocks), and Py4 and Py5 (only in BIF). Py1 yields high As, Co, Ni, Pb and Ag concentrations, whereas Py2 (formed by agglomeration of Py1) maintains high trace element concentrations with slightly less of those elements. Trace element incorporation in Py3 is similar to Py1 in carbonaceous pelite. Early-stage Py2 and main-stage Py3 in BIF and andesite have increased Co and Ni, but have less Au and As. Late-stage Py4 is characterized by lower trace element concentrations, whereas Py5 is further enriched in As, Bi, Co, Ni and Pb. The hydro-thermal alteration is divided into early-, main- and late-stage, which correlate to the sulfide hydrothermal evolution. The study shows that carbonaceous pelite is pre-enriched in Co, Ni and Pb, whereas certain elements like Ag, Au, Bi and As are only hydrothermally concentrated either during the early, main or late stage in BIF and andesite. This geochemical pattern supports a syngenetic versus hydrothermal origin of distinct elements, in-cluding some trace elements now in the ore zones. Multiple sulfur isotope data suggest that mineralizing fluids at the Cuiabá gold deposit reflect a complex mixing of sulfur evolved from three possible sources: seawater, mantle, and reduced elemental sulfur. Spongy, syngenetic Py1 yields $\Delta^{33}S$ values ranging from -2.28 to $-0.25‰$, separated into two ranges, the first from -2.28 to $-1.97‰$, and the second from -0.96 to $-0.25‰$. The first range suggests Py1 in the carbonaceous pelite was deposited in a seawater environment. These pyrites probably mixed with later mantle sulfur carrying a near-zero $\Delta^{33}S$ signature, which is indicated by the second $\Delta^{33}S$ range, or could have mixed with fluids sourced from sedimentary rocks at depth carrying a positive $\Delta^{33}S$ signature. The second scenario is more common in sedimentary and diagenetic pyrites. An unequivocal contrast is shown by early-, main- and late-stage pyrite types (Py2, Py3, Py4 and Py5) in carbonaceous pelite, BIF and andesite, which present a continuous process of crustal assimilation values towards increasingly positive $\delta^{34}S$ and $\Delta^{33}S$ values. This confirms evidence for a sedimentary-derived sulfur source as also indicated by fluid inclusion data of the andesite-hosted orebody at the Cuiabá deposit.
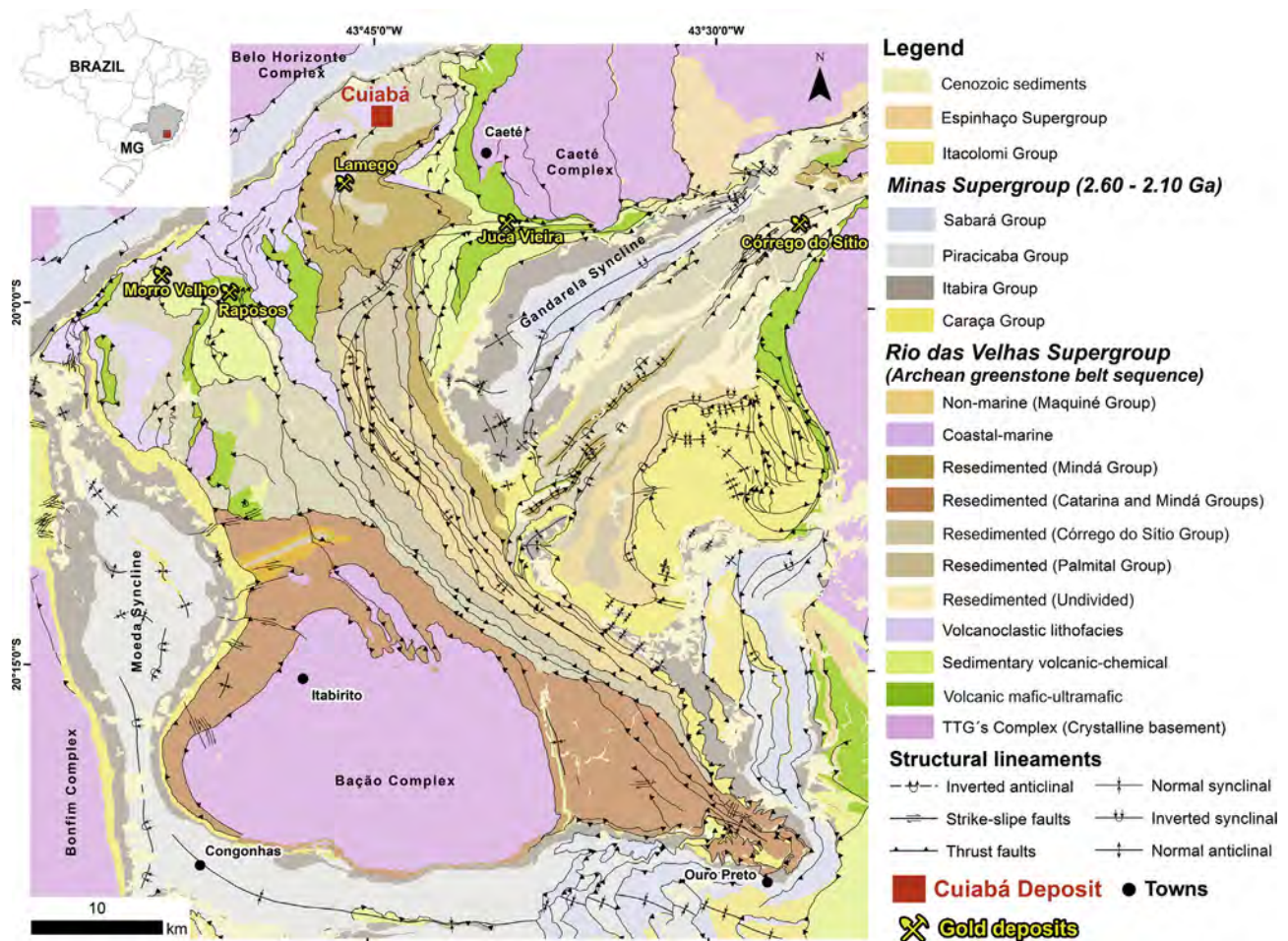
Fig. 1. Geological map of the Quadrilátero Ferrífero region with principal lithofacies associations of the Rio das Velhas greenstone belt after Baltazar and Zucchetti (2007), and location of the Cuiabá and other gold deposits (after compilation by Lobato et al., 2005).

1. Introduction

The BIF-hosted Cuiabá orogenic Au deposit is located in the northern part of the Quadrilátero Ferrífero district (QF; Fig. 1), one of the most significant Au provinces in Brazil (Lobato et al., 2014). The Cuiabá gold deposit, operated by AngloGold Ashanti Brasil Mineração Ltda.-AGA, is located approximately 40 km northeast of Belo Horizonte, in the northern part of the QF, in the State of Minas Gerais, SE Brazil (Fig. 1). It is the largest underground gold mine in the country, containing 150 t Au. As of 2015, it has produced five million ounces (Moz), with a further 7 Moz in reserve (AGA, personal communication), making it the largest gold deposit in the QF. According to AGA, the deposit produces 1.2 million tonnes of ore per year, with an average grade of 7.96 g/t Au, and by-product Ag and H_2SO_4. The cut-off grade is 2.82 g/t Au, with reserves at 9.8 million tonnes ore and total resources (inferred, indicated and measured) of 21.7 million tonnes ore (in December 2008). Between 1985 and 2008, gold production amounted to 103 tonnes of this metal. Its expected life is until 2026 (date 2010 AGA, personal communication). Gold has been reported and mined from numerous localities in the QF, mainly in the northern and southeastern parts, which are hosted by Archean and Paleoproterozoic successions. The largest gold deposits, e.g., Morro Velho, Cuiabá, Lamego, Raposos, São Bento, are hosted in the basal unit of the Nova Lima Group. The world-class Morro Velho Mine started production in 1834, and has produced > 470 t of gold from 1834 to 1999. Raposos and São Bento were also closed in recent years. The major mines operating by Anglogold Ashanti are Cuiabá, Lamego and those of the Córrego do Sítio lineament that are located in the northeastern part of the QF.

The Cuiabá deposit is hosted by a sequence of metamorphosed volcanic and sedimentary rocks, with mineral assemblages typical of the greenschist facies metamorphic conditions. The local rock stratigraphy encompasses, from bottom to top, a lower metamafic unit, BIF and metachert (carbonaceous and-or ferruginous), carbonaceous phyllite, an upper metamafic unit, micaceous phyllite and metavolcanoclastic rocks. Gold is associated with massive and disseminated sulfide minerals, mainly pyrite and pyrrhotite, hosted in BIF and metachert, especially in the Fonte Grande Sul, Serrotinho, Balancão and Galinheiros orebodies, with the Cuiabá fold marking the contours of the BIF (Fig. 2, Ribeiro Rodrigues et al., 2007). However, a small amount of gold associated with quartz-carbonate veins hosted in the upper metamafic unit have also been mined in the Viana, Galinheiro Footwall and Galinheiro Quartzo orebodies (Fig. 2; Ribeiro Rodrigues, 1998).

The predominant sulfide minerals - pyrite, pyrrhotite and arsenopyrite - reflect diagenetic and epigenetic-hydrothermal stages based on cross-cutting and replacements patterns, as well as textural and zonation features. Based on these observations and the classification into different stages, additional geochemical variations provide a link to the hydrothermal evolution at Cuiabá. Equivalent sulfide phase classification, especially for pyrite, by Large et al. (2007, 2009), and Martins et al. (2016), verify a relation between geochemical and textural associated pyrite stages, as pyrite trace element composition is related to fluid composition (Tardani et al., 2017). To resolve the controversial source of mineralizing fluids (Groves et al., 2003; Large et al., 2011; Tomkins, 2013), many studies on the characterization and quantification of trace elements in sulfide minerals associated with orogenic Au deposits have been conducted (Pitcairn et al. 2006; Wood and Large,
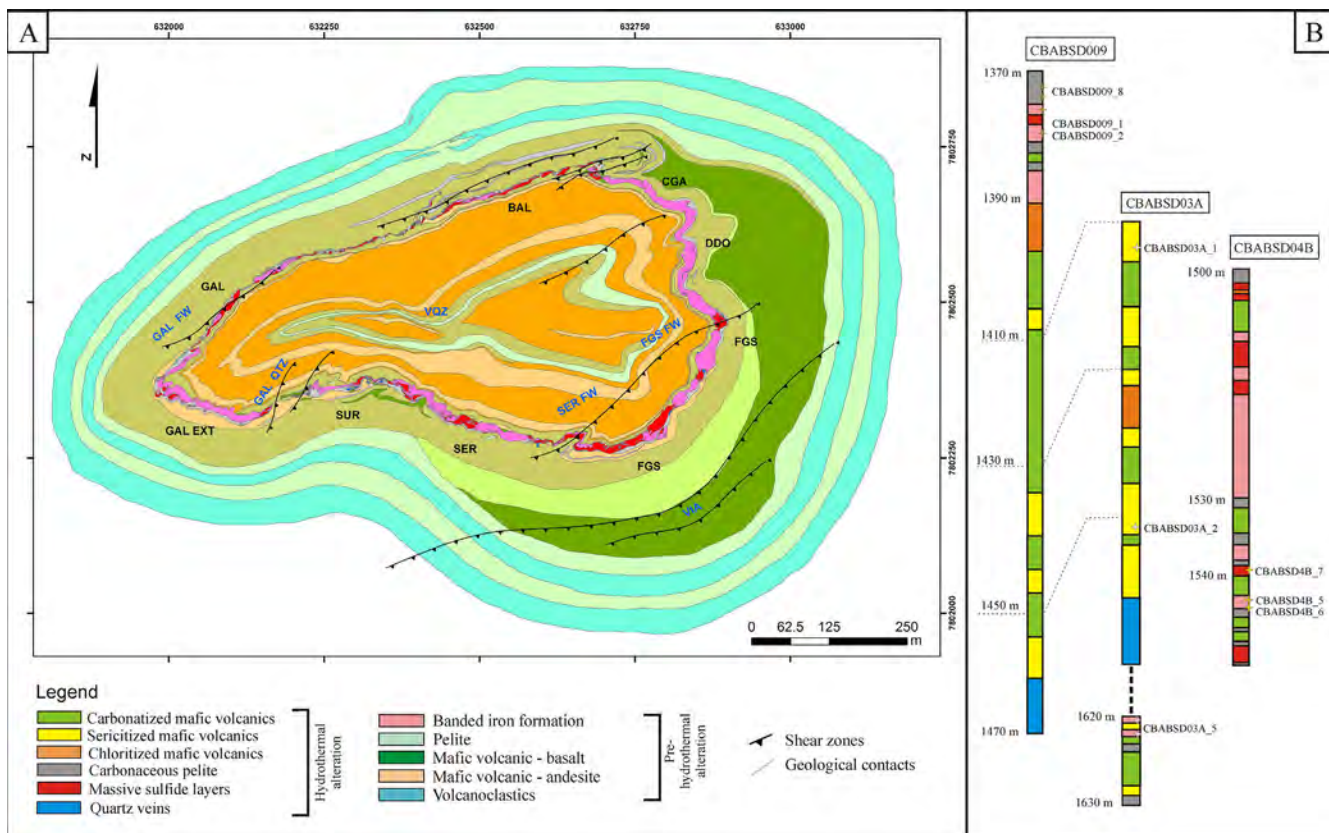
Fig. 2. Geological map of the Cuiabá mine, Level 11 and location of all main orebodies **(A)** (modified after Vitorino, 2017). Orebodies BAL = Balancão; CTG = Canta Galo; FG = Fonte Grande; FGS = Fonte Grande Sul; SER = Serrotinho; SUR = Surucu; GAL = Galinheiro; DDO = Dom Domingos; GAL FW = Galinheiro Footwall; GAL QTZ = Galinheiro Quartzo; GAL EXT = Galinheiro Extenção; SER FW = Serrotinho Footwall; FGS FW = Fonte Grande Sul Footwall; VQZ = Veio de Quartzo; VIA = Viana. Schematic lithostratigraphic succession of sampled drill cores sections CBABSD009, CBABSD03A and CBABSD04B **(B)**. Sections are representative of the FGS orebody.

2007; Morey et al., 2008; Sung et al., 2009; Thomas et al., 2011; Large et al. 2011, 2012; Velásquez et al., 2014; Finch and Tomkins, 2017; Selvaraja et al., 2017a,b,c). Laser ablation inductively coupled plasma mass spectrometry (LA-ICP-MS) and sulfur isotope analyses of pyrite and pyrrhotite by Large et al. (2007), Gregory et al. (2015a,b, 2016), Steadman et al. (2015), Steadman and Large (2016) and Neyedley et al. (2017) have shown significant differences in trace element compositions and/or sulfur isotope signatures, indicating the relation between hydrothermal fluid composition and trace element content in sulfide minerals. Furthermore, trace element signatures of sulfides can also be used to distinguish between different sulfide generations, revealing a complex multiphase hydrothermal history (Zhao et al., 2011). Previous research on orogenic Au deposits by Groves et al. (2000) and Hagemann and Cassidy (2000) argued that Au was introduced from a deeply sourced fluid late in the deformation history of the deposit (syn- or post-kinematic). For Carlin-style and orogenic Au deposits in sedimentary environments, Large et al. (2009) proposed that invisible gold is concentrated early in pyrite during the growth of diagenetic pyrite, and may be remobilized and reconcentrated late in the outer growth zones of hydrothermal pyrite due to final deformation stages. Similar findings are indicated by Oliver et al. (2015) for the world-class Neoproterozoic Paracatu orogenic Au deposit, Brazil.

In addition to trace elements, sulfur isotope data are also informative, since they help trace the potential sulfur source, as each reservoir has characteristic isotopic compositions. Fundamental processes such as mixing and interaction with the mantle, crustal magmas, hydrothermal fluids, and country rocks control isotopic signatures, and result in sulfides with variable sulfur isotope compositions (Xue et al., 2013; LaFlamme et al., 2016, 2018; Gregory et al., 2016; Selvaraja

et al., 2017a). Secondary ion mass spectrometry (SIMS) offers high-precision isotopic analysis of multiple sulfur isotopes, and affords the ability to measure the least common stable isotopes of sulfur, ^{33}S (0.75%) and ^{36}S (0.02%), together with the more abundant ^{32}S (95.02%) and ^{34}S (4.21%) isotopes, while preserving spatial context. This provides the potential to identify the anomalous sulfur isotopic signatures indicative of mass-independent (MIF) or mass-dependent fractionation (MDF) (Farquhar et al., 2013; Whitehouse, 2013; Ireland et al., 2014; Ushikubo et al., 2014).

Previous data on different pyrite types at Cuiabá were presented by Ribeiro Rodrigues (1998), Martins (2000), Costa (2000), and Lobato et al. (2001b,c). These studies are based on textural features, and pyrites are generally classified as: i) fine-grained, ii) coarse-grained with poikiloblastic centres and massive rims, and iii) medium- to coarse-grained and porphyroblastic. These authors noted that all three types may locally have low chemical variations characterized by As-rich and -poor fractions. Existing sulfur isotope studies at the Cuiabá deposit by Lobato et al. (2001c) and Bühn et al. (2012) focused on the pyrite-mineralized BIF, resulting in a range of $\delta^{34}S$ = +3.8–5.1‰. The $\delta^{33}S$ = 2.9–4.8‰ and $\Delta^{33}S$ = 0.9–2.2‰ by Bühn et al. (2012) clearly suggest sulfur isotope MIF.

In this contribution, we present a new systematic geochemical and sulfur isotope characterization of syngenetic and epigenetic sulfide mineral generations of the Cuiabá deposit. The classification of pyrite, pyrrhotite and arsenopyrite types is based on textural variations and defined paragenetic stages. We suggest that the various pyrite stages document the isotopic and geochemical evolution of the mineralizing fluid. Data obtained by electron probe micro analyzer (EPMA) and LA-ICP-MS illustrate element incorporation in the pyrite varieties hosted in

metamorphosed carbonaceous pelite, BIF and mafic volcanic rocks. Our aim is to understand the traceability of the mineralization history from textures and sulfide trace element content and sulfur isotope signatures in the different host rocks. Pyrrhotite and arsenopyrite data serve as indicators to constrain the consistency of element distribution throughout the sulfide minerals. In general, multiple sulfur isotope analyses (^{32}S, ^{33}S, ^{34}S, ^{36}S) of pyrite and pyrrhotite related to gold mineralization confine the origin of sulfur to felsic magmas, mantle-sourced, metamorphic or meteoric fluids, as well as sedimentary source. As the transport of Au in hydrothermal fluids is generally assumed to be complexed with HS⁻ in orogenic gold systems (Groves et al., 1998; Large et al., 2011), tracing the sulfur source may place strong constraints on the origin of Au.

2. Regional geology

The QF district covers an area of 7000 km2, centered about latitude 20° 15′ S and longitude 43° O 30′ W in the south-central part of the state of Minas Gerais, south of the São Francisco Craton (Almeida, 1967; Dorr, 1969; Almeida and Hasui, 1984) (Fig. 1). The district is geologically well known both for its gold deposits hosted in an Archean greenstone belt sequence, as well as its Superior-type BIF deposits within a Lower Proterozoic clastic-chemical sedimentary unit (e.g., Lobato et al., 2014).

Archean gneissic trondhjemite-tonalite-granodiorite (TTG) terranes make up the largest proportion of the crystalline basement of the QF, comprising four main lithostructural domes, e.g. Belo Horizonte to the north, Caeté to the northeast, Bação in the center, and Bonfim to the west of the district. According to Noce (1995), these domains consist of 3.2 Ga granitoid gneisses and minor metasedimentary rocks, which are intruded by 2.7–2.8 Ga old metatonalites, metandesites, metagranites, pegmatites and Proterozoic mafic dikes (Noce et al., 2005; Farina et al., 2015; Moreira et al., 2016). Noce et al. (2007) suggest that these TTG derive from igneous protoliths older than 2.9 Ga.

Overlying this is the Rio das Velhas Supergroup, a volcano-sedimentary greenstone belt, and Proterozoic metasedimentary units of the Minas and Espinhaço Supergroups (Dorr, 1969; Toledo, 1997; Alkmim and Marshak, 1998 and references therein; Noce, 2013). The Rio das Velhas (3.0–2.7 Ga; Machado et al., 1989; Machado and Carneiro, 1992) greenstone belt sequence is separated into the basal Nova Lima and the upper Maquiné Groups (Fig. 1). In general, rocks are regionally metamorphosed to the lower greenschist facies. The Nova Lima Group is further subdivided into three units, with basal komatiitic to tholeiitic metavolcanics interlayered with clastic metasedimentary rocks and exhalative chemical metasedimentary rocks (Vieira and Oliveira, 1988). The middle unit comprises mafic and felsic metavolcanics (tuffs) interlayered with carbonaceous metasedimentary rocks and BIF with felsic metavolcanoclastics on the top. Clastic metasedimentary rocks interlayered with mafic and felsic metavolcanoclastics comprise the upper most unit of the Rio das Velhas Supergroup, which is overlain by quartzite and conglomerate of the Maquiné Group. The Minas Supergroup is Neoarchean-Paleoproterozoic age (2.6–2.1 Ga; Babinski et al., 1991) represents a continental margin sequence, and comprises clastic chemical-sedimentary rocks. More recently, Cabral et al. (2012) dated zircons (U-Pb LA-ICP-MS) from a volcanic layer within the Minas Supergroup iron formation, and proposed a 2.65 Ga Archean age for the deposition of these rocks.

According to Baltazar and Zucchetti (2007), the detailed classification of the Rio das Velhas Supergroup into lithofacies associations takes into consideration the depositional environment of their sedimentary units and source areas (Fig. 1). Hence, the Nova Lima Group is separated into the following associations, from bottom to top: 1) a volcanic-mafic-ultramafic association, composed of tholeiites and komatiites, 2) a clastic- chemical-sedimentary association, with mafic and felsic metavolcanics interlayered with BIF and ferruginous chert, 3) a clastic-chemical-sedimentary association typically made up of

carbonaceous pelite with BIF and ferruginous chert, 4) a volcaniclastic association composed of felsic and mafic volcaniclastic rocks, and 5) the most extensive association, which is composed of resedimented rocks, primarily composed of graywackes, sandstones and siltstones. This is overlain by the coastal and non-marine associations of the Maquiné Group.

3. Deposit geology

There have been many studies on the geology and gold mineralization at Cuiabá (Vial, 1988a; Toledo, 1997; Ribeiro Rodrigues, 1998; Lobato and Vieira, 1998; Costa, 2000; Lobato et al., 2001a,b). The description that follows refers to metamorphosed rocks, and the prefix "meta" has been chosen to be omitted for brevity.

The lithostratigraphic succession at the mine area, first defined by Vial (1980), includes volcanic, volcanoclastic and sedimentary rocks, characterized by greenschist facies mineral assemblages, and structurally controlled by the Cuiabá anticlinal fold (e.g. Vitorino, 2017); detrital zircons (U-Pb-SHRIMP) yield a minimum age of 2.74 Ga for the volcanoclastics (Schrank and Machado, 1996; Lobato et al. 2001a,b). This succession is related to the lower, middle and upper units of the Nova Lima Group defined by Ladeira (1980). The description that follows is largely summarized from Lobato et al. (2001b,c) and Ribeiro Rodrigues et al. (2007).

The lower unit is characterized by a thick (> 400 m) succession of alternating layers of chloritized mafic volcanics and pelites, both carbonatized and sericitized mafic volcanics, as well as interbedded lenses of carbonaceous pelite (Fig. 2A). The basal mafic rocks are light green and fine-grained, both massive and foliated. The main minerals are amphibole, plagioclase, clinozoisite/epidote, chlorite and quartz. Vieira (1991) described the presence of pillow lavas, and variolites of andesitic composition.

Hydrothermally altered mafic volcanics are overlain by the Cuiabá BIF, which ranges from < 1 to 15 m and is dominated by dark carbonate-quartz and light carbonate-quartz bands (Lobato et al., 2001c). The BIF is nearly completely enclosed by carbonaceous pelite, consisting of muscovite, quartz, carbonate, chlorite and carbonaceous matter. Lenses of carbonaceous pelite are also present in the lower and upper mafic volcanic units. The upper unit of the Nova Lima Group consists of a succession of carbonatized, muscovitized and chloritized mafic volcanics, volcanoclastics and pelites. The upper volcanic units have basaltic compositions, with a higher Fe/Mg ratio compared to the lower, andesitic mafic unit (Vieira, 1991). Volcanoclastic rocks of dacitic to rhyolitic composition are at the top of the stratigraphic sequence, forming a 500-m thick unit that represents the most abundant rock type in the area. Quartz and plagioclase phenocrysts are the main components in a light mica-chlorite-quartz-carbonate matrix. Mafic dikes up to 30 m in thickness, crosscut all other rock types.

3.1. Structural setting

The structural evolution of the Cuiabá deposit comprises at least three deformational events, i.e. D1, D2 and D3 (Ribeiro Rodrigues, 1998). The first two deformation events, D1 and D2, developed under ductile to ductile-brittle conditions, with fault zones oriented in the NW-SE direction, and tectonic transport from SE to NW. The D3 structures formed in a brittle-ductile regime and were in an E-W-orientation under compressional stress (Xavier et al., 2000). All lithological units are affected by a pervasive axial planar foliation that is locally mylonitic (S2 = 135/45; Vitorino, 2017). They show a prominent mineral elongation lineation (LS = 126/22–35) indicated by the preferred orientation of elongated muscovite, carbonates and sulfides. Late, NW-verging, sigmoidal thrust faults reactivated pre-existing structures and caused folding, boudins and rotation of the Cuiabá BIF. There is no consensus regarding the geometry of the Cuiabá fold, which has an inverted north flank and a normal sequence in the south flank

marked by the BIF. Studies by Vial (1980), Toledo (1997), Ribeiro Rodrigues (1998, 2007) considered the Cuiabá fold as a tubular structure, plunging southeast at 30° (Vial, 1980; Toledo, 1997). Recently published data of the nearby Lamego gold deposit record that the Lamego fold structure, which is comparable with the Cuiabá fold, represents a reclined, isoclinal, cylindrical and rootless fold (Martins et al., 2016).

3.2. Gold mineralization

The Cuiabá orebodies display a strong structural control, and one prominent feature of all ore shoots is their consistent, down-plunge continuity (Ribeiro Rodrigues et al., 2007). Three different mineralization styles are defined: 1) stratabound-replacement, commonly in BIF; 2) disseminated, related to hydrothermal alteration in shear zones; and 3) shear zone related, quartz-carbonate-sulfide veins (e.g., Ribeiro Rodrigues et al., 2007, Martins et al., 2016). These styles reflect variations in fluid-rock interaction, and thereby a distinctive sulfide-gold assemblage and composition (Lobato and Vieira, 1998).

The typical sulfide mineral assemblage of the Cuiabá BIF is pyrite-pyrrhotite-arsenopyrite with minor chalcopyrite and sphalerite, and gold in equilibrium. Gold is also found as inclusions in pyrite, arsenopyrite and pyrrhotite, varying in size between 10 and 80 μm. The economic-grade gold mineralization at Cuiabá is related to six main BIF-hosted gold orebodies: 1) Balancão, 2) Canta Galo, 3) Fonte Grande, 4) Fonte Grande Sul, 5) Serrotinho, and 6) Galinheiro (Fig. 2A). These orebodies (> 4 ppm Au) represent sulfide-rich segments of the BIF, grading laterally into non-economic mineralized or barren BIF. Orebodies in association with quartz veins are the Veio de Quartzo (VQZ), Galinheiro Footwall (GAL FW), Serrotinho Footwall (SER FW) and Fonte Grande Sul Footwall (FGS FW) (Fig. 2A). Minor orebodies like Galinheiro Extensão, Surucu, Canta Galo and Dom Domingos are of secondary interest. Furthermore, mafic volcanic-hosted orebodies such as Viana and Galinheiro Quartzo are associated with the upper mafic unit and were locally mined in the past. The newly discovered gold occurrences VQZ and Serrotinho FW are hosted in the lower mafic unit, where mineralization is related to distinct hydrothermal alteration zones (Vieira, 1988; Lobato et al., 2001a,b).

The Fonte Grande Sul orebody, located in the SE closure of the Cuiabá fold, contains the richest gold ore of the mine. The orebody shows a reasonably constant thickness, between 4 and 6 m, but both the orebody area and Au content increase progressively with depth. The mineralized BIF is intensively sulfidized (Fig. 3), folded and disrupted by D1 thrust faults containing generally recrystallized and massive ores that lack banding. The BIF consists of rhythmic alternation of dark, white, and ocher-colored, millimeter- to centimeter-thick bands, rich in carbonaceous material, fine-grained quartz and carbonate, and is embedded between lower (footwall) and upper (hanging wall) mafic volcanic rocks (Xavier et al., 2000; Lobato and Vieira, 1998). The country rocks to the mineralized BIF show strong sericite, carbonate and chlorite alteration zones (Fig. 2B), typical of greenschist facies metamorphic conditions. Transitions of sulfide- rich to -poor portions of the BIF are gradational, and marked by shear zones or quartz veins.

4. Host rocks and hydrothermal alteration assemblages

4.1. Banded iron formation

The Algoma-type Cuiabá BIF (e.g., Lobato et al., 2001c) ranges in thickness between 1 and up to 15 m, and shows the characteristic alternating layering of dark (quartz-carbonate-carbonaceous matter) and light orange (quartz-carbonate-chert) bands (Figs. 3A, 4). Pyrite, pyrrhotite and arsenopyrite are abundant and in equilibrium, accompanied by gold grains in fractures and along contacts between sulfide grains. Two individual BIF sequences within the Cuiabá mine can be distinguished, and are separated by a 15 cm mafic volcanic unit. The lower

BIF, typically banded with abundant Fe-carbonate, and carbonaceous material, is the main host to the gold mineralization. The upper BIF consists of highly deformed, ferruginous chert as well as carbonaceous matter (Lobato et al., 2001c).

4.2. Carbonaceous pelite

Pelites surrounding the Cuiabá BIF mainly consist of carbonaceous matter, hydrothermal smoky (Qz1) and granoblastic quartz (Qz2), carbonate minerals, chert layers, chlorite, muscovite and sulfide minerals (Fig. 4). The latter phases are pyrite, arsenopyrite with minor proportions of pyrrhotite, chalcopyrite and sphalerite (Fig. 3D). Free gold is observed in equilibrium with sulfides and dispersed in the carbonaceous material. The well defined lithological boundary between carbonaceous pelites and mafic volcanics varies from concordant to slightly deformed. However, the contact between carbonaceous pelite and the Cuiabá BIF is intensely deformed.

4.3. Andesite

The mafic volcanics contain a typical alteration assemblage of the chlorite hydrothermal alteration zone with albite ± epidote ± zoisite (clinozoisite) ± quartz ± actinolite ± carbonate ± chlorite (Figs. 3B and E, 4), previously described by Vieira (1987). The absence of hornblende serves as indication that peak metamorphic conditions did not exceed the greenschist-amphibolite facies transition (Spear, 1995). Sulfide minerals are accessory and include mainly pyrite, chalcopyrite and sphalerite in equilibrium (Fig. 4). They appear dispersed in the matrix, and are commonly associated with carbonate minerals. Gold mineralization is in equilibrium with pyrite. Lenses of carbonaceous pelite also occur within the lower and upper mafic volcanic units.

5. Materials and Methods

Three diamond drill holes CBABSD03A, CBABSD04B and CBABSD009 were sampled for this study. All of them represent the detailed lithostratigraphic succession of the FGS orebody (Fig. 2B), including sulfide-rich BIF, carbonaceous pelite and andesite. Host rocks were sampled bearing visible sulfide minerals linked to the main foliation (S2) and different degrees of hydrothermal alteration were especially targeted for sampling. About 40 samples were used to prepare 34 polished thin sections. Hand specimens and polished thin sections have been described petrographically with regards to gangue and ore minerals.

5.1. Electron probe micro analyzer (EPMA)

Quantitative analyses and element maps were carried out at the Centre of Microscopy at the Federal University of Minas Gerais, Brazil. By using the electron probe micro analyzer JEOL JXA 8900RL, with an accelerating voltage of 15 kV, dwell time of 50 ms and beam current of 80nA, element maps of the following elements were produced: Fe, Zn, As, Ag with EDS and S, Sb, Au, Co, Ni and Cu, with a WDS system depending on the appropriate crystal.

5.2. Laser ablation inductively coupled plasma mass spectroscopy (LA-ICP-MS)

Eleven polished thin sections were selected to examine the trace element compositions of pyrite, pyrrhotite and arsenopyrite in different host rocks by analyzing the following 16 elements (with detection limits in ppm if not otherwise specified): ^{29}Si, ^{34}S (0.4 wt%), ^{55}Mn (4.8), ^{58}Fe (0.1 wt%), ^{59}Co (1.5), ^{60}Ni (4.6), ^{70}Zn (0.05), ^{73}Ge (5.3), ^{75}As (1.6), ^{108}Ag (0.7), ^{115}In (0.3), ^{197}Au (0.7), ^{201}Hg (10.0), ^{208}Pb (0.3), ^{205}Tl (0.3) and ^{209}Bi (0.1). Analyses were conducted at the Institute of Mineralogy and Economic Geology, Laboratory of Geochemistry, at the
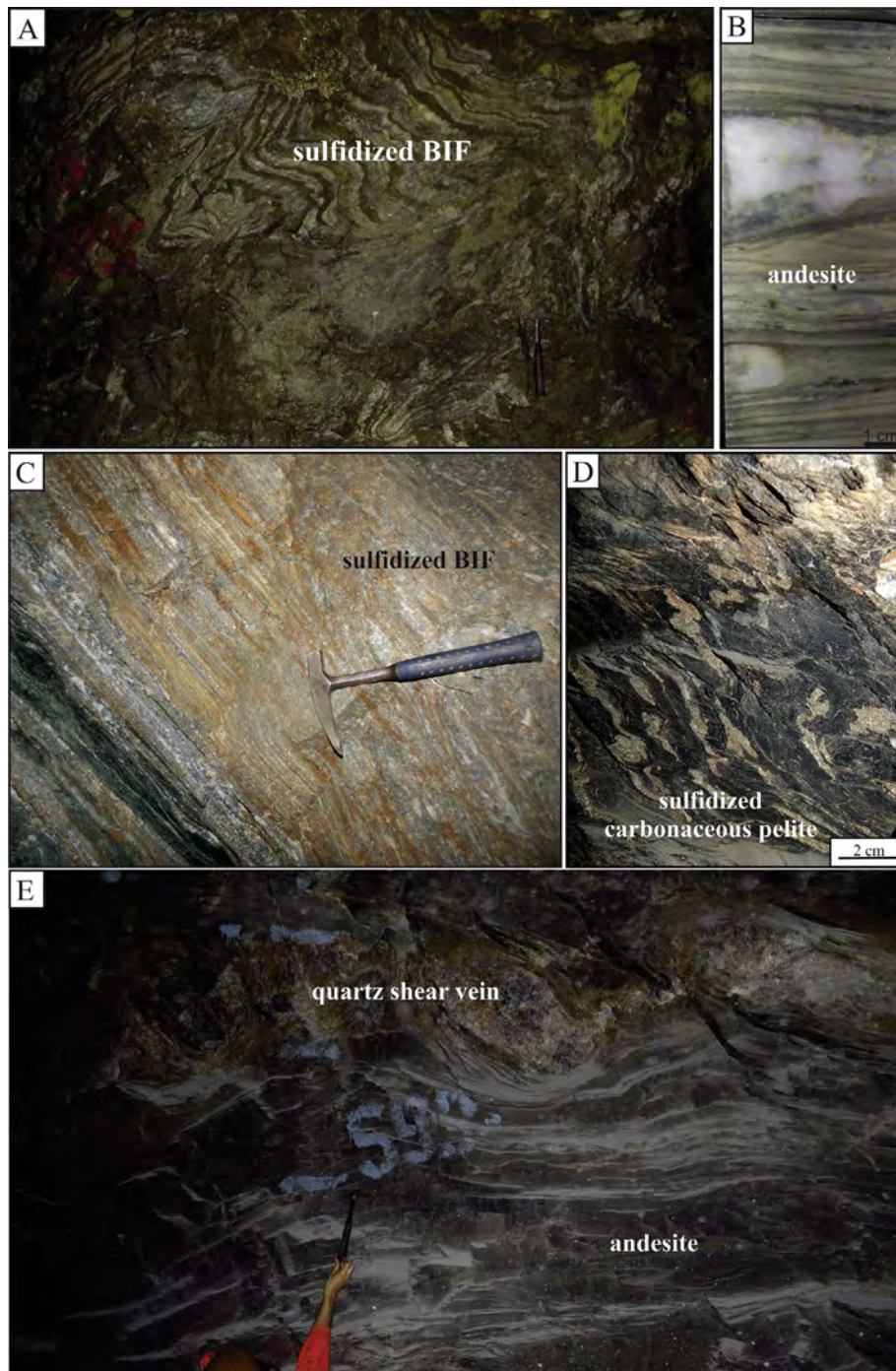
Fig. 3. Photographs of mineralized host rocks. Stope view of sulfidized BIF (Level 15, FGS orebody) (A). Sampled drill core of sulfidized andesite (drill core 03A, 1414.70–1414.84, FGS orebody) (B). Stope view of sulfidized BIF (Level 18, Serrotinho orebody) (C). Stope view of sulfidized carbonaceous pelite (Level 15, Galinheiro FW orebody) (D). Stope view of hydrothermally altered andesite and quartz shear veins (Level 15, VQZ orebody) (E).

RWTH University of Aachen, Germany. Measurements were carried out using a New wave UP-193 laser microprobe coupled with an ICP-MS system (ELAN DRC-e) under the following conditions: Standard: Mass-1 (powder pressed pellet); dwell time 10 ms; spot size 35–150 μm; Argon/ Helium ratio 0.8/0.6; frequency 4 Hz. Standardized trace element values were used from the USGS and Wilson et al. (2002). Data treatment and reduction were made by an in-house software, developed at the Laboratory of Inorganic Chemistry at the ETH Zürich. The analytical mass spectra were reduced and evaluated individually in order to eliminate contamination effects. Each analytical spectrum was reduced manually. Peaks of elements such as Si, Ca, Al, K and Mg are typically indicative of gangue mineral inclusions. These elements are not certified for Mass-1, and consequently were not quantified. A detailed description regarding the LA-ICP-MS analyses on sulfide minerals is described by Danyushevsky et al. (2011).

5.3. Secondary ion mass spectroscopy (SIMS)

In-situ multiple sulfur isotope composition ($^{33}S/^{32}S$, $^{34}S/^{32}S$, $^{36}S/^{32}S$) was measured using secondary ion mass spectrometry (SIMS), Cameca IMS-1280 at the Centre for Microscopy, Characterization and Analysis (CMCA), University of Western Australia (UWA), Perth,
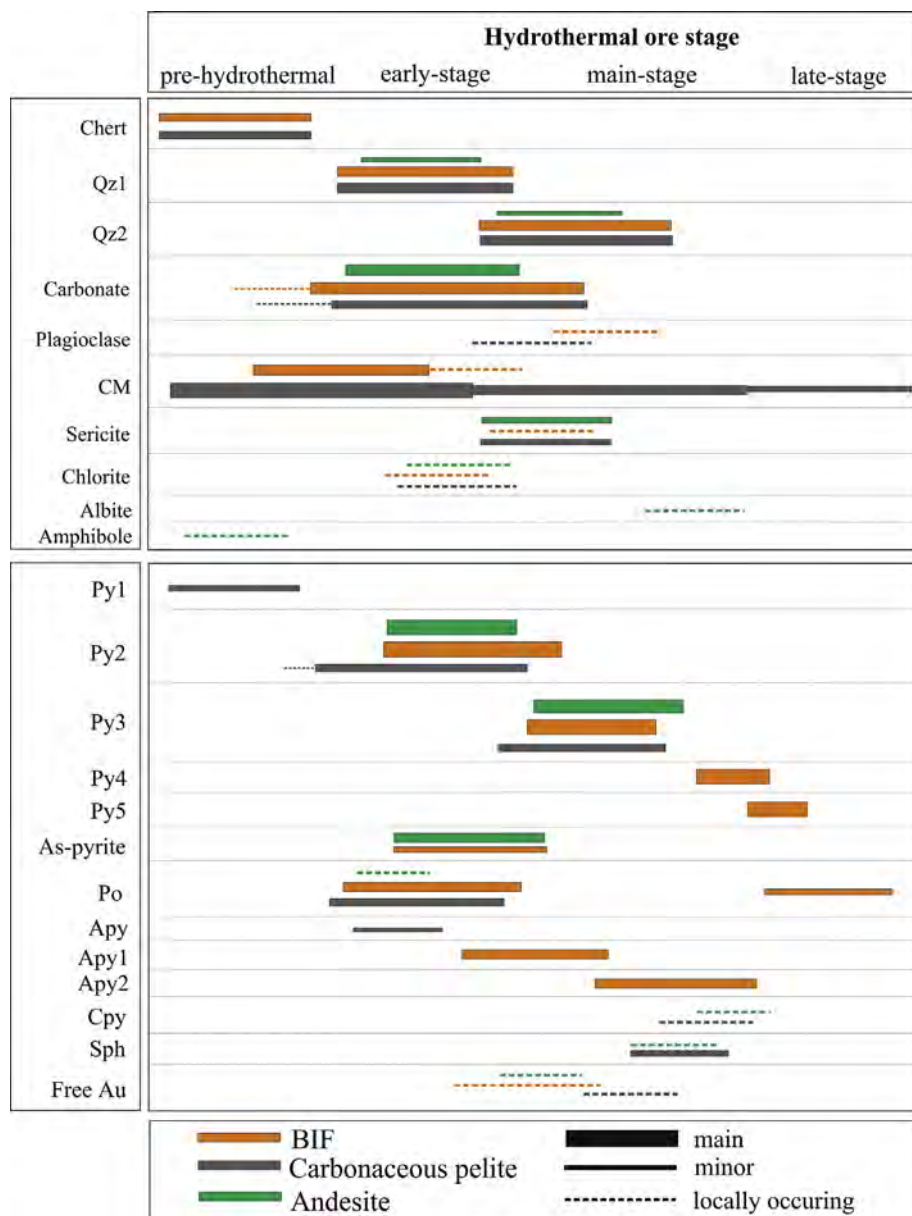
Fig. 4. Mineralogical paragenesis of gangue and ore minerals of BIF, carbonaceous pelite and andesite. Abbreviations: Qz1 = smoky quartz, Qz2 = granoblastic quartz, CM = carbonaceous matter, Py = pyrite, Po = pyrrhotite, As-Py = arsenic pyrite, Apy = arsenopyrite, Cpy = chalcopyrite, Sph = sphalerite.

Australia. Sierra pyrite (FeS$_2$) and Alexo pyrrhotite (Fe(1 − x)S) were used as sulfur isotope standards, both chemically characterized by electron microprobe analyses, and isotopically characterized for δ^{33}S, δ^{34}S, and δ^{36}S by fluorination gas-source mass spectrometry, and tested for homogeneity at the microscale by secondary ion mass spectrometry (LaFlamme et al., 2016). Analytical conditions and data reduction processes were similar as described in LaFlamme et al. (2016), and summarized here. A ca. 1–4nA focused Cs$^+$ primary beam was operated at 10 kV, and the secondary ion beam was extracted at −10 kV. The analysis area was presputtered using a 20 × 20 µm raster for 45 s followed by automated secondary centering in the field aperture (FA; 3000 µm) and entrance slit (ES; 60 µm). The analysis used a 15 × 15 µm raster employing dynamic transfer at a 100× field magnification for 20 × 4 s integrations. Four sulfur isotopes were measured simultaneously using three Faraday Cup (FC) detectors with amplifiers of 10^{10} Ω resistor for ^{32}S and 10^{11} Ω for ^{33}S and ^{34}S, and an electron multiplier (EM) detector for ^{36}S. Exit slit of 250 um was used on each of the multicollector detectors, providing a nominal mass resolving power

(MRP) of ca. 5000, sufficient to separate the ^{32}S ^{1}H from ^{33}S peak. The magnetic field was regulated using nuclear magnetic resonance (NMR). Typical ^{32}S count rate was ∼ 1.5 × 10^9 cps, approximately corresponding to ^{36}S count rate of ∼2.0 × 10^5 cps, causing enough EM aging during an analysis session. The EM high voltage (HV) was adjusted automatically before every analysis, thus minimizing the effect of EM aging on reproducibility. The uncertainty (2SD) on individual measurements is equal to ∼0.30‰ on δ^{34}S, ∼0.22‰ on Δ^{33}S and ∼0.96‰ on Δ^{36}S. In total, 22 rock fragments from 9 samples were analyzed, including pyrite and pyrrhotite of sulfide-rich BIF, carbonaceous pelite and andesite.

6. Ore petrography and sulfide textures

The studied hydrothermally altered and mineralized host lithologies include carbonaceous pelite, BIF and andesite, which reveal five different pyrite types. The Py1 is classified as synsedimentary to diagenetic, based on its fine-grained, spongy, anhedral and euhedral nature,
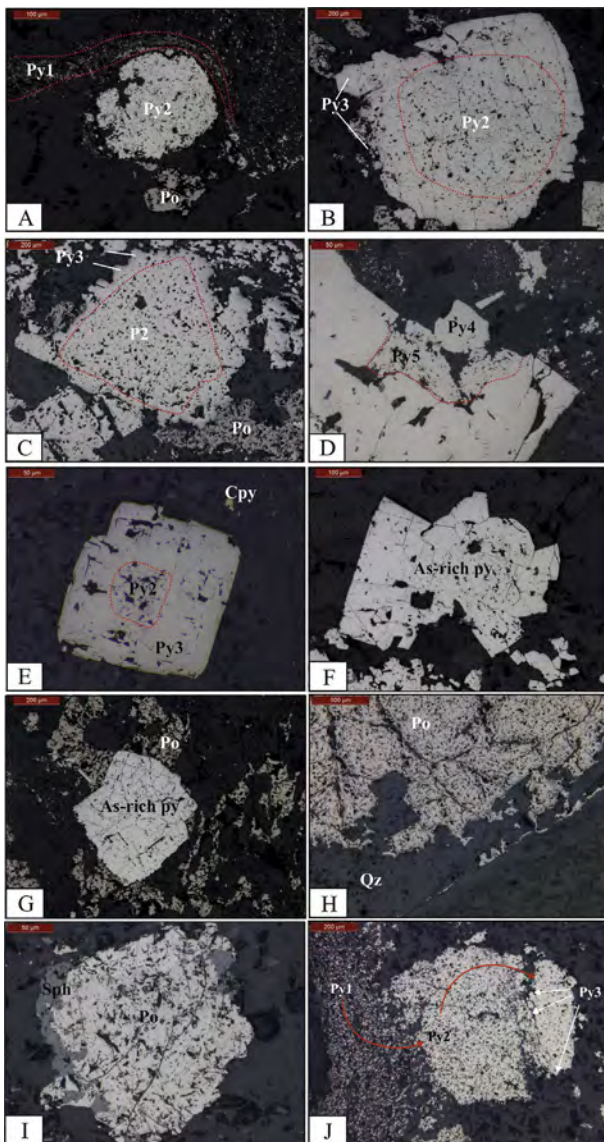
Fig. 5. Photomicrographs taken under reflected light and uncrossed nicols of pyrite, pyrrhotite and arsenopyrite types. Py1 as spongy, fine-grained anhedral and euhedral grains building up Py2 to a rounded aggregate in carbonaceous pelite (009_8B) (A). Porous Py2 surrounded by Py3 in carbonaceous pelite (009_8B) (B). Euhedral Py3 overgrowing Py2 in BIF (04B_5A) (C). Smooth Py4 in BIF overgrown by Py5 (04B_5A) (D). Py2 overgrown by Py3 in andesite (03A_2) (E). Arsenian pyrite in andesite (03A_1) (F). Arsenian pyrite in BIF (03A_5B) (G). Massive pyrrhotite in BIF-hosted quartz vein (04B_7) (H). Porous and fractured pyrrhotite in equilibrium with sphalerite in quartz vein within carbonaceous pelite (009_15) (I). Pyrite development from spongy Py1, over porous Py2 to smooth euhedral Py3 in the carbonaceous pelite (04B_16). Abbreviations see Fig. 4.

forming disseminated aggregates (Fig. 5A), embedded in the bedding of the carbonaceous pelite. However, Py1 is seldom observed in the Fonte Grande Sul orebody. Agglomerating of Py1 gives place to the typically porous Py2 (Fig. 5A, B). This second pyrite type (Py2) is also observed in BIF and andesite. Porous Py2 commonly dominates the central portions (Fig. 5B, C, F) of pyrite grains, which are overgrown by a third type, classified as Py3, which constitutes smooth, subhedral to euhedral borders (Fig. 5C). The Py4 appears as smooth, nearly isolated grains (Fig. 5D); Py5 overgrows Py4 as fine-grained, euhedral margins, with the latter two only observed in BIF (Fig. 5D).

Pyrrhotite and arsenopyrite types differ in occurrence, morphology and mineral associations. Four different pyrrhotite types are identified

in BIF, quartz veins and carbonaceous pelites. (Po1) Early-stage pyrrhotite of BIF; (Po2) Late-stage pyrrhotite of quartz-pyrrhotite veins; and (Po3) Early- and (Po4) Late-stage pyrrhotite in carbonaceous pelite. Pyrrhotite (Po1) aggregates are anhedral, elongated, and form patches; it is replaced by pyrite and arsenopyrite (Fig. 5F). Pyrrhotite (Po1) and (Po2) form anhedral massive aggregates (Fig. 5H). Pyrrhotite (Po3) is laminated in equilibrium with arsenopyrite and chalcopyrite; where less altered, carbonate is replaced by pyrrhotite (Fig. 5C). Porous and fractured pyrrhotite (Po4) together with sphalerite is present in quartz veins within carbonaceous pelite (Fig. 5I). Arsenopyrite forms euhedral and subhedral grains, intergrown with pyrite, and may be distinguished into porous (Apy1) and smooth (Apy2) varieties in BIF. Arsenian pyrite is present in sulfidized BIF and andesite (Fig. 5F, G); the optical differentiation between arsenian pyrite and arsenopyrite is uncertain due to habit and color. Fig. 5J shows the pyrite development from spongy Py1, the agglomeration to Py2, and the fine-grained euhedral Py3 grains in the carbonaceous pelite. In general, free gold is present along the contact between Py2 and Py3, as well as in fractures within pyrite, arsenopyrite and pyrrhotite.

7. Analytical results

7.1. EPMA maps of trace element variation

Based on visible textural differences, which have been displayed by backscattered electron images-BSE (Fig. A1), sulfide minerals were analyzed for elemental composition. Pyrite and arsenopyrite were analyzed quantitatively for Fe, S, As, Co, Ni, Ag and Au. Pyrrhotite was analyzed for the same elements, except Ag and Au.

In general, pyrite types in BIF show similar trace element values, whereas Py3 and Py4 have lower trace element concentrations (Table 1). The analyzed pyrite in carbonaceous pelite has much higher mean concentrations of trace elements such as Co (0.05 wt%), Ni (0.05 to 0.07 wt%) and As (0.20 to 0.24 wt%). Mean gold values are similar in carbonaceous pelite (0.01 wt%), andesite (0.02 wt%) and BIF (0.01 wt%).

In addition to the quantitative analyses, electron microprobe maps were generated (Fig. 6). They are extremely useful for displaying element distribution in the textural context, particularly for showing compositional zonation in sulfide minerals. Significant zonation is seen in Py2 and Py3 in andesite, arsenopyrite in BIF, and between Py2 and Py3 in carbonaceous pelite. The BSE images (Fig. A1), showing the Py2 to Py3 transition in carbonaceous pelite, demonstrates euhedral Py3 overgrowing Py2. Cobalt and Ni are enriched from Py2 to Py3, and a weak S and As zonation (Fig. 6A). The Py2 and Py3 of andesite can be clearly separated due to their S and As zonation, with Co and Ni variation constrained to the porous center represented by Py2 (Fig. 6B). Both the Au and Ag maps show two inclusions of an Au-Ag alloy in the transition between Py2 and Py3. The Fe map represents an Fe chlorite surrounding an euhedral pyrite grain (Fig. 6B).

The element distribution in BIF arsenopyrite shows Fe, S and As enrichment in the central grain portions. Arsenopyrite borders have a Co peripheral enrichment. Transitions between Py2 and Py3, or Py4 and Py5, which display differences in their gray scale in BSE images, did not become evident in elemental distribution maps. Low detectability of trace elements may have been the reason.

7.2. Pyrite LA- ICP-MS data

In situ LA-ICP-MS analyses were conducted in pyrite, pyrrhotite and arsenopyrite from the Cuiabá gold deposit. Samples include disseminated sulfide minerals in altered host rock and quartz veins, and massive sulfide layers in BIF. Laser ablation ICP-MS spectra provide insight into lattice-bound and inclusion-related elements in sulfide minerals (Fig. 7). The statistical summary of the pyrite, pyrrhotite and arsenopyrite data set is presented in Tables 2, 3 and 4.

Table 1

Statistical summary of electron microprobe analyses of pyrite and pyrrhotite in carbonaceous pelite, BIF and andesite in wt%

Host rock	Mineral	Sample ID		As	Fe	S	Au	Ag	Co	Ni	Total
Carbonaceous pelite	Py1 to Py2	009_8B	Min	0.05	35.99	40.82	0.00	0.00	0.01	0.04	88.91
			Max	0.42	45.42	53.02	0.01	0.02	0.09	0.14	97.82
			Mean	0.20	43.37	50.76	0.00	0.00	0.05	0.07	95.41
			Median	0.17	43.72	51.49	0.00	0.00	0.05	0.06	95.86
			SD	0.10	1.97	2.70	0.00	0.01	0.02	0.03	1.99
	Py2 to Py3	009_8A/009_8B	Min	0.01	39.83	42.14	0.00	0.00	0.00	0.00	82.03
			Max	0.82	45.37	53.11	0.06	0.01	1.06	0.23	98.39
			Mean	0.24	44.53	51.93	0.01	0.00	0.05	0.05	96.82
			Median	0.19	44.75	52.32	0.00	0.00	0.02	0.03	97.44
Andesite	Transition fromPy2 to Py3	03A-Am2(n = 24)	Min	0.03	42.66	49.49	0.00	0.00	0.00	0.00	94.10
			Max	2.27	44.43	52.08	0.07	0.02	0.07	0.19	96.88
			Mean	0.78	43.45	51.13	0.02	0.00	0.01	0.03	95.42
			Median	0.61	43.49	51.28	0.01	0.00	0.01	0.01	95.46
BIF	Py2 to Py3	4B_5/009_1/4B_6(n = 56)	Min	0.01	8.22	9.53	0.00	0.00	0.00	0.00	18.13
			Max	2.01	46.48	54.23	0.07	0.01	0.04	0.04	100.00
			Mean	0.33	44.89	52.14	0.01	0.00	0.01	0.01	97.39
			Median	0.13	45.65	53.17	0.00	0.00	0.00	0.01	99.21
	Py4 to Py5	4B_5(n = 15)	Min	0.06	43.32	50.22	0.00	0.00	0.00	0.00	93.82
			Max	0.22	46.07	53.39	0.02	0.01	0.02	0.04	99.52
			Mean	0.13	44.96	52.56	0.00	0.00	0.01	0.02	97.69
			Median	0.12	45.21	52.75	0.00	0.00	0.01	0.02	98.21
Late-stagequartz-pyrrhotite veins	Late-stage pyrrhotite	4B_7(n = 15)	Min	0.01	59.39	36.57	–	–	0.00	0.00	96.65
			Max	0.08	61.13	39.81	–	–	0.02	0.04	99.97
			Mean	0.05	60.29	39.19	–	–	0.01	0.02	99.34
			Median	0.05	60.29	39.47	–	–	0.01	0.02	99.68
Carbonaceous pelite	Porous pyrrhotite	009_15 (n = 30)	Min	0.01	54.09	34.93	–	–	0.02	0.64	92.03
			Max	0.08	61.61	39.61	–	–	0.05	0.74	100.00
			Mean	0.04	58.99	38.96	–	–	0.04	0.67	98.70
			Median	0.04	59.11	39.11	–	–	0.04	0.67	99.03
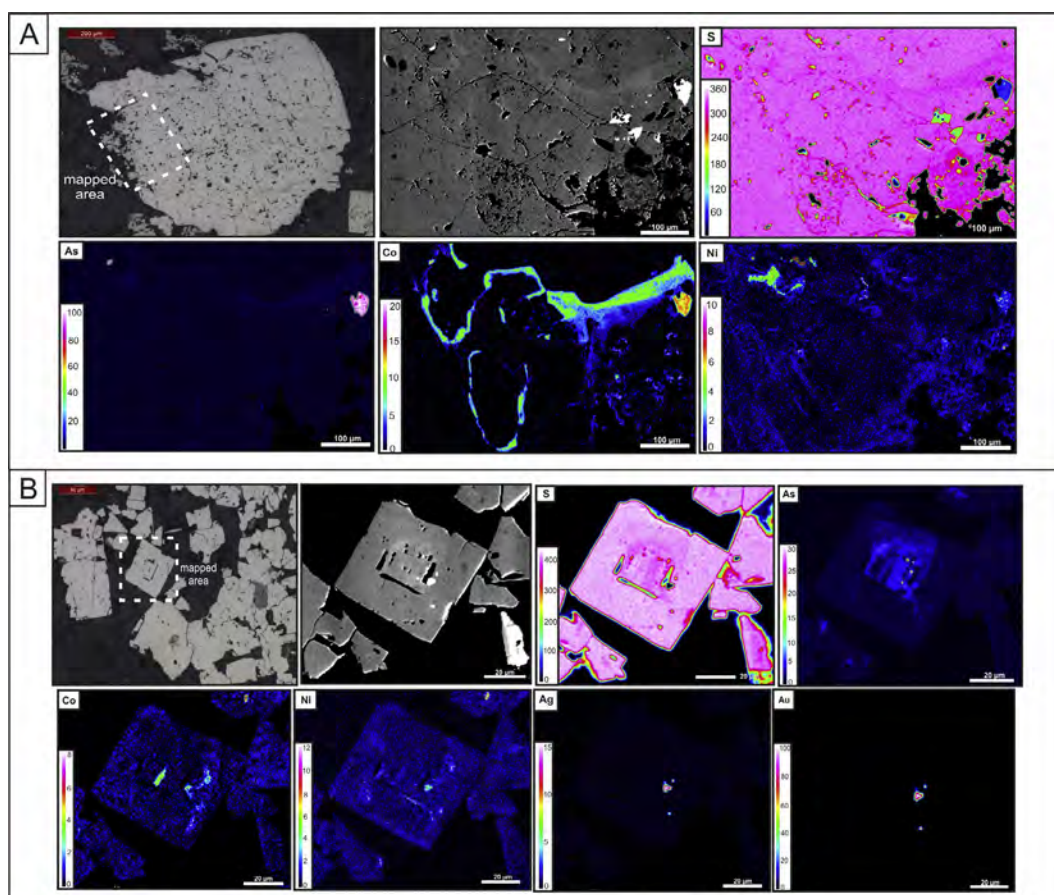
Fig. 6. Element maps of Py2 and Py3 in carbonaceous pelite (A) and andesite (B): BSE image and element maps of Fe, S, As, Co, Ni, Ag and Au. Color bars are given in cps.
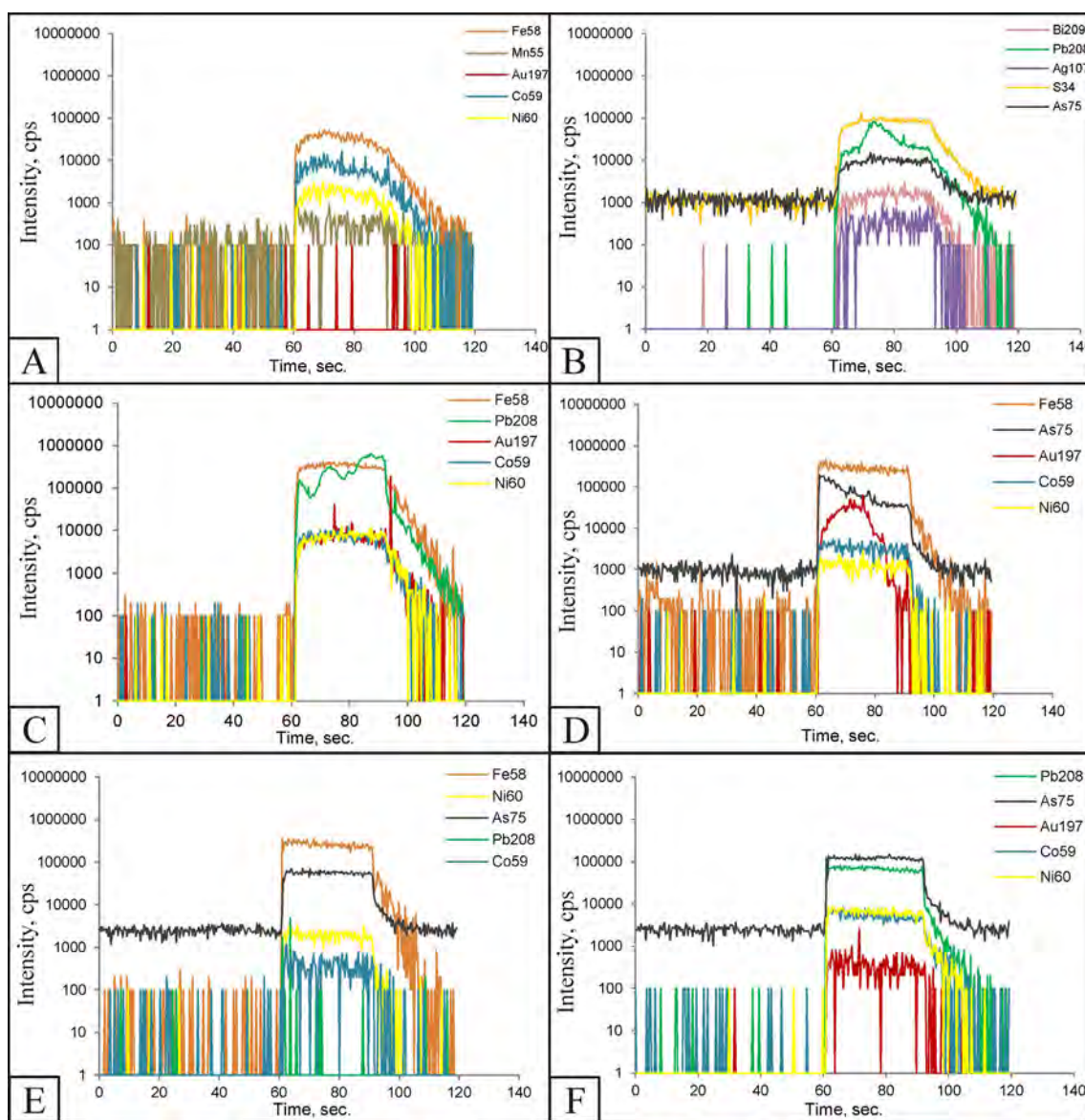
Fig. 7. LA-ICP-MS ablation spectra of pyrite analyses displaying intensity in count per second (cps) versus acquisition time (sec). Carbonaceous pelite: Py1: As-Co-Ni-(Mn)-(Bi) rich pyrite (A/B). Andesite: Porous Py2: Pb-Co-Ni rich pyrite with lattice-bound and inclusion-related Au (C). BIF: Py3 with lattice-bound Co, Ni and As, and inclusion-related Au (D). BIF: Py4: Co-Ni-As rich pyrite (E). BIF: Py5: Pb-Co-Ni rich pyrite with inclusion-related Au (F).

Lattice bound or evenly distributed nano-inclusions elements: A flat element profile in time resolved laser ablation output graphs may indicate that the trace elements are held in the pyrite lattice or as evenly distributed nao-inclusions (Gregory et al., 2014).

In carbonaceous pelite, Co-Ni-Mn-Pb-As ± Ag ± Bi form flat and consistent spectra profiles for Py1. In contrast, Py2 shows flat signals for Co, Ni, Pb and (As), and Py3 shows similar spectra profiles to Py1 (Fig. 7A, B). Lattice-bound elements in Py2 and Py3, such as Co, Ni and As, form flat and consistent spectra profiles in andesite and BIF (Fig. 7C, D). Lead and Au partly display flat signals, and may fit in lattice of Py2 and Py3 of both andesite and BIF (Fig. 7C, D).

Inclusion-related elements: Gold and Ag display irregular profiles indicative for inclusion-related elements (Gregory et al., 2014). This is present in Py2 and/or Py3 of andesite and BIF, as is the case with Pb; these most likely represent galena inclusions in pyrite.

In carbonaceous pelite (Fig. 8), Py1 is the only paragenetic type that consistently forms a specific population. While Py3 generally shows good elemental correlations, Py2 is more variable in its trace element distribution. For example, one population of Py1 is highlighted in the

Co versus Ni binary plot (R_{Py1} = 0.28) (Fig. 8A), with high Ni and relatively lower Co; Py2 shows a good positive correlation, whereas Py3 has two populations correlating positively (R_{Py3} = 0.15) (Fig. 8A). The Ag and Pb binary plot indicates a weak positive correlation of Py1 (R_{Py1} = 0.35) and Py3 (R_{Py3} = 0.64), while Py2 displays no true correlation (R_{Py2} = −0.55), but two populations at relatively high Ag and Pb and lower Ag and Pb (Fig. 8C). Silver and Bi concentrations of Py1 and Py3 display a positive correlation (R_{Py1} = 0.49, R_{Py3} = 0.86); Py2 shows two populations: 1) higher Ag and Bi values (10–100 ppm), and 2) lower Ag and Bi (1–5 ppm) (Fig. 8D).

From the four pyrite types in <u>BIF</u>, porous Py2 generally shows good trace element correlations, whereas smooth Py3 and Py4 correlate poorly. The 'overgrowing' Py5 has consistently high trace element values (e.g., Co, Ni, As, Bi). The Co versus Ni binary plot displays a positive correlation for Py2 (R_{Py2} = 0.31), and a flat correlation for Py3 (R_{Py3} = 0.01). The Py4 shows a weak positive correlation of Co and Ni (R_{Py4} = 0.32); Py5 forms one population at high Ni and lower Co concentrations (Fig. 9A). The Py2 forms two populations in the As-Ni plot, the first with a positive correlation at high As and Ni values, and

Table 2

LA-ICP-MS concentration data of pyrite analyses in carbonaceous pelite (CP), BIF and andesite. Trace element concentrations are given in wt% and ppm. SD = Standard deviation, bdl = below detection limit.

Sample	S [wt%] Max.	Min.	SD	Mean	Mn Max.	Min.	SD	Mean	Fe [wt%] Max.	Min.	SD	Mean	Co Max.	Min.	SD	Mean	Ni Max.	Min.	SD	Mean
Py1 CP	51.8	49.0	1.4	50.3	51.67	17.90	12.19	30.51	83.0	67.8	4.7	74.2	889.0	321.0	168.9	617.3	1673.0	549.04	351.99	951.59
Py2 CP	51.8	51.8	0.0	51.8	177.23	22.13	89.48	73.91	81.3	54.1	6.6	64.0	6193.1	9.0	1420.2	591.6	1601.6	50.2	373.4	416.4
BIF	53.7	23.2	8.1	49.8	341.27	2.07	68.76	41.57	75.6	19.2	11.4	55.9	177.8	1.7	42.7	26.5	351.5	5.08	74.63	53.60
Andesite	51.3	51.3	–	51.3	146.51	4.31	49.53	33.46	70.4	51.0	5.0	59.7	515.4	16.1	116.6	124.2	514.6	50.71	146.54	286.01
Py3 CP	51.8	51.8	0.0	51.8	32.07	19.12	6.59	26.30	83.2	53.0	8.3	67.7	1108	17.4	303.9	357.6	1455.0	58.51	338.97	579.75
BIF	53.7	23.3	10.7	48.4	923.03	4.64	291.26	134.13	71.2	21.9	13.0	51.9	668.55	1.3	152.7	86.3	238.6	6.31	48.90	51.02
Andesite	51.3	51.3	–	51.3	13.08	1.40	3.93	4.55	76.0	47.2	7.4	61.5	481.04	28.4	124.5	227.9	1381.3	174.65	322.05	505.38
Py4 BIF	53.7	52.9	0.3	53.1	bdl				64.0	56.4	2.7	59.2	123.6	3.1	38.7	44.2	118.0	8.2	34.5	67.5
Py5 BIF	52.0	52.0	0.0	52.0	110.84	6.66	51.33	33.88	64.0	56.7	3.3	61.3	55.4	42.9	5.9	49.5	348.0	137.7	92.6	269.6

Sample	As Max.	Min.	SD	Mean	Ag Max.	Min.	SD	Mean	Au Max.	Min.	SD	Mean	In Max.	Min.	SD	Mean
Py1 CP	3635	1403	684	2401	60.64	19.49	10.72	35.10	bdl				40.53	2.15	13.85	11.27
Py2 CP	9204	297	2649	2054	40.06	1.47	14.25	16.02	bdl				6.64	0.83	4.11	3.74
BIF	32,032	188	8123	7070	43.18	0.23	8.24	5.93	246.59	0.27	50.61	37.36	0.76	0.35	0.15	0.48
Andesite	32,390	2033	8235	14,923	184.17	0.57	43.42	18.31	704.46	0.34	161.89	62.60	1.29	0.25	0.54	0.68
Py3 CP	6789	727	1193	2337	43.67	1.67	12.45	21.76	6.20	3.13	2.17	4.66	16.31	0.90	4.85	5.79
BIF	37,860	434	8740	5601	36.13	0.50	11.02	7.74	217.34	0.23	65.87	36.15	bdl			
Andesite	18,817	1137	4448	6053	126.42	1.31	37.00	15.04	79.48	0.68	26.60	15.49	0.26	0.25	0.01	0.26
Py 4 BIF	2761	916	597	1401	36.13	0.66	20.13	12.89	bdl				bdl			
Pyrite 5 BIF	4510	1172	1542	2727	4.57	2.10	1.05	3.32	3.79	2.43	0.78	3.32	bdl			

Sample	Pb Max.	Min.	SD	Mean	Bi Max.	Min.	SD	Mean	Zn Max.	Min.	SD	Mean	Tl Max.	Min.	SD	Mean
Py1 CP	2968.0	258.0	761.4	938.2	62.68	11.36	12.80	35.16	11.39	0.57	3.89	2.41	17.86	1.15	5.71	10.27
Py2 CP	2282.3	0.8	598.3	362.4	46.28	0.93	17.00	13.52	bdl				8.13	3.37	3.36	5.75
BIF	1108.6	1.0	156.2	76.2	2.70	0.11	0.66	0.86	0.08	0.06	0.01	0.07	bdl			
Andesite	1194.5	2.7	321.2	189.8	11.70	0.17	3.11	2.41	0.48	0.06	0.30	0.27	bdl			
Py3 CP	6767.6	1.1	1693.1	1119.3	61.85	0.88	14.26	23.28	3.71	0.24	1.18	1.44	29.59	1.78	10.30	13.58
BIF	1106.1	0.3	188.4	68.9	1.19	0.12	0.35	0.61	0.32	0.12	0.14	0.22	bdl			
Andesite	29.0	0.4	11.1	12.1	62.57	0.07	19.42	7.37	0.18	0.02	0.09	0.08	bdl			
Py4 BIF	82.0	5.2	25.7	20.3	0.66	0.29	0.19	0.45	bdl				bdl			
Py5 BIF	350.1	169.0	75.1	263.8	12.42	5.81	2.71	9.06	bdl				2.14	0.85	0.56	1.66

Table 3

LA-ICP-MS data of pyrrhotite analyses in carbonaceous pelite (CP), BIF and andesite. Element concentrations are given in wt% and ppm. SD = Standard deviation, bdl = below detection limit.

	S [wt%]				Mn				Fe [wt%]				Ni			
	Max	Min	SD	Mean	Max	Min	SD	Mean	Max	Min	SD	Mean.	Max	Min	SD	Mean
Anhedral early-stage pyrrhotite																
CP	39.0	39.0	0.0	39.0	bdl				105.3	80.0	7.4	97.4	1937.0	1346.0	173.6	1620.4
BIF	39.0	39.0	0.0	39.0	709.3	18.8	188.9	115.3	90.1	66.0	6.6	81.1	461.2	199.9	93.5	301.9
Porous pyrrhotite																
CP	39.0	39.0	0.0	39.0	bdl				181.7	150.1	7.6	164.7	8535.2	7020.2	408.1	7754.5
Massive late-stage pyrrhotite																
BIF-hosted quarz-pyrrhotite vein	39.0	39.0	0.0	39.0	13.2	4.2	5.1	10.2	73.9	60.3	3.6	67.6	218.7	114.3	37.7	151.2

	As				Ag				In				Co				Au			
	Max	Min	SD	Mean	Max	Min	SD	Mean	Max	Min	SD	Mean	Max	Min	SD	Mean	Max	Min	SD	Mean
Anhedral early-stage pyrrhotite																				
CP	bdl				bdl				bdl				bdl				bdl			
BIF	823.7	239.3	186.4	440.9	bdl				bdl				bdl				5.9	3.4	1.3	4.8
Porous pyrrhotite																				
CP	bdl				21.9	2.5	3.5	8.0	17.9	1.0	4.4	5.2	477.9	363.1	27.5	418.4	bdl			
Massive late-stage pyrrhotite																				
, BIF-hosted quarz-pyrrhotite vein	bdl				7.5	0.7	1.5	2.4	bdl				33.3	22.9	3.6	28.4	bdl			

	Pb				Tl				Bi				Zn			
	Max	Min	SD	Mean	Max	Min	SD	Mean	Max	Min	SD	Mean	Max	Min	SD	Mean
Anhedral early-stage pyrrhotite																
CP	10.2	3.2	3.2	6.6	bdl				bdl				bdl			
BIF	67.2	1.7	20.0	21.9	bdl				1.1	0.5	0.3	0.8	bdl			
Porous pyrrhotite																
CP	1752.7	146.6	307.4	647.7	1.3	0.5	0.3	0.8	45.5	8.9	9.3	32.2	8.5	0.2	1.7	1.8
Massive late-stage pyrrhotite																
BIF-hosted quarz-pyrrhotite vein	3.9	0.4	0.8	1.5	bdl				bdl				bdl			

Table 4
LA-ICP-MS concentration data of arsenopyrite analyses in carbonaceous pelite (CP) and BIF. Element concentrations are given in wt% and ppm. SD = Standard deviation.

	S [wt%]				As [wt%]				Fe [wt%]				Mn				Co				Ni				Bi			
	Max	Min	SD	Mean	Max	Min	SD	Mean	Max	Min	SD	Mean	Max	Min	SD	Mean	Max	Min	SD	Mean	Max	Min	SD	Mean	Max	Min	SD	Mean
CP	21.9	21.9	0.0	21.9	51.0	35.4	5.7	44.4	136.7	62.6	30.1	85.4	bdl				16122.6	15,153	400.7	15,460	9037	2682	2591	4610	11.3	5.0	2.6	7.7
BIF Apy 1	23.0	23.0	0.0	23.0	38.9	18.3	5.6	27.9	40.6	24.6	4.2	31.3	340.9	6.9	98.5	82.0	59.5	2.3	15.2	15.7	404.9	11.4	96.0	49.6	4.2	0.3	1.1	1.7
BIF Apy 2	24.6	23.3	0.5	23.5	35.6	12.7	7.0	28	38.3	27.5	3.6	34.5	400.9	12.5	161.3	136.9	42.5	5.3	13.6	27.8	492.8	11.7	198.4	153.6	3.3	0.7	1.0	1.7

	Au				Pb				Tl			
	Max	Min	SD	Mean	Max	Min	SD	Mean	Max	Min	SD	Mean
CP	8.4	3.7	1.9	6.3	240.3	85.1	57.9	179.5	6.7	2.1	2.4	3.9
BIF Apy 1	10.1	0.9	3.5	4.2	1570.9	8.2	427.7	244.5	bdl			
BIF Apy 2	2.3	1.0	0.5	1.8	495.9	9.4	142.5	103.6	bdl			

the second with consistent As and higher Ni concentrations. The Py4 delineates one population at higher As and lower Ni values (Fig. 9B). The Ag and Bi binary plot portrays positive correlations for Py2 (R_{Py2} = 0.39) and Py5 (R_{Py5} = 0.98) (Fig. 9C).

The Py2 and Py3 hosted in <u>andesite</u> display positive trends of trace elements, with both pyrite types containing lattice-bound or evenly distributed nano-inclusions of Au, Ag and Bi (Fig. 7). The Co versus Ni binary plot portrays a positive correlation for Py2 (R_{Py2} = 0.75) and Py3 (R_{Py3} = 0.73) with increasing Co (up to 500 ppm), and Ni values (up to 1400 ppm) (Fig. 9D). The Py2 has higher As than Py3. On the other hand, two paths of Py3 in the Ni-As plot are indicated; one path has a relatively positive trend, the other with a continuous flat trend shows increasing Ni with consistent As concentrations (Fig. 9E).

7.3. Pyrrhotite and arsenopyrite LA-ICP-MS data

Lattice-bound or evenly distributed nano-inclusions elements: In BIF arsenopyrite and pyrrhotite, elements like Co, Ni, Bi, Mn, Pb and Au, form flat, and partly irregular LA-ICP-MS spectra profiles (Fig. A2). Cobalt, Ni, Pb form consistent spectra in both sulfide minerals that may be indicative of lattice substitutions in carbonaceous pelite.

Inclusion-related elements: Bismuth, Ag and Au form fluctuating, but not strong irregular profiles. These elements are interpreted to be present in the arsenopyrite lattice, and may form colloidal inclusions, which may be pervasive throughout the crystal or as discrete isolated inclusions in arsenopyrite of the BIF.

Cobalt-Ni and Ag-Pb bivariant plots of pyrrhotite and arsenopyrite types clearly demonstrate a separation into BIF- and carbonaceous pelite-related fields, except for the Bi-Pb plots, where the majority of arsenopyrite analyses of both host rocks display a distribution of Bi:Pb ratios between 0.1 and 1 (Fig. 10C, D).

7.4. Sulfur isotope data

A total of 293 SIMS sulfur isotope analyses ($\delta^{34}S$, $\Delta^{33}S$ and $\Delta^{36}S$) were conducted on syngenetic and hydrothermal pyrite and pyrrhotite from BIF, andesite and carbonaceous pelite taken from the FGS orebody (Fig. 2) at the Cuiabá mine (Tables 5, 6). Individual spots were selected based on previous backscattered images of pyrites and pyrrhotites, showing internal zoning (Fig. A3). The entire dataset of sulfur isotope analyses are listed in the Appendix Table A1. In-situ measurements of $\delta^{34}S$, $\Delta^{33}S$ and $\Delta^{36}S$ returned values for pyrites ranging between 1.78 to +6.90‰ $\delta^{34}S$, –2.28 to +1.73‰ $\Delta^{33}S$, and –2.04 and +3.19‰ $\Delta^{36}S$ (Fig. 13; Table 5). Pyrrhotite analyses range between –2.27 and +6.49‰ for $\delta^{34}S$, 0.68 and 1.90‰ for $\Delta^{33}S$, and –1.90 and +1.46‰ for $\Delta^{36}S$ (Table 6).

The multiple sulfur isotope data are subdivided according to different pyrite and pyrrhotite types (Fig. 5; Tables 5, 6). Fig. 11 shows two different patterns of sulfur isotope data. The first is a correlation between $\Delta^{33}S$ values and the amount of mass dependant fractionation (MDF) recorded by the ^{34}S-^{32}S ratios ($\delta^{34}S$ values). All data are outside the defined area of MDF, i.e., $\Delta^{33}S$ ranging from –0.2 to +0.2‰ (Farquhar and Wing, 2003) (Fig. 11). The second pattern demonstrates the correlation between $\Delta^{33}S$-$\Delta^{36}S$ data of all pyrite types. The $\Delta^{36}S$/$\Delta^{33}S$ ratio differentiates mass-dependent processes and contributions from Archean MIF sources when magnitudes of mass-dependent fractionation deviations are small (Farquhar et al., 2007; Johnston, 2011). The typical Archean array indicated by Johnston (2011) and Zerkle et al. (2012) is –0.9, whereas our data point to a $\Delta^{36}S$-$\Delta^{33}S$ array of –0.5 (Fig. 11).

The Py1, only analyzed in the carbonaceous pelite, yields $\delta^{34}S$ values ranging from 1.78 to 5.69‰ (median 2.82‰), $\Delta^{33}S$ ranging from –2.28 to –0.25‰ (median –1.46‰), and $\Delta^{36}S$ between 0.77 and 3.19‰ (median 2.11‰) (Table 5, Fig. 11). The $\Delta^{33}S$ signatures for this pyrite may be subdivided in two groups: from –2.28 to –1.97‰, and –0.96 to –0.25‰ (Fig. 11).
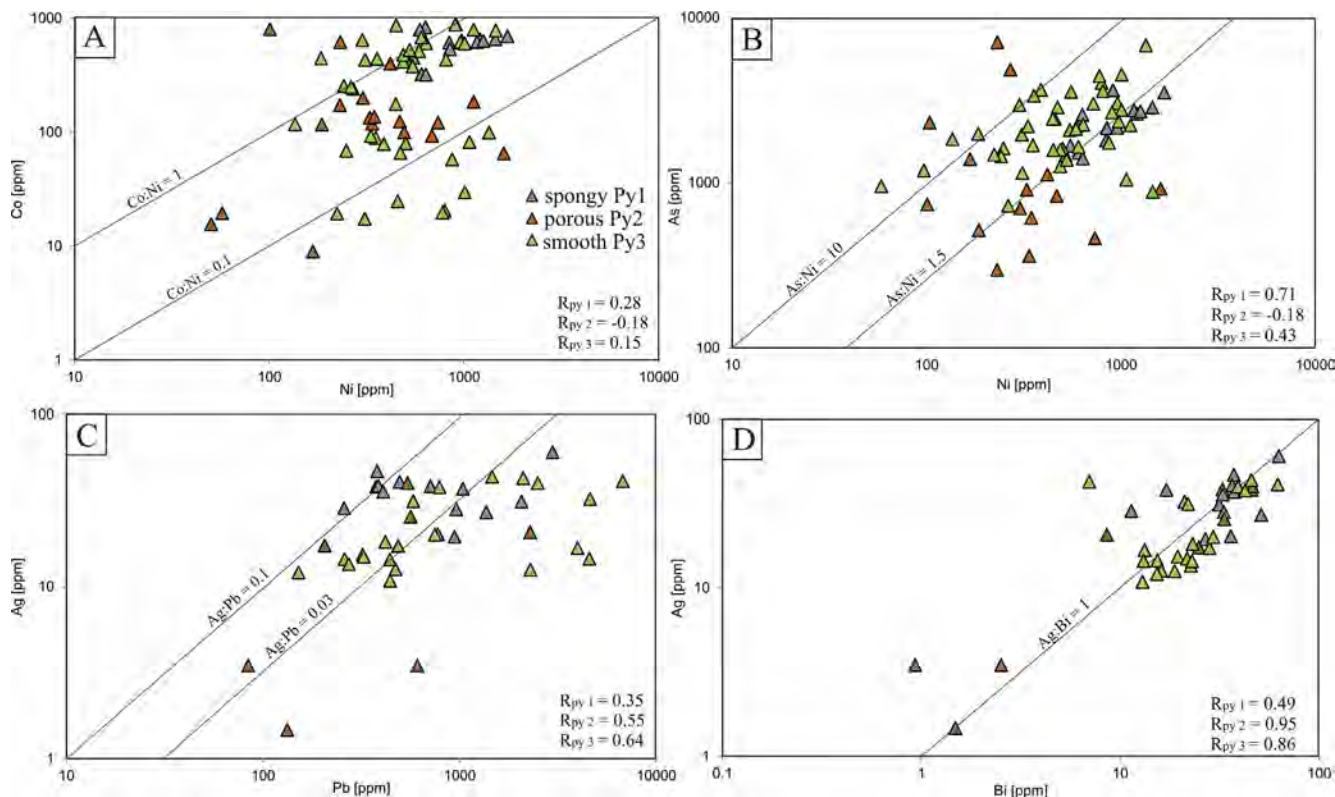
Fig. 8. Trace element spot analyses on pyrite types in the carbonaceous pelite. R_{Py} represent correlation coefficients for each pyrite type.

The Py2 of carbonaceous pelite has $\delta^{34}S$ values from 3.01 to 5.79‰ (median 4.16‰), $\Delta^{33}S$ ranging from 0.28 to 1.07‰, and $\Delta^{36}S$ between –0.80 to +2.22‰. The Py2 of andesite and BIF have similar $\delta^{34}S$ and $\Delta^{33}S$ signatures ($\delta^{34}S$ = 3.57 to 6.86‰ and 3.20 to 6.09‰; $\Delta^{33}S$ = 0.57 to 0.79 and 0.64‰ to 1.44‰, respectively). The $\Delta^{36}S$ values of both host rocks are slightly more negative (Fig. 11).

The Py3 of all host rocks has $\delta^{34}S$, $\Delta^{33}S$ and $\Delta^{36}S$ ranges that are similar to those of the Py2, with values between 3.85 and 6.90‰ $\delta^{34}S$, 0.37 to 1.73‰ $\Delta^{33}S$, and –2.04 to +1.68‰ $\Delta^{36}S$ (Table 5, Fig. 11).

Both Py4 and Py5 in BIF yield more constrained $\delta^{34}S$, $\Delta^{33}S$ and $\Delta^{36}S$ values (Table 5). The $\delta^{34}S$ values range from 4.90 to 6.53‰ (median 5.93‰), $\Delta^{33}S$ from 0.77 to 1.11‰ (median 0.98‰), and $\Delta^{36}S$ from –1.38 to +0.42‰ (median –0.75‰). The $\delta^{34}S$ and $\Delta^{33}S$ values of Py5 are even more positive in the order of 5.19 to 6.94‰ (median 6.38‰)

$\delta^{34}S$, and from 0.96 to 1.14‰ (median 1.06‰) $\Delta^{33}S$. The $\Delta^{36}S$ values range from –1.32 to –0.04‰ (median –0.70‰).

Pyrrhotite sulfur isotope data are subdivided due to their paragenetic stage (Fig. 5). Early-stage Po1 of the BIF has $\delta^{34}S$ from 1.53 to 5.76‰ (median 4.98‰), $\Delta^{33}S$ from 0.68 to 1.15‰ (median 0.93‰), and $\Delta^{36}S$ from –0.90 to +2.30‰ (median 0.45‰) (Table 6). Early-stage Po3 of carbonaceous pelite yields $\delta^{34}S$ from 4.75 to 5.80‰ (median 5.50‰), $\Delta^{33}S$ from 1.02 to 1.42‰ (median 1.11‰), and $\Delta^{36}S$ from –0.62 to +1.46‰ (median –0.05‰) (Table 6). Late-stage Po2 of BIF-hosted quartz-pyrrhotite veins indicates $\delta^{34}S$ values ranging from 4.91 to 5.19‰ (median 5.01‰), $\Delta^{33}S$ from 1.05 to 1.25‰ (median 1.14‰), and $\Delta^{36}S$ from –1.84 to –0.85‰ (median –1.35‰) (Table 6). Late stage Po4 of carbonaceous pelite yields slightly more positive $\delta^{34}S$ (5.02 to 6.49‰), and $\Delta^{33}S$ values (1.58 to 1.90‰). The $\Delta^{36}S$ values are
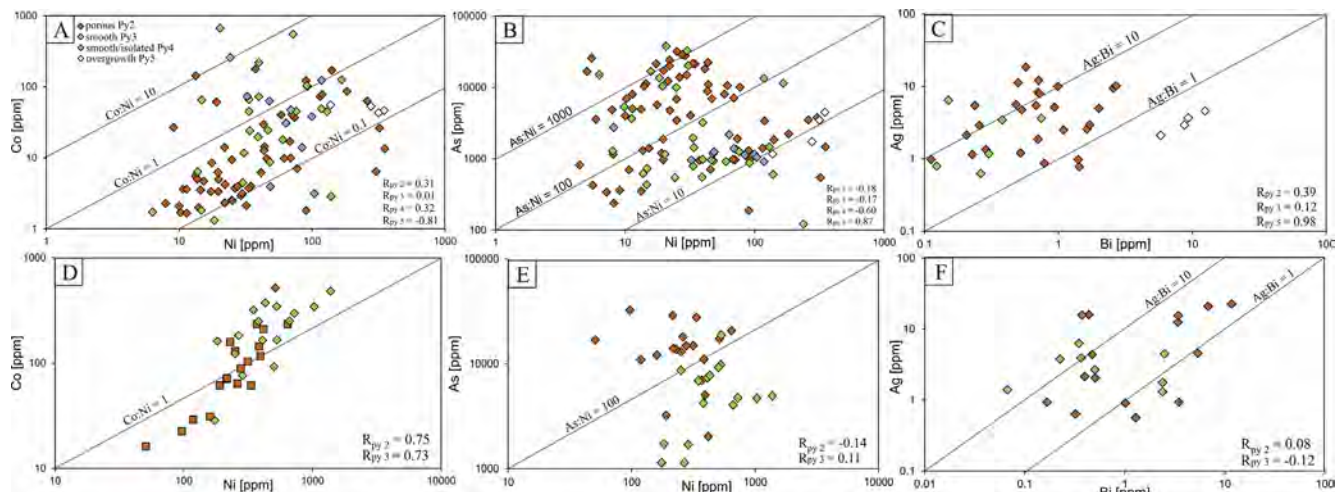

Fig. 9. Trace element spot analyses on pyrite types in the BIF (A-C) and andesite (D-F). R_{Py} represent correlation coefficients for each pyrite type.
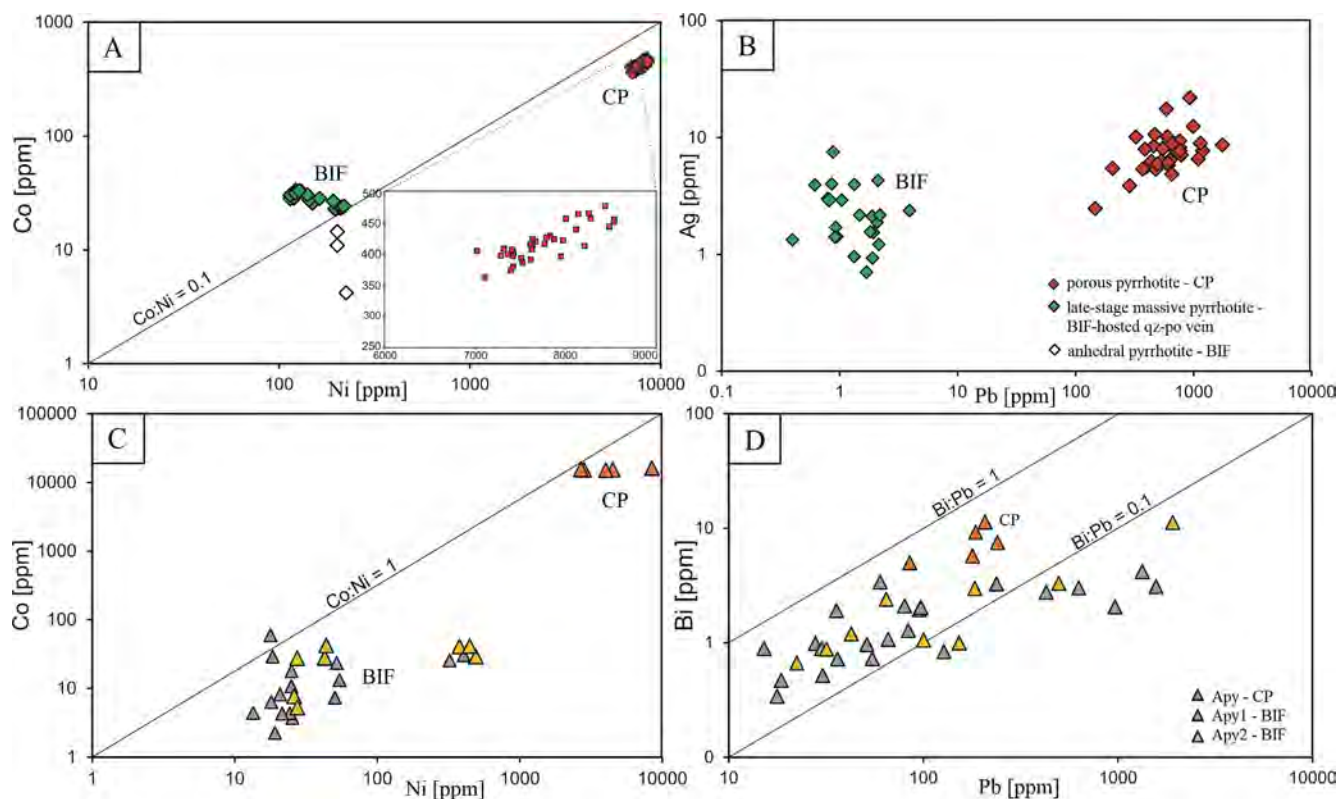
Fig. 10. Trace element spot analyses on pyrrhotite (Po) (A/B) and arsenopyrite (Apy) (C/D) in BIF and carbonaceous pelite (CP). Qz = Quartz.
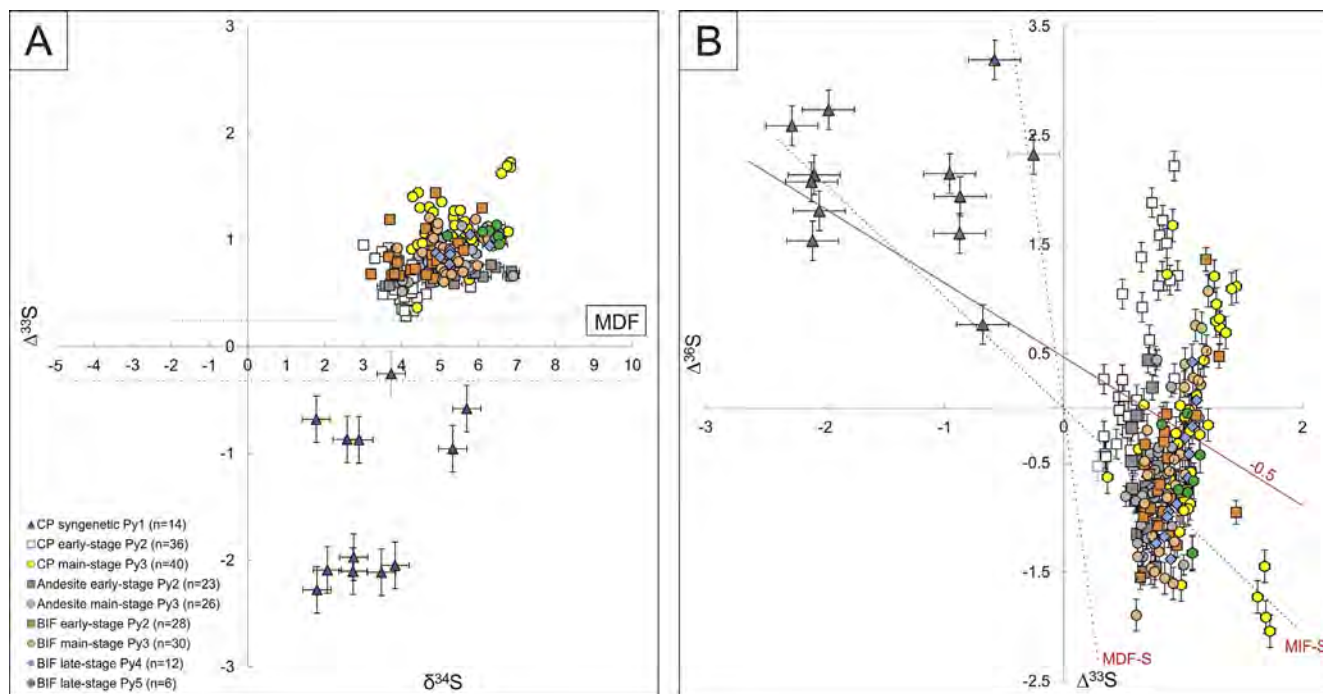
Fig. 11. Bivariate plots of multiple sulfur isotope data on pyrite types in the Cuiabá deposit. Data are grouped according to pyrites (Py1 to Py5) and host rocks BIF, carbonaceous pelite (CP) and andesite. Number of analyses are shown in caption box. δ34S versus Δ33S (A). Δ36S-Δ33S data array. Stippled line: MDF-S between −9 and −7 by Wacey et al. (2015). Dashed line: MIFS Δ36S-Δ33S ≈ −0.9, Archean array by Johnston (2011) and Zerkle et al. (2012). Solid line: −0.5, present study (see text) (B). The δ34S, Δ33S and Δ36S error bars (2σ) are graphically represented in both directions. MDF and MIF = mass dependent and independent fractionation.

Table 5
Statistical summary (comprising minimum, mean, median and maximum) of δ34S, Δ33S and Δ36S values for pyrite types in carbonaceous pelite, BIF and andesite. Py1 only in carbonaceous pelite; Py2 and Py3 in all host rocks. Py4 and Py5 only in BIF.

	Syngenetic Py1 (n = 14)			Early-stage Py2 (n = 91)			Main-stage Py3 (n = 96)			Late-stage Py4 BIF (n = 12)			Late-stage Py5 BIF (n = 7)		
	δ34S	Δ33S	Δ36S	δ34S	Δ33S	Δ36S	δ34S	Δ33S	Δ36S	δ34S	Δ33S	Δ36S	δ34S	Δ33S	Δ36S
Min	1.78	-2.28	0.77	3.01	0.28	-2.00	3.85	0.37	-2.04	4.90	0.77	-1.38	5.19	0.96	-1.32
Mean	3.22	-1.40	2.07	4.60	0.73	-0.22	5.31	0.95	-0.46	5.79	0.97	-0.63	6.19	1.06	-0.66
Median	2.82	-1.46	2.11	4.62	0.71	-0.42	5.26	0.93	-0.60	5.93	0.98	-0.75	6.38	1.06	-0.70
Max	5.69	-0.25	3.19	6.86	1.44	2.22	6.90	1.73	1.68	6.53	1.11	0.42	6.54	1.14	-0.04

similar to late-stage, massive pyrrhotite of BIF-hosted quartz-pyrrhotite veins (Table 6).

8. Discussion

When comparing the trace element distribution for carbonaceous pelite, BIF and mafic rocks (Figs. 8, 9), it is clear that a different pattern arises for the former in comparison to the two latter rock types. The trace element distribution of carbonaceous pelite (Fig. 8) is somewhat constrained between Co/Ni ratios 0.1 and 1, suggesting an inheritance from the host rock geochemical behavior, with this lithotype being the only one where a syngenetic pyrite (Py1) is identified. On the other hand, the large scatter of points in Fig. 9, widely distributed in all plots, may be interpreted as a geochemical behavior dominantly resulting from the hydrothermal fluid.

8.1. Co/Ni ratio versus Bi, Ag and Au

Recent studies by Large et al. (2014) and Gregory et al. (2015a,b) invoke Co/Ni ratios to determine the origin of pyrites in carbonaceous pelite. Bajwah et al. (1987, and references therein) consider that hydrothermal pyrite commonly contains > 400 ppm Co, with a Co/Ni ratio > 1, whereas syngenetic pyrite has < 100 ppm Co, and a Co/Ni ratio < 1. According to Large et al. (2014) and Gregory et al. (2015a), the Co/Ni ratio of the majority of pyrite formed from hydrothermal fluids is > 2, with only submarine exhalative and orogenic gold deposits having pyrites with lower ratios. The presence of pyrrhotite also influences Co/Ni ratios, and therefore metamorphism of rocks from mesozonal orogenic gold deposits may shift pyrite compositions into the VHMS field (Co/Ni > 1; Belousov et al., 2016). According to Belousov et al. (2016), Co/Ni ratios may well distinguish between mineral systems, e.g. VHMS and orogenic gold deposits, with most pyrites of orogenic gold deposits having Co/Ni < 1, and 94% with Co/Ni ratios < 10. This relates to Co being more soluble than Ni in moderate to high temperature saline fluids typical of VHMS ore deposits, whereby mesozonal orogenic gold deposits associated with greenstone belts are generally characterized by low to moderate salinity (5–10 wt% NaCl equiv), and low to moderate temperature hydrothermal fluids (Ridley and Diamond, 2000).

In the case of Cuiabá, calculated Co/Ni ratios of carbonaceous pelite Py1 trend towards Co/Ni = 1 line (Fig. 8). The values for Py2 and Py3 are more variable, but some Py2 have Co/Ni ratios > 1 (up to 2.6 and 7.9), coinciding with ratios < 1 for Py1. Furthermore, relatively

reducing fluid conditions indicated for the Cuiabá deposit (Lobato et al., 2001a,b), have also been invoked to help enhance the uptake of Ni into pyrite (Maslennikov et al., 2009; Scott et al., 2009; Guy et al., 2010). Besides the interpreted Co/Ni ratio, there is a difference regarding Bi values of pyrites with respect to each host rock analyzed. For andesite (Fig. 9), Co/Ni ratios are consistent, remaining flat with respect to increasing Bi values (Co/Ni ratio > 1) (Fig. 12A). On the contrary, for carbonaceous pelite there is a completely separate population with predominantly higher Co/Ni ratios (Co/Ni = 1) and high Bi concentrations (up to 65 ppm). As for the BIF, the Co/Ni ratio versus Bi shows mostly a positive correlation for Py2, Py3 and Py4, with Py5 forming one separate population (Fig. 12A). Most of the Co/Ni ratios are < 1, and Bi ranges between 0.1 and 1. Fig. 12B depicts the relation between Co/Ni ratio and Ag, which shows a similar behavior for all pyrite types in the three host rocks. The Co/Ni ratio and Au in pyrites hosted in andesite (Fig. 12B) show the same pattern as observed in the Co/Ni-Bi and Co/Ni-Ag plots. In contrast, the BIF indicates a completely different manner in a constrained range of Co/Ni ratios between 0.1 and 1. However, both host rocks display a constant Co/Ni ratio, but variable Au concentrations.

Higher Bi concentrations are most likely interpreted as Bi-Au-(Pb)-bearing telluride inclusions in pyrite and as incooporations in galena. Bismuth enrichment may also be explained by changes in provenance of the sediments, which can also affect the availably of certain elements. For example, mafic elements like Ni, Co and Cu would have been available in shale basins, where sediments are sourced from a mafic igneous terrane. In contrast, sediment sourced from a felsic igneous terrane would provide more felsic elements (e.g., Mo, Bi) (Gregory et al., 2015a). According to Tribovillard et al. (2006), Ni, Cu, and Zn are associated with rates of organic carbon sinking flux, which is frequently associated with its productivity. Those trace elements adsorb onto organic matter and are incorporated into the sediments. Once the organic matter breaks down, the trace elements are left behind, and some are incorporated into pyrite (Gregory et al., 2015a). Furthermore, Bi and Au may be more easily accumulated into the pyrite lattice if As is present and substituted into the Fe site of this sulfide mineral. Arsenic has the ability to distort the pyrite lattice, making it easier for large cations to be incorporated in the pyrite, and at higher concentrations (Reich et al., 2005; Deditius et al., 2014). Bismuth enrichment and the presence of Bi-bearing inclusions may suggest the contribution of felsic magmatic hydrothermal fluids, or the leaching of granitoid rocks during fluid transport from the source to the depositional site (based on the association of Bi and Sn with felsic magmatic rocks) (Gregory et al.,

Table 6
Statistical summary (comprising minimum, mean, median and maximum) of δ34S, Δ33S and Δ36S values for pyrrhotite paragenetic stages and host rocks.

	Late-stage qz-po vein (n = 7)			Early-stage anhedral po BIF (n = 45)			Early-stage anhedral po CP (n = 11)			Late-stage porous po CP (n = 10)		
	δ34S	Δ33S	Δ36S	δ34S	Δ33S	Δ36S	δ34S	Δ33S	Δ36S	δ34S	Δ33S	Δ36S
Min	4.91	1.05	-1.84	1.53	0.68	-0.90	4.75	1.02	-0.62	5.02	1.58	-1.90
Mean	5.04	1.15	-1.40	4.40	0.91	0.37	5.43	1.13	0.09	6.19	1.80	-1.17
Median	5.01	1.14	-1.35	4.98	0.93	0.45	5.50	1.11	-0.05	6.30	1.81	-1.13
Max	5.19	1.25	-0.85	5.76	1.15	2.30	5.80	1.42	1.46	6.49	1.90	-0.56
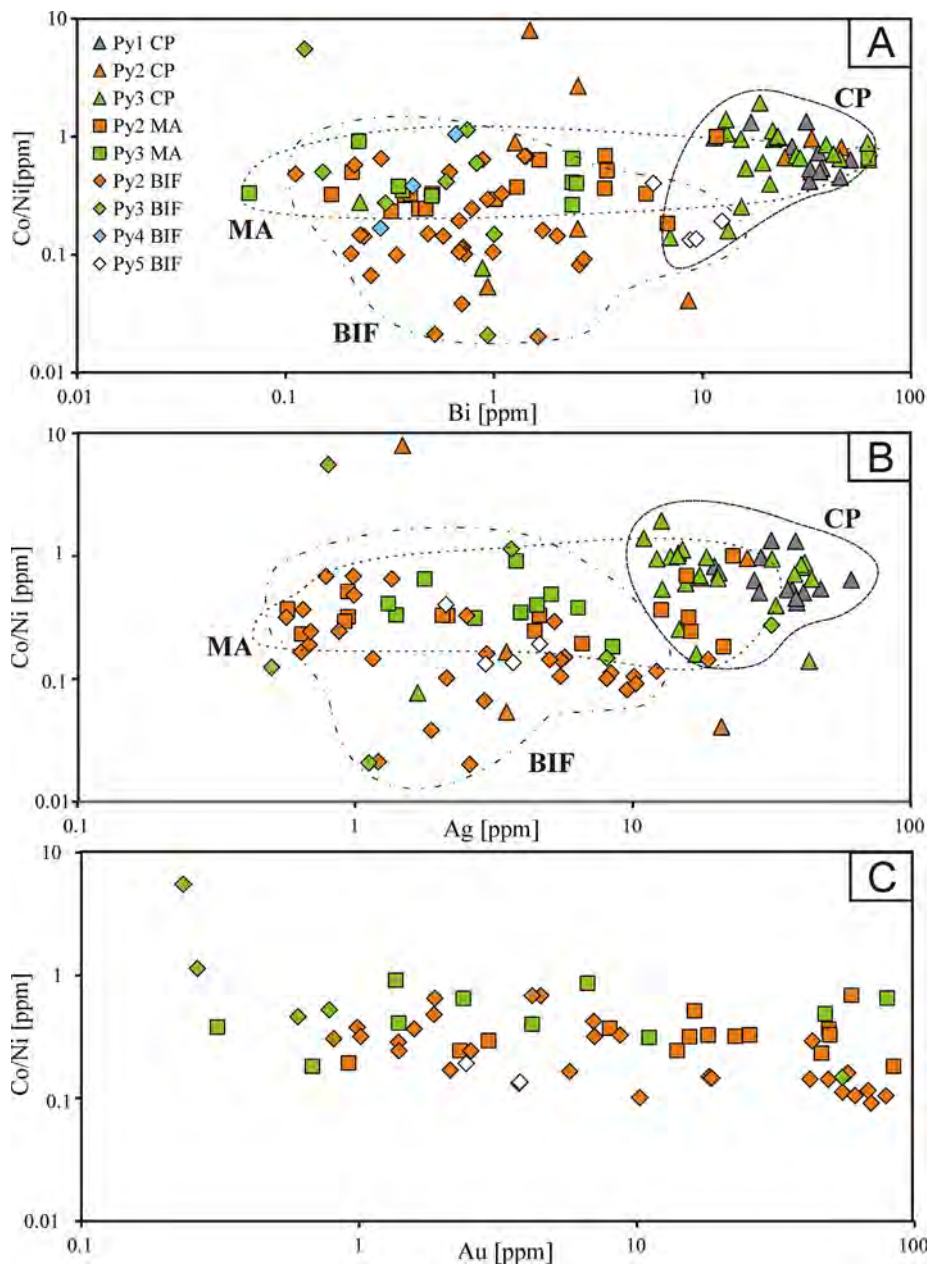
Fig. 12. Co/Ni ratio versus Bi (A), Ag (B) and Au (C) of pyrite types (Py) for each host rock under study, indicating significant trends for each one of them. Dotted line = andesite (MA), dashed line = carbonaceous pelite (CP), dashed-dotted line = BIF.

2015a). The Cuiabá deposit is situated within a granite-greenstone belt, and it is likely that some metals were leached from underlying intrusion domes.

It is thus reasonable to assume that at Cuiabá Co/Ni ratios mainly > 1 registered in all pyrite types arising from reducing fluid conditions, which helped enhance the uptake of Ni into pyrite. The relations between Co/Ni ratio and Au as well as Ag concentrations are characteristic for each host rock. While BIF and andesite show relatively dispersed patterns, the carbonaceous pelite fields (Bi and Ag) (Fig. 12A, B) are more restricted.

8.2. Significance of trace element data of pyrite, pyrrhotite and arsenopyrite

Pyrite: The relation between pyrite types and trace element distribution is complex, and is initially considered separately for carbonaceous pelite, andesite and BIF. All the same, porous Py2 and smooth Py3 are similar in their habit in all host rocks, and for this reason should

allow the comparison of their trace element incorporation.

The Py1 shows a distinct geochemical signature when compared to Py2 and Py3 in carbonaceous pelite (Fig. A4, top diagram). The restricted range and high concentration of Co, Ni, As and Ag in Py1 may be indicative of its syngenetic origin, whereas those of Py2 and Py3 imply a hydrothermal character with their variable trace element distribution (Fig. A4). These elements may be concentrated originally by organic processes during sedimentation and diagenesis of organic-rich sediments in an euxinic environments. Arsenic, Ni, Ag and Au (the latter not detected in this study) could be released from organic matter and concentrated in Py1. As Py2 is formed after Py1, these elements and some Au may have been released to the hydrothermal fluid (cf. Large et al., 2011). Laser ICP-MS studies on sedimentary pyrites from the late Archaean Hamersley basin by Gregory et al. (2015b) result in median As/Ni ratios between 0.1 and 10. Most of the syngenetic to late diagenetic pyrite types of the carbonaceous pelite at Cuiabá have As/Ni ratios within this range (Fig. 8). In contrast, with a few exceptions the
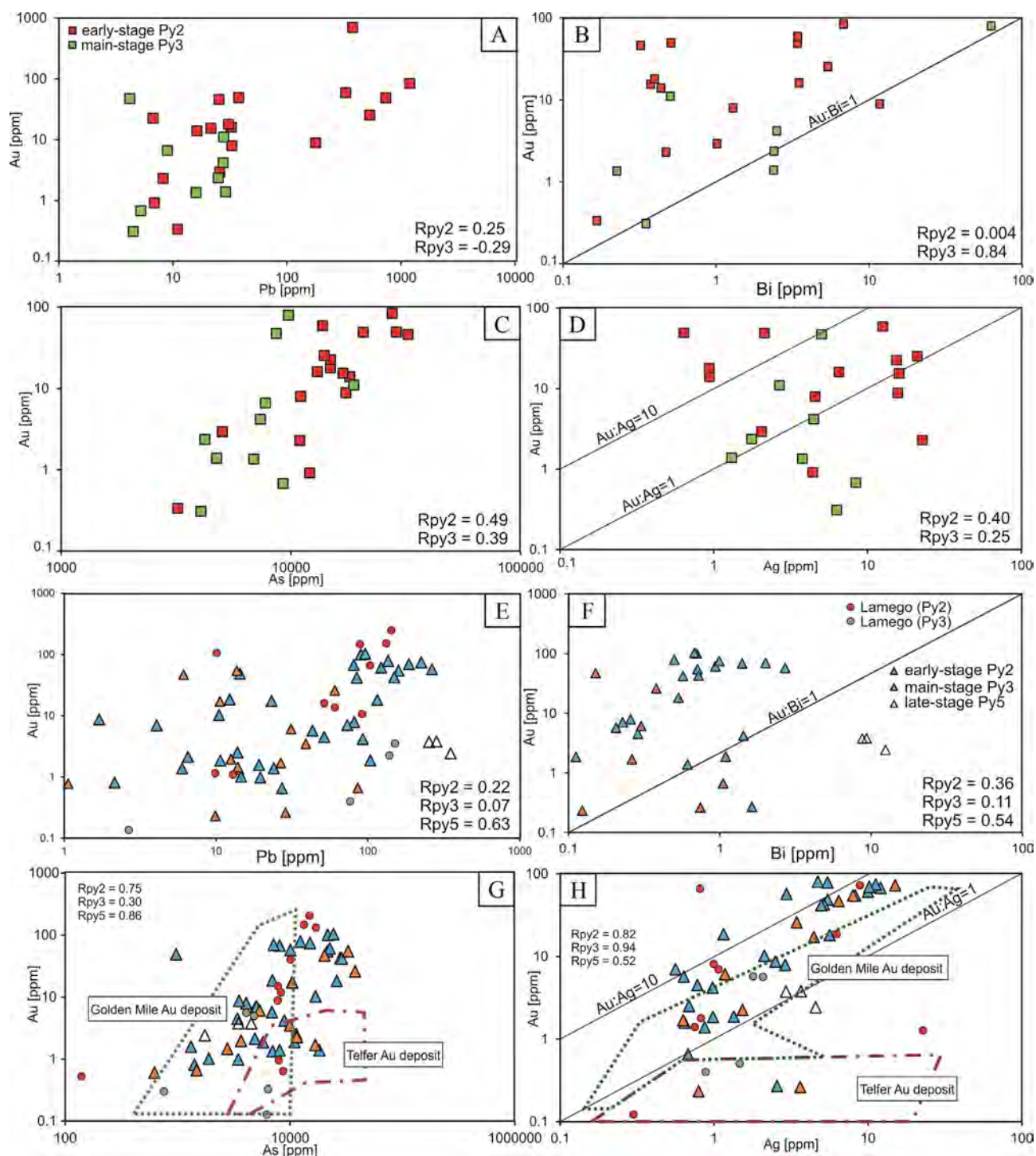
Fig. 13. Andesite plots of pyrite spot analyses of the Cuiabá deposit (A–D). BIF plots of pyrite spot analyses of Cuiabá are compared with other orogenic gold deposits (E–H). Au-Pb plot (A). Au-Bi plot (B). Au-As plot (C). Au-Ag plot (D). Au-Pb plot (E). Au-Bi plot (F). Au-As plot (G). Au-Ag plot (H). Reference data of other gold deposits. Sulfide-rich BIF-hosted pyrite - Lamego orogenic Au deposit (Martins, 2016,); black-shale hosted pyrite - Golden Mile Au deposit (Steadman et al., 2015; Steadman and Large, 2016); metasediment-hosted pyrite - Intrusion-related Telfer Cu-Au deposit. R$_{Py}$ represent correlation coefficients for each pyrite type.

majority of As/Ni ratios of BIF- and andesite-hosted pyrite types are > 10, suggesting that these elemental variations were much more influenced by the hydrothermal fluid in the case of both these host rocks, than in carbonaceous pelite.

Figure A4 demonstrates that the average As concentrations are consistent throughout pyrite types, assuming similar paragenetic stages for Py2 and Py3 in all host rocks. However, if the host rocks are separately considered, As concentrations vary among them (Table 2). An

increase of As, Bi and Pb from Py2 to Py3 in carbonaceous pelite is likely to suggests their release from the hydrothermal fluid, and incorporation into Py3. Andesite and BIF display a reverse trend of As, Bi and Pb between Py2 and Py3, showing depletion of Bi, Pb and As from Py2 to Py3 (Table 2). It is noteworthy that whereas arsenopyrite (Apy1 and Apy2) is a significant phase in BIF, and minor in carbonaceous pelite, it is absent in andesite where arsenian pyrite is present (Fig. 5). The development of significantly more Apy1 and Apy2 in BIF, and

arsenian pyrite in andesite compared to arsenopyrite in carbonaceous pelite, may explain the variability in the As behavior (Fig. A4), and the related incorporation of As, Bi and Pb in arsenopyrite.

The binary plots displayed in Fig. 13 show that Au correlates well with elements of crustal affinity, such as Bi and Pb. However, Au and As in Py2 and Py3 in andesite and BIF are clearly correlated supporting their hydrothermal origin. Late-stage Py4 and Py5 in BIF display a different geochemical pattern (Fig. A4). The Py4 shows lower trace element concentrations when compared to Py3, whereas Py5 exhibits further enrichment in Co, Ni and Bi relative to all other pyrite types, as well as Au concentrations of up to 2 ppm (Fig. A4).

Pyrrhotite: The trace element distribution in pyrrhotite (Fig. 10A, B) differs completely from pyrite in terms of host rock and paragenetic stage (Fig. 5). Although anhedral pyrrhotite in carbonaceous pelite reveals Co concentrations below detection limits and Ni enrichment of up to 1900 ppm, porous pyrrhotite in the same host rock is highly enriched in both Co (~500 ppm) and Ni (~9000 ppm). Anhedral pyrrhotite represents the earliest formed hydrothermal sulfide (Fig. 5A, C); in contrast, porous pyrrhotite is interpreted to have formed at an advanced stage (Fig. 5I). In comparison, anhedral pyrrhotite in BIF is approximately 100 times less enriched in Co, Ni and Pb. This seems to indicate that the carbonaceous pelite was relatively rich in Ni, allowing for the progressive fixation of this metal in pyrrhotite as this sulfide mineral developed.

Since As is high (mean value 441 ppm) in BIF pyrrhotite, but not detected in either anhedral or porous pyrrhotite of carbonaceous pelite, it may be related to the formation of arsenopyrite at an earlier stage in the BIF compared to its stage of development in carbonaceous pelite (Fig. 4). Given that pyrrhotite does not hold gold or arsenic in its structure (Large et al. (2011, and references therein), conversion of Au-bearing diagenetic pyrite to pyrrhotite during greenschist and amphibolite facies metamorphism releases invisible gold and arsenic into the fluid. As a result Au-As-bearing ores in proximal or distal zones of orogenic gold deposits are common (e.g., Buryak, 1982; Pitcairn et al., 2006; Large et al., 2007; Tomkins, 2013).

Increasing Pb concentration from 150 ppm to 1700 ppm with somewhat higher Ag in porous pyrrhotite of carbonaceous pelite implies primary low Pb concentrations, and also late-stage hydrothermal enrichment (Fig. 10B). In contrast, hydrothermally concentrated Ag is similar to BIF pyrrhotite. Syngenetic arsenian pyrite may be converted into pyrrhotite under greenschist facies conditions in carbonaceous pelite (Large et al., 2011), and similarly to Au certain elements such as Bi, Pb, S and As as already mentioned are released into the fluid. The elevated Pb and Bi in late-stage porous pyrrhotite of Cuiabá may be indicative of this conversion (Table 3).

As indicated in Fig. 10, showing early- and late-stage pyrrhotite types, in the case of Cuiabá Co, Ni, Ag, Pb and Bi may also have been released to/from the hydrothermal fluid, respectivley.

Arsenopyrite: Similar geochemical patterns are shown for arsenopyrite analyses (Fig. 10 C, D), which also indicate completely different trace element patterns in BIF and carbonaceous pelite. For example: (1) Apy in carbonaceous pelite has low Co (16 ppm) and Ni (5 ppm) concentrations; (2) Apy1 in BIF shows low Co (16 ppm) and low Ni (50 ppm); and (3) Apy2 in BIF has elevated Co (28 ppm) and Ni (154 ppm), but lower As (up to 28 ppm) and Au (3 ppm) (Fig. 10). Cobalt and Ni were probably present in the original carbonaceous pelite, but both were hydrothermally enriched in the BIF as well as later in carbonaceous pelite. Also noticeable are significantly higher Au concentrations in BIF Apy1 (up to 53 ppm) in comparison to its Apy2. The Apy1 of BIF is interpreted to be part of an early hydrothermal stage that is linked to gold mineralization (Fig. 4). The Apy2 (Fig. 4), in contrast, is interpreted to have formed during a late hydrothermal stage with significant Co and Ni enrichments, but As depletion.

8.3. Pyrite-related Au mineralization at Cuiabá

Fig. 13 shows the correlation of Au and certain trace elements like Pb, Bi, As and Ag. Gold and Pb correlate positively with Py2 and Py3 in andesite (R_{Py2} = 0.25, R_{Py3} = −0.29), with a decreasing trend from early-stage Py2 to main-stage Py3 (Fig. 13A). The Au-Bi plot of andesite-bearing Py2 and Py3 shows that the majority of both pyrite types have Au/Bi ratios > 1. The best correspondence displays Au and As with a steep positive correlation between andesite Py2 (R_{Py2} = 0.49) and Py3 (R_{Py3} = 0.39). The majority of Py2 analyses plot at high As and Au values, with a decreasing tendency from early-stage Py2 to main-stage Py3 (Fig. 13C). The Au vs Ag binary plot shows no correlation for andesite pyrite (Fig. 13D).

For BIF (Fig. 13E–H), Au and Pb correlate positively in Py2 (R_{Py2} = 0.22); at the highest Pb and intermediate Au field, Py5 defines one specific population (unfilled triangles), whereas the Py3 data are scattered (R_{Py3} = 0.07) (Fig. 13E). Both Py2 and Py3 show a weak positive correlation of Au and Bi with most of them having an Au/Bi ratio > 1 (R_{Py2} = 0.36, R_{Py3} = 0.11). The Py5 is clearly separated from Py2 and Py3 with Au/Bi ratio of < 1. The Au and As binary plot of the BIF indicates a positive correlation for Py2 (R_{Py2} = 0.75), Py3 (R_{Py3} = 0.30) and Py5 (R_{Py5} = 0.86), showing a decrease from early-/main-stage Py2 and Py3 to late stage Py5 (Fig. 13G). Both Py2 and Py3 indicate a positive correlation of Au and Ag in BIF (R_{Py2} = 0.82, R_{Py3} = 0.94). The outliers for Py3 may represent gold and-or silver inclusions (Fig. 13H).

Compared to other orogenic gold deposits like the nearby QF BIF-hosted Lamego deposit, the mafic rock-hosted Golden Mile (Steadman and Large, 2016), and metasedimentary-hosted Telfer deposits in Australia (Schindler et al., 2016), a similar correlation pattern is illustrated (Fig. 13D, E, F), although it is noticeable that the Cuiabá and Lamego data are slightly different. For example, both QF deposits yield partly higher Au:Ag ratios independent of pyrite type, and some higher As values are related to higher Au concentrations. There is a strong Au-As correlation with decreasing Au and As concentration from early-stage Py2 to main-stage Py3 in andesite, and from Py2, Py3 to Py5 in the BIF (Fig. 13E, F). This probably reflects Au released from Py1 in carbonaceous pelite, or organic matter. Alternatively thus may represent Au directly precipitated from hydrothermal fluid during shear zone activity (Cook et al., 2009; Large et al., 2011).

Reich et al. (2005) demonstrated that the maximum possible gold amount in solid solution in pyrite depends on the As content of this sulfide mineral. The As-Au relationship in pyrite has proven to be useful for distinguishing between the refractory and free gold ores (e.g., Large et al., 2007, 2009, 2011; Thomas et al., 2011). A comparison study of VHMS and orogenic gold deposits by Belousov et al. (2016) shows that most of the Au-As associated orogenic gold deposits, with high Au and As contents in pyrite, have the majority of their Au in refractory form. The São Bento orogenic gold deposit in the QF, where Au is mainly associated with arsenopyrite, shows the same refractory nature for Au (Pereira et al., 2007). A few examples in the Yilgarn craton such as St. Ives, Kanowna Belle, Lancefield and Youanmi, as well as deposits in the Au-As-Te association (e.g. Golden Mile and Chalice), also have significant amounts of Au as inclusions (Belousov et al., 2016). Those pyrites from Au-As ores have Pb/Bi > 5 (Belousov et al., 2016), which is in accordance with the Cuiabá Pb/Bi ratios ranging between 9 and 70 for andesite pyrite, and between 29 and 300 for BIF pyrite.

In Fig. 14, LA-ICP-MS spot analyses of pyrite (Table 2), which plot above the maximum saturation line (yellow field) contain free gold inclusions (one analysis point), whereas analyses plotting below the line contain refractory gold in pyrite. Lattice-bound or evenly distributed nano-inclusions, and inclusion-related analyses are differentiated based on LA-ICP-MS spectra, in order to plot the data of Fig. 14 (see section on Materials and Methods). The Cuiabá data (Fig. 14) suggest that the maximum Au solubility line might be lower for pyrites in BIF and in andesite than previously determined by Reich et al.
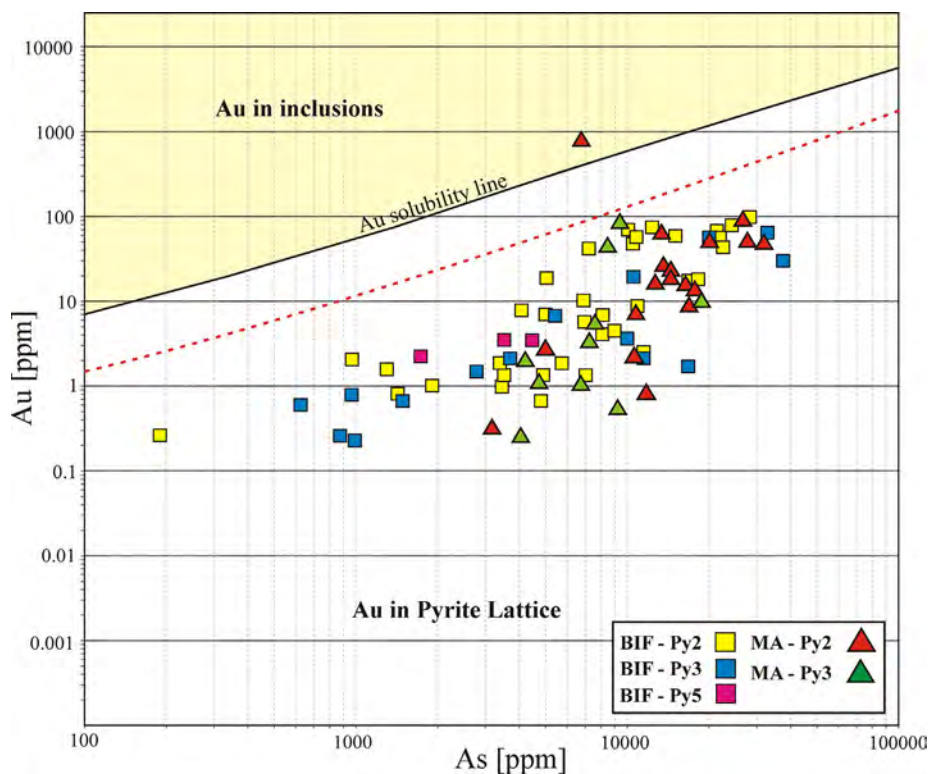
Fig. 14. Au-As solubility plot for pyrite types (Py) from the Cuiabá orogenic gold deposit with the Au-As solubility line for pyrites described in Reich et al. (2005), and modified (red stippled line) with regard to the Cuiabá pyrite data. MA = andesite. (For interpretation of the references to color in this figure legend, the reader is referred to the web version of this article.)
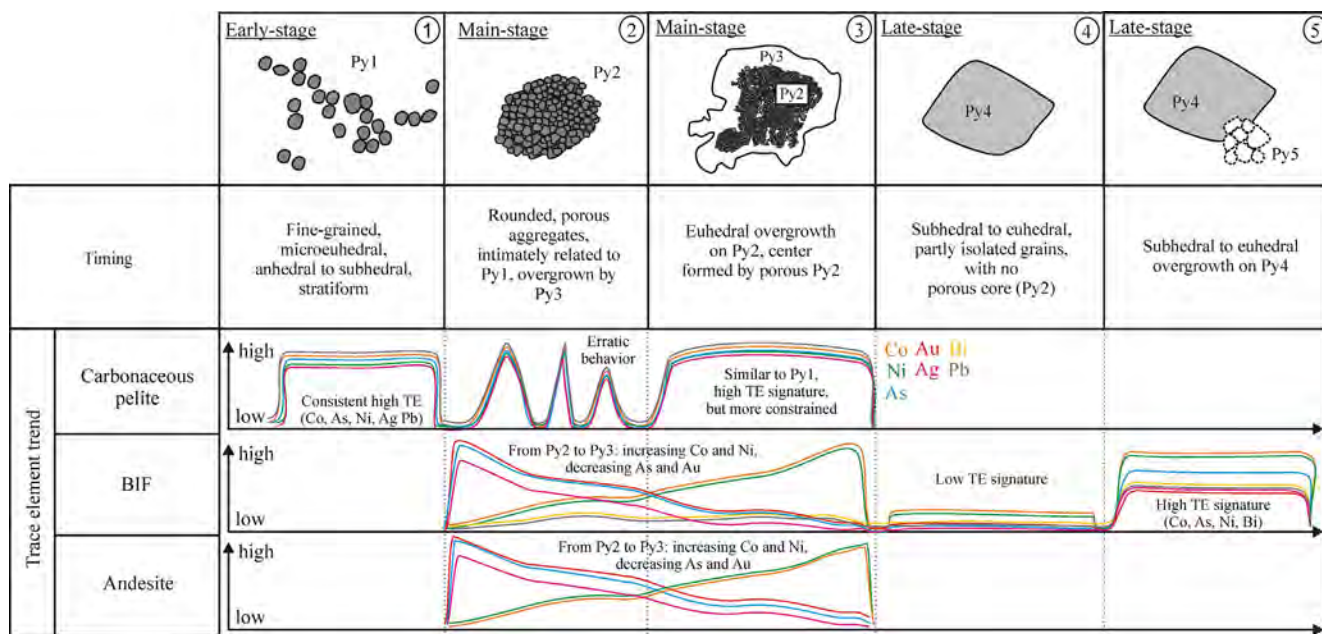
Fig. 15. Sketch of five-stage pyrite (Py) evolution, taking into account timing evidence and trace element (TE) trends of pyrite types. Py1 only observed in carbonaceous pelite. Late-stage Py4/Py5 only observed in BIF.

(2005), implying that more Au forms inclusions rather than stays in the pyrite structure. A simpler explanation might be that at Cuiabá the fluid had lower gold content, and that most of the Au was present in native form. Assuming that all native gold was precipitating at the same time, less gold would be available to form as inclusions in pyrite.

8.4. Pyrite evolution at the Cuiabá deposit

By combining paragenetic evidence of timing and geochemical trends of trace elements in the different pyrite types in carbonaceous pelite, BIF and andesite, a five-stage evolution is proposed (Fig. 15). From Fig. 15 it is clear that geochemical and petrographic overlaps are reasonable between evolving pyrites types. Parallel to this, the individual paragenetic stages of pyrite, pyrrhotite and arsenopyrite are compared to trace possible relations.

Carbonaceous pelite has a syngenetic, spongy Py1 that is characterized by consistent high trace elements (As, Co, Ni, Pb, and Ag), which results in Py2 forming due to the aggregation of Py1. Although Py2 partly inherited the geochemical features of Py1 (Figs. 8, A4), it shows an irregular distribution pattern, and generally lower values

(also a decreasing signature) in trace element distribution. Therefore, this second type Py2 is interpreted to be i) late diagenetic based on the assumption that Py2 is made up by the accumulation of Py1 through pressure, and resulted in its porous nature, and-or ii) early hydrothermal based on its irregular trace element concentration, indicating an inherited, as well as hydrothermal fluid signature, correlated to its main gold and As enrichment (Fig. 15). The rather irregular distribution pattern acquired by Py2 may have resulted from somewhat unbuffered conditions that must have prevailed during these relatively early hydrothermal alteration stages.

Banded iron formation and andesite have average Au concentrations that are significantly higher in Py2 than in Py3. Interestingly, the geochemical signature of Py3 in pelite is somewhat similar to that of Py1, with data distribution better constrained, forming data population (Fig. 8) that is better defined than that of Py2. This may be interpreted as evidence for Py3 having equilibrated from a higher fluid-rock ratio during its formation, and after buffering was achieved (Fig. 15), and probably marks the main hydrothermal stage. The Py3 in BIF and andesite evolved from a fluid rich in trace elements acquired from earlier sulfide phases, or inherited in the fluid, but under better buffered conditions between host rock and fluid.

Cobalt and Ni increase from Py2 to Py3, whereas As and Au decrease from Py2 to Py3 in andesite and BIF. It is likely that Co and Ni are akin to the main and-or late hydrothermal stage when Py3 developed, with As and Au probably being early hydrothermal related to Py2. Despite the low trace element concentrations in late-stage Py4 in BIF, there is an increase, especially in As, Bi, Co and Ni, during late-stage Py5, suggesting a possible new hydrothermal input (Fig. 15).

In order to better constrain the development path of the pyrite generations, integration with data from the other sulfide minerals, the correlation to geological and fluid data as well as to deformation events is necessary, so that one can deduce the physico-chemical conditions of distinct fluid stages and their evolution through time (Tardani et al., 2017). Neither in BIF, nor in carbonaceous pelite, has the early-stage anhedral pyrrhotite shown high Co concentration. However, significant Co (and Ni) enrichment in late-stage pyrrhotites and in arsenopyrite suggest that the mineralizing fluids carried these elements. Cobalt in pyrrhotite and arsenopyrite is ten times higher in carbonaceous pelite than in BIF, suggesting that the pelite was probably pre-enriched in trace elements (Fig. 10), and reacted better in reducing trace elements in the sulfide minerals when compared to the geochemically poorer BIF. Alternatively, the BIF might have other minerals that acted as sinks for Ni and Co and may not have released them into the fluid.

Ribeiro Rodrigues (1998) studied least altered and hydrothermally altered samples of two Cuiabá BIF types, and mafic volcanic and pelitic rocks of the Fonte Grande Sul (FGS) orebody at the Cuiabá deposit. The Cuiabá BIF characterized by dark quartz-carbonate layers (dominated by carbonaceous matter) revealed Co values of < 10 ppm and Ni concentrations up to 33 ppm. Whole rock geochemistry of the Serrotinho and Canta Galo gold orebodies (Fig. 2) displays Co values of up to 53 ppm. The BIF characterized by light quartz-carbonate layers has relatively lower Co and Ni concentrations of < 10 ppm. Cobalt concentrations in the least altered mafic volcanic rocks range between 49 and 84 ppm, with Ni between 50 and 76 ppm. Where altered, these are slightly more enriched with Co up to 90 ppm, and Ni values up to 263 ppm. In comparison to the Cuiabá BIF, Ni concentrations in the carbonaceous pelite are relatively high up to 94 ppm, whereas Co values are < 10 ppm (Ribeiro Rodrigues, 1998).

Enrichment of Co and Ni may have been associated with fluids that have leached metals from mafic/ultramafic units (Simard et al., 2013). These lithotypes are characteristic components of Archean greenstone belts, with the former making up a large part of the Cuiabá stratigraphy. The consistent Ni > Co abundance is observed in pyrrhotite, arsenopyrite and pyrite (except in pyrite of the carbonaceous pelite) and is likely due to pre-enrichment of Co. Such enrichment of Ni over Co in sulfide minerals has been attributed to precipitation from lower

temperature fluids (Co-rich pyrite being typical of higher temperature conditions) (Huston et al., 1995; Maslennikov et al., 2009), and/or fluids of higher fS_2 (Maslennikov et al., 2009, and references therein). Similar Co-Ni partitioning may be also relevant to pyrrhotite and arsenopyrite.
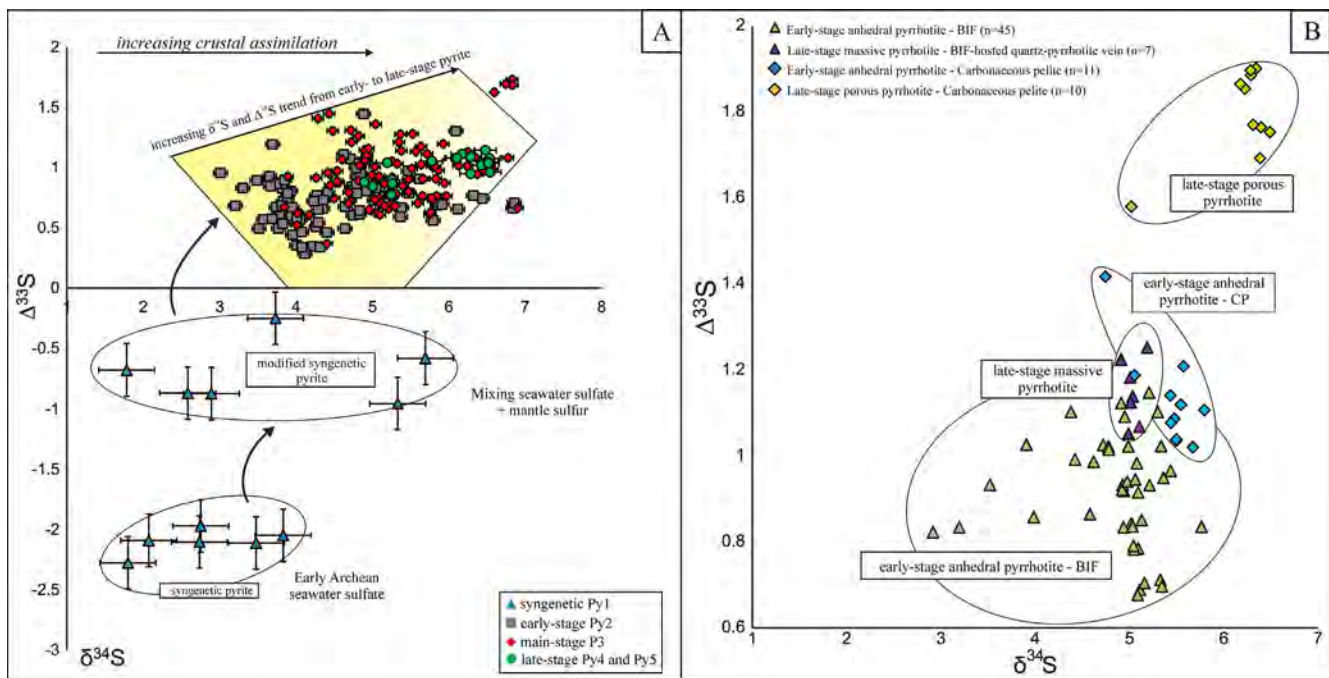
8.5. Sulfur source

Tracing the origin of sulfur places strong constraints on the origin of Au, because the transport of Au in hydrothermal fluids of orogenic gold deposits is generally assumed as bisulfide complexes (e.g., Agangi et al., 2016; Gregory et al., 2016), and the same applies to the Cuiabá deposit (Lobato et al., 2000). In Archean age rocks, the differentiation between a sedimentary S source and a hydrothermal S source can be aided by the degree of MIF of sulfur (Farquhar et al., 2000). This degree is given by the magnitude of the $\Delta^{33}S$ value and provides important information on the provenance of the S analyzed, wether S is sedimentary or hydrothermal (Gregory et al., 2016).

The $\delta^{34}S$ isotope signature is extremely variable for orogenic gold deposits (data for all ages of deposits range between 0 and +10‰) (Golding et al., 1990; Kerrich, 1987, 1979; Nesbitt, 1991; Partington and Williams, 2000; Brown et al., 2003; Bühn et al., 2012; Ribeiro et al., 2015; Steadman et al., 2015; Gregory et al., 2016; Selvaraja et al., 2017a, b; LaFlamme 2018). Earlier data by Lobato et al. (2001a,b,c) show $\delta^{34}S$ in pyrites and pyrrhotites associated with the ore zones varying from +1.4 to 5.6‰. Bühn et al. (2012) studied pyrite and chalcopyrite in BIFs from the QF, including the Cuiabá and São Bento mines. The pyrite analyses show a distinctive displacement towards positive $\Delta^{33}S$ between 0.9 and 2.2‰, which suggests a significant MIF effect (Table 7).

Photochemical reactions that result in the MIF signature have two main products: (1) sulfate, and (2) elemental S aerosols (largely S_8; Farquhar et al., 2000). These two main products have very different $\Delta^{33}S$ signatures, with S_8 having positive values, and sulfate negative values that allow determination and interpretation of the source of S in pyrite. If the S source was magmatic or mantle derived, the expected $\Delta^{33}S$ signature should be 0‰ (Farquhar and Wing, 2003). Near zero $\Delta^{33}S$ and $\delta^{34}S$ signatures reflects a H_2SO_4 source. Given the photochemical experiments from various studies, in environments where the magnitude of $\Delta^{33}S$ is relatively low varying from −1‰ to +1‰, it has been established that the relationship between the $\Delta^{33}S$ and $\Delta^{36}S$ may be used to differentiate contributed MDF-S and MIF-S processes, but may attain a wide range (Johnston, 2011; Wacey et al., 2015; Selvaraja et al., 2017a,b). The MDF-S is primarily powered by biological processes, and can create small $\Delta^{33}S$ and $\Delta^{36}S$ signatures (Johnston, 2011). In contrast, MDF-S derived $\Delta^{33}S$ and $\Delta^{36}S$ anomalies would lay along the fractionation array of −7 to −9 (Wacey et al., 2015; Roerdink et al., 2016; Selvaraja et al., 2017a). Large biologically derived MIF-S signatures require significant fractionation of $\delta^{34}S$ to very positive or negative values (Jamieson et al., 2006), whereas the maximum biologically derived MIF-S signature is dependent on the $\delta^{34}S$ variation. According to Selvaraja et al. (2017a), smaller and giant gold deposits differ in their $\Delta^{33}S/\Delta^{36}S$ ratios, reflecting different ranges of sulfur reservoirs and processes. Smaller deposits are assumed to represent a single sedimentary sulfur source with a coherent Archean $\Delta^{33}S/\Delta^{36}S$ signal (~ 0.9–1.5), whereas giant deposits may require sourcing from a wider range of sulfur reservoirs, indicating a random $\Delta^{33}S/\Delta^{36}S$ slope (Selvaraja et al., 2017a). For example, the Australian Golden Mile and the Plutonic gold deposits indicate $\Delta^{33}S/\Delta^{36}S$ arrays of 2.2 and –0.37, respectively (Selvaraja et al., 2017a).

Our $\delta^{34}S$ values show a narrow range between 1.78 and 6.90‰, representing MIF-S anomalies in the Cuiabá data, which is caused by photochemical processes (Fig. 16A). The average array of our $\Delta^{33}S/\Delta^{36}S$ results is –0.5 for all pyrite types, and from all host rocks, plotting outside the accepted MIF-S Archean array of –0.9 (Johnston, 2011; Zerkle et al., 2012), with MDF-S array ranging from –9 to –7 (Wacey

Fig. 16. $\Delta^{33}S$-$\delta^{34}S$ plot of pyrite types (Py1, Py2, Py3, Py4 and Py5) (A) independently from host rocks. The $\Delta^{33}S$ and $\delta^{34}S$ error bars (2σ) are graphically represented in both directions. The pyrite $\Delta^{33}S$-$\delta^{34}S$ plot shows seawater sulfur source of syngenetic pyrite, and mixed seawater sulfate with mantle sulfur of the modified syngenetic pyrite in carbonaceous pelite. The Py2 and Py3 display an increasing crustal assimilation up to Py4 and Py5. The pyrrhotite $\Delta^{33}S$- $\delta^{34}S$ plot (B) shows the increasing tendency from early- to late-stage pyrrhotite in BIF-related pyrrhotite and carbonaceous pelite-hosted pyrrhotite.

et al., 2015) (Fig. 11B), and displaying weak R^2 correlations of 0.22. Early- and late-stage pyrrhotite at Cuiabá display a similar behavior, with a slope of –0.4 and a R^2 correlation of 0.14. Mixing of MID-S and MDF-S can be ruled out, because it is not possible to generate this array of –0.5 (solid line in Fig. 11B) (Wacey et al., 2015, Selvaraja et al., 2017a). Instead, it is more likely that this difference reflects sourcing from multiple reservoirs, including sulfur from seawater sulfate (S^{2-}; this is reduced (S^0) and fractionated, resulting in an $\Delta^{33}S$-$\Delta^{36}S$ array trending from the top left to the bottom right quadrant in Fig. 11B.

According to Ohmoto et al. (2006), $\Delta^{33}S$ as well as $\Delta^{36}S$ anomalies could be derived from abiotic processes during diagenesis like thermochemical sulfate reduction (TRS). Experimental TRS simulations revealed a typical MIF-S range for $\Delta^{36}S$ values between 0 and 1‰ (Oduro et al., 2011). The $\Delta^{36}S$ values of the Cuiabá diagenetic and hydrothermal pyrites fall outside this range (Fig. 11B), suggesting that sulfur in this study is derived from a source that preserves Archean photochemical reaction products, such as the carbonaceous matter-bearing Cuiabá BIF and carbonaceous pelite itself.

The scattered data in the top right quadrant of Fig. 11B are uncommon for orogenic gold deposits, but comparable with data obtained by Selvaraja et al. (2017a), who interpreted this fractionation pattern as a S_3^- signature. This trisulfur radical ion becomes dominant at temperatures above 250 °C and pressures over 0.5 GPa (e.g., in hydrothermal fluids that source porphyry-epithermal mineral systems), but for orogenic gold deposits the low solubility of pyrite at above 500 °C is the major limiting factor for S_3^-. There are very few orogenic gold systems above 500 °C. Therefore, S_3^- is capable of concentrating Au only at hot stages of metamorphism (500–700 °C), where S_3^- concentrations are high enough to yield Au-enriched fluids within hypozonal orogenic gold systems (Pokrovski et al., 2015), but not relevant for mesozonal orogenic gold systems.

In the carbonaceous pelite, Py1 yields significant negative $\Delta^{33}S$ (–2.28 to –1.97‰; Fig. 16A), a signal interpreted to be derived from seawater sulfate (Ono et al., 2003). This syngenetic pyrite with negative $\Delta^{33}S$ values is more likely to have formed earlier during diagenesis, and at a time when a greater amount of free sulfate was available compared

to pyrite with a positive $\Delta^{33}S$ value. Another population of Py1 with less negative $\Delta^{33}S$ values (–0.96 to –0.25‰) may represent modification of seawater sulfate with mixed mantle sulfur carrying a near-zero $\Delta^{33}S$ signature (Fig. 16A). It may also indicate that the fluid mixed with S of positive $\Delta^{33}S$ signature, as sedimentary pyrite usually has a positive $\Delta^{33}S$ (Gregory et al., 2015b; LaFlamme et al., 2018). The lowermost eight results of Py2 and one of Py3, all in carbonaceous pelite, plot close to the MDF field, suggesting that the interaction of the gold mineralizing fluid with these grains was somewhat insignificant, since the sulfur isotope record has been maintained with a similar signature to that of Py1. As fluid-rock ratio increased, an increase in $\Delta^{33}S$ values is attained, roughly above 0.5‰ (Fig. 16A).

In andesite and BIF, early-stage Py2 and main ore-stage Py3 are characterized by positive $\Delta^{33}S$ trends without exception, indicating that an external, sedimentary-derived S source interacted with these rocks (Farquhar et al., 2000; Farquhar and Wing, 2003, 2005). The euhedral overgrowing Py3 rims show a shift towards higher positive $\Delta^{33}S$ values (~0.9‰), pointing to advanced crustal assimilation under sedimentary influence. Late-stage Py4 and Py5 show an even greater shift towards higher positive $\Delta^{33}S$ values, thus representing the pyrite types that were most influenced by the interaction with sedimentary rocks (Fig. 16A). Positive $\Delta^{33}S$ values are also indicative of relatively late formation of the pyrite because S^8 is less readily available to be incorporated into pyrite and is thus incorporated into pyrite later during diagenesis (Johnston, 2011). A similar development pattern is shown by early- to late-stage pyrrhotite hosted in the BIF and carbonaceous pelite (Fig. 16B). Laser in-situ fluid inclusion data by Kresse et al. (2018, under review) have shown that sedimentary-derived elements (especially Pb, Zn, and Cu) are consistent with these findings.

8.6. Comparison with other orogenic gold deposits

Multiple sulfur isotope studies by Ribeiro et al. (2015) undertaken for the turbidite-hosted Córrego do Sítio gold district, also situated in the QF, show $\Delta^{33}S$ values of hydrothermal pyrite ranging from + 0.27 to +3.46‰, and from + 0.7 to 2.0‰ for pyrrhotite, both ranges

Table 7
Overview of sulfur isotope data of Archean and Paleoproterozoic orogenic gold deposits worldwide.

Deposit	Size	Host rocks	Age	Sulfide mineral	Δ33S	δ34S	Reference
Cuiabá, Brazil	> 10 Moz	BIF, andesite, carbonaceous pelite	Archean	Syngenetic Py1	-2.28 to -0.25‰	+1.78 to 5.69‰	This study
				Early-stage Py2	+0.28 to 1.44‰	+3.01 to 6.86‰	
				Main-stage Py3	+0.37 to 1.73‰	+3.85 to 6.90‰	
				Late-stage Py4	+0.77 to 1.11‰	+4.90 to 6.53‰	
				Late-stage Py5	+0.96 to 1.14‰	+5.19 to 6.54‰	
				Early-stage pyrrhotite	+0.68 to 1.42‰	+1.53 to 5.80‰	
				Late-stage pyrrhotite	+1.05 to 1.90‰	+4.91 to 6.49‰	
				BIF-hosted pyrite	+0.85 to 2.18‰	+3.85 to 5.02‰	
Corrego do Sítio district, Brazil	c. 5.12 Moz	Metagraywacke and subordinate carbonaceous pelite	Archean	Hydrothermal pyrite	+0.27 to +3.46‰	+3.1 to 4.8‰	Bühn et al. 2012
				Pyrrhotite	+0.7 to 2.0‰	-2.9 to +0.1‰	Ribeiro et al., 2015
Golden Mile, Kalgoorlie gold district Australia	> 50 Moz	Mafic metavolcanics and black shale units	Neoarchean	Ore-related pyrite	Near-zero values	1) -6 to +6‰, 2) -10 to -2‰	1) Steadman et al., 2015
				Pyrite nodules	Nodule cores negative, rims positive	Positive values up to +6‰	
Wallaby, Yilgarn craton, Australia	8 Moz	Wallaby conglomerate (basalt, andesite, feldspar porphyry and quartz feldspar porphyry, BIF and quartz)	Archean	Pyrite generations (1–5)	–	-7.3 to +9.3‰	Ward et al., 2017
St. Ives Gold district, Australia	12 Moz	Pyrite-rich black shale, siliciclastic units, dolerite intrusions, granites, mafic and ultramafic extrusive rocks	Neoarchean	Sedimentary pyrite	1) 0.7 to 2.4 ‰,2) -0.9 to +0.1‰	2.3 to 7.4‰	Gregory et al., 2016
				Hydrothermally altered pyrite	+1.0 to 1.3‰	+1.1 to 5.2‰	
				Ore-stage pyrite (East Repulse deposit)	-0.13 to +0.24‰	-8.5 to +7.7‰	
Barberton greenstone belt	6 Moz	Sandstone, shale, chert, BIF and felsic volcanic rocks	Mesoarchean	Ore-stage pyrite	-0.6‰ to +1.0‰	-0.87‰ to +9.64‰	Agangi et al., 2016
Gounkoto, West Africa	> 3 Moz	Metasedimentary rocks	Paleoproterozoic	Auriferous pyrite	–	+5.8 to 12.8‰	Lambert-Smith et al., 2016
				Diagenetic pyrite	–	+6.4 to 25.1‰	
Loulo Mining District, Mali, West Africa	15.5 Moz	Metasedimentary rocks	Paleoproterozoic	Ore-stage pyrite +syngenetic pyrite	–	+5.8 to 15.5‰	Lawrence et al., 2013
				Arsenopyrite	–	+5.8 to 6.8‰	
Archaean Hattu schist belt, eastern Finland	194,000 oz	Metasedimentary rocks	Neoarchean	Pyrite	–	-9.1 to +8.5‰	Molnár et al., 2016
				Pyrrhotite	–	-4.6 to +5.6‰	

approximately similar to the Cuiabá data. In contrast, the $\delta^{34}S$ signatures of pyrrhotite are slightly different in the order of –2.9 to +0.1‰ (Table 7). Ribeiro et al. (2015) also suggest that the hydrothermal fluid responsible for gold mineralization at Córrego do Sítio interacted with the host metasedimentary sequences during its ascending path.

Comparing Cuiabá with other orogenic gold deposits of Archean and Paleoproterozoic ages worldwide, e.g. deposits in the Kalgoorlie Au district in Australia (Golden Mile and St. Ives), orogenic gold deposits in West Africa and those hosted in the Barberton greenstone belt in South Africa, the sulfur isotope data at Cuiabá is distinctly different.

For example, $\Delta^{33}S$ signatures of ore-related pyrites in the Golden Mile and the St. Ives deposits range around near-zero values and from –0.13 to +0.24‰, respectively (Steadman et al., 2015; Gregory et al., 2016). Diagenetic pyrite nodules from carbonaceous shales within the deposit contain cores with negative $\Delta^{33}S$ values, whereas the nodule rims display positive $\Delta^{33}S$ values of the Golden mile deposit (Steadman and Large, 2016). Sedimentary pyrite of the St. Ives Au deposit yields two $\Delta^{33}S$ ranges from 0.7 to 2.4‰, and from –0.9 to +0.1‰ (Table 7). Especially noticeable are the negative $\delta^{34}S$ ranges as low as $-10‰$ for the ore-stage pyrites in the Golden Mile deposit, and as low as $-8.5‰$ in the St. Ives Au district (Table 7), suggesting the presence of oxidizing fluids in the ore zones. All sulfide studies undertaken for Cuiabá show only positive $\delta^{34}S$ values, suggesting reducing fluids with fO_2 at a narrow range, below the ΣSO_2-H_2S boundary (Ohmoto and Rye, 1979), as previously suggested by Lobato et al. (2001c).

An important point to be explored is that the Rio das Velhas greenstone belt is sediment-dominated with depositional characteristics that are similar to other Archean sedimentary-dominated greenstone belts in the world (e.g., Ootes et al., 2011; Anhaeusser, 2014), e.g. the Yellowknife Supergroup, where sedimentary rocks dominate (e.g., Condie, 1981; Helmstaedt and Padgham, 1986). The latter is composed of widespread turbidites (Burwash-Wash Formations) derived from granite-gneiss, as well as felsic and mafic volcanic rocks (Taylor and McLennan, 1985). The influence of the large amount of chemical and clastic sedimentary rocks of the Nova Lima Group with regards to fluid-rock interaction and the impact on potential metal sources may be significant and of great interest for the Rio das Velhas greenstone belt. According to Guy et al. (2012), the depositional environment also affects the S isotope signature; this is the case of deep, tectonically quiescent sedimentary environments that have only positive $\Delta^{33}S$ signatures characteristic of elemental sulfur. Given that the Cuiabá deposit is situated in the metasedimentary-rich Rio das Velhas greenstone belt (Baltazar and Zucchetti, 2007), the sulfur source of early-, main and late-stage pyrites must have been supracrustal, either clastic-sedimentary or metavolcanic rocks, and BIF.

8.7. Implications for exploration

The identification of the main sulfide phases such as pyrite, pyrrhotite and arsenopyrite (Fig. 4) provide a substantial advantage for the exploration at the Cuiabá mine, because gold mineralization is related to different paragenetic stages of these sulfide minerals. Once described and paragenetically constrained, these sulfide types may be distinguished by the exploration geologists with the naked eye, which canaid the day-to-day drill core descriptions with the indication of the main ore-stages Py2 and Py3, especially in BIF and andesite.

The present study has shown that the main ore-stage pyrite types are porous Py2 and smooth (clean) Py3 in BIF and andesite, which also incorporate other metals such as As, Co, Ni, Pb, Bi and partly Mn and Ag at appreciable concentrations. Metal associations, e.g., As-Au, Au-Ag, Co-Ni, Ag-Pb and Ag-Bi may reflect the fluid signature as well as the type of fluid-rock interactions, thus representing prevalent physicochemical conditions at the time of gold mineralization. Overall, the main Au-metal associations are Au-Pb, Au-Ag and Au-As, whereby the Au-As solubility plot by Reich et al. (2005) (Fig. A1) may distinguish

between refractory and inclusion-related Au in pyrite based on the As concentration data. Our data indicate that more Au forms as inclusions rather than stays in the pyrite lattice, which could improve the mine productivity in terms of metallurgical process and decrease of the cut-off grade. Also, these metal associations are potential path finder elements in exploration efforts.

Multiple sulfur isotope analyses indicate different ranges of sulfur reservoirs and processes. According to Selvaraja et al. (2017a), the $\Delta^{33}S$/$\Delta^{36}S$ ratio in particular of pyrite analyses may be a new tool to categorize concealed Au resources in the QF and elsewhere.

9. Conclusions

A detailed classification of five pyrite types, in syngenetic, early, main and late, epigenetic-hydrothermal stages, in three different host rocks (carbonaceous pelite, BIF and andesite) has been the basis to unravel certain metal associations linked to distinct evolutionary stages at the world-class, BIF-hosted, Cuiabá orogenic gold deposit in the Archean Rio das Velhas greenstone belt. The classification also allowed the pursuit of the sulfur isotope history at Cuiabá, leading to inferrences regarding mineralizing fluid source(s). These are the highlighted points:

(i) *Ore petrography and sulfide textures:* Five pyrite types are identified, with a syngenetic, spongy Py1 present only in carbonaceous pelite; porous, early-stage Py2 is made up of Py1 in pelite, and typically forms the central portion of pyrite grains in andesite and BIF. Euhedral, main-stage Py3 appears along pyrite borders and overgrows Py2; late stage Py4 and Py5 form smooth euhedral grains in BIF (Fig. 5).

(ii) *LA-ICP-MS data results:* Py1 has high As, Co, Ni, Pb and Ag concentrations, indicating syngenetic metal enrichments (Figs. 8, A4). As Py2 results from Py1 by clustering, the high trace element concentrations are maintained, although with a large variability, which may be interpreted as unbuffered conditions and dissolution-reprecipitation reactions at this stage. Early-stage Py2 and main-stage Py3 show an increase of Co and Ni, but a decrease of Au and As. Late-stage Py4 is characterized by lower trace element concentrations; Py5 indicates an enrichment in As, Bi, Co, Ni and Pb (Fig. A4).

(iii) *Co/Ni ratios versus Bi, Ag and Au:* Pyrites have Co/Ni < 1, which is also characteristic of most syngenetic and epigenetic-hydrothermal pyrites of orogenic Au deposits. The Py2 and Py3 are more variable with some Py2 having Co/Ni ratios > 1 (up to 2.6 and 7.9). Three possibilities are suggested: 1) Higher Bi concentrations may be interpreted as Bi-Au-(Pb)-bearing inclusions of tellurides in pyrite. 2) Bismuth and Au may be more easily accumulated into the pyrite lattice if As is present and substituted into the Fe site of pyrite. 3) Bismuth enrichment and present Bi-bearing inclusions may suggest the contribution of felsic magmatic hydrothermal fluids, or leaching of granitoid rocks during fluid transport along its pathways. Regarding the Cuiabá orogenic gold deposit, for the scenario where As is present in pyrite, the second possibility is most likely.

(iv) *Pyrite-related Au mineralization:* There is strong Au-As correlation with decreasing Au and As concentration from early-stage Py2 to main-stage Py3 in andesite, and from Py2 and Py3 to Py5 in BIF (Fig. 13). This probably reflects Au having been released from Py1 of carbonaceous pelite, or from organic matter, or alternatively represents Au directly precipitated from hydrothermal fluid during shear zone activity. Using the As-Au relationship documented in hydrothermal pyrites (Reich et al., 2005), we propose that more Au forms inclusions than stays in the pyrite structure in BIF and andesite pyrites at Cuiabá (Fig. 14).

(v) *Pyrite evolution:* Paragenetic evidence of timing and geochemical behavior of trace elements in early-, main-, and late-stage pyrite types in carbonaceous pelite, BIF and andesite indicate a five-

stage evolution as shown in Fig. 15.

(vi) *Sulfur isotope data:* Pyrite $\delta^{34}S$ values range from 1.78 to +6.90‰, $\Delta^{33}S$ from –2.28 to +1.73‰, and $\Delta^{36}S$ from –2.04 to +3.19‰ (Fig. 11). Noticeable are 1) Negative $\Delta^{33}S$ values for the syngenetic Py1 in carbonaceous pelite, 2) Only positive $\Delta^{33}S$ values for other pyrite types in all other host units, 3) Lack of negative $\delta^{34}S$ values for samples analyzed.

(vii) *Sulfur source:* It is suggested that Py1 of the carbonaceous pelite was deposited in a seawater environment (non-zero $\Delta^{33}S$), and later mixed with mantle sulfur carrying a near-zero $\Delta^{33}S$ signature or alternatively a different sedimentary source with a positive $\Delta^{33}S$ (Py2 carbonaceous pelite; Fig. 13). Early-, main- and late-stage hydrothermal pyrite types (Py2, Py3, Py4 and Py5) in BIF and andesite present a continuous process of crustal assimilation (only positive $\delta^{34}S$ and $\Delta^{33}S$ values) (Fig. 16).

(viii) *Implications:* The identification of the main ore-stage pyrite types (Py2 and Py3) can aid in the drill core description by mine geologists. Porous Py2 and smooth Py3 in BIF and andesite also incorporate trace metals such as As, Co, Ni, Pb, Bi and partly Mn and Ag, reflecting fluid signature and fluid-rock interactions. The $\Delta^{33}S/\Delta^{36}S$ isotope ratio could be used as a tool of categorization between small and giant-scale gold deposit following what is postulated by Selvaraja et al. (2017a), and shown in Fig. 11B.

This study shows that trace elements such as As, Co, Ni, Pb, Ag and Au are either only hydrothermally concentrated and/or pre-enriched in each host rock, since paragenetic and hydrothermal stages of pyrite, pyrrhotite and arsenopyrite differ in their trace element signatures.

The Cuiabá deposit is closely associated with metasedimentary rocks in the Rio das Velhas greenstone belt, which has significant implications for potential metal sources, trace element concentrations and distributions as well as sulfur isotope signatures.

Acknowledgments

Appendix A. Supplementary data

Supplementary data associated with this article can be found, in the online version, at https://doi.org/10.1016/j.oregeorev.2018.05.012.

References

Agangi, A., Hofmann, A., Eickmann, B., Marin-Carbonne, J., Reddy, S.M., 2016. An atmospheric source of S in Mesoarchaean structurally controlled gold mineralisation of the Barberton Greenstone Belt. Precambr. Res. 285, 10–20.

Alkmim, F.F., Marshak, S., 1998. Transamazonian orogeny in the Southern São Francisco craton region, Minas Gerais, Brazil: evidence for Paleoproterozoic collision and collapse in the Quadrilátero Ferrífero. Precambr. Res. 90, 29–58.

Almeida, F.F.M., Hasui, Y., 1984. O pré-cambriano do Brasil. Edgar Blücher Ltda, São Paulo.

Almeida, F.F.M., 1967. Origem e evolução da plataforma brasileira. Departamento Nacional da Produção Mineral - Divisão de Geologia e Mineralogia 241, 36.

Anhaeusser, C.R., 2014. Archaean greenstone belts and associated granitic rocks–a review. J. Afr. Earth Sci. 100, 684–732.

Babinski, M., Chemale, F. Jr, Van Schmus, W.R., 1991. Geocronologia Pb/Pb em rochas carbonáticas do Supergrupo Minas Quadrilátero Ferrífero. Minas Gerais: Congresso Brasil Geoquimica 3, 628–631.

Bajwah, Z.U., Seccombe, P.K., Offler, R., 1987. Trace element distribution Co:Ni ratios and genesis of the Big Cadia iron-copper deposit, New South Wales, Australia. Mineralium Deposita 22, 292–300.

Baltazar, O., Zucchetti, M., 2007. Lithofacies associations and structural evolution of the Archean Rio das Velhas greenstone belt, Quadrilátero Ferrífero, Brazil: a review of the setting of gold deposits. Ore Geol. Rev. 32, 471–499.

Belousov, I., Large, R.R., Meffre, S., Danyushevsky, L.V., Steadman, J., Beardsmore, T., 2016. Pyrite compositions from VHMS and orogenic Au deposits in the Yilgarn Craton, Western Australia: implications for gold and copper exploration. Ore Geol. Rev. 79, 474–499.

Brown, S.M., Johnson, C.A., Watling, R.J., Premo, W.R., 2003. Constraints on the composition of ore fluids and implications for mineralising events at the Cleo gold deposit, Eastern Goldfields Province, Western Australia. Austr. J. Earth Sci. 50, 19–38.

Bühn, B., Santos, R.V., Dardenne, M.A., de Oliveira, C.G., 2012. Mass-dependent and mass-independent sulfur isotope fractionation ($\delta^{34}S$ and $\delta^{33}S$) from Brazilian Archean and Proterozoic sulfide deposits by laser ablation multi-collector ICP-MS. Chem. Geol. 312, 163–176.

Cabral, A.R., Zeh, A., Koglin Jr, N., Gomes, A.A.S., Viana, D.J., Lehmann, B., 2012. Dating the Itabira iron formation, Quadrilátero Ferrífero of Minas Gerais, Brazil, at 2.65 Ga: depositional U-Pb age of zircon from a metavolcanic layer. Precambr. Res. 204–205, 40–45.

Condie, K.C., 1981. Archean Greenstone Belts. vol. 3 Elsevier.

Cook, N.J., Ciobanu, C.L., Mao, J., 2009. Textural control on gold distribution in As-free pyrite from the Dongping, Huangtuliang and Hougou gold deposits, North China Craton (Hebei Province, China). Chem. Geol. 264, 101–121.

Costa, M., 2000. Estudo de isótopos de carbono e oxigênio e caracterização petrográfica do minério da Mina Cuiabá: Unpusblished M. Sc. thesis, Belo Horizonte, Brazil, Universidade Federal de Minas Gerais.

Danyushevsky, L., Robinson, P., Gilbert, S., Norman, M., Large, R., McGoldrick, P., Shelley, M., 2011. Routine quantitative multi-element analysis of sulphide minerals by laser ablation ICP-MS: standard development and consideration of matrix effects. Geochem. Explor. Environ. Anal. 11, 51–60.

Deditius, A.P., Reich, M., Kesler, S.E., Utsunomiya, S., Chryssoulis, S.L., Walshe, J., Ewing, R.C., 2014. The coupled geochemistry of Au and As in pyrite from hydrothermal ore deposits. Geochim. Cosmochim. Acta 140, 644–670.

Dorr, J.V.N., 1969. Physiographic, stratigraphic, and structural development of the Quadrilátero Ferrífero, Minas Gerais, Brazil, U.S. Geological Survey Professional paper, v. 614 (A), p. 110.

Farina, F., Albert, C., Lana, C., 2015. The Neoarchean transition between medium-and high-K granitoids: clues from the Southern São Francisco Craton (Brazil). Precambr. Res. 266, 375–394.

Farquhar, J., Bao, H., Thiemens, M., 2000. Atmospheric influence of Earth's earliest sulfur cycle. Science 289, 756–758.

Farquhar, J., Wing, B.A., 2003. Multiple sulfur isotopes and the evolution of the atmosphere. Earth Planet. Sci. Lett. 213, 1–13.

Farquhar, J., Wing, B.A., 2005. The terrestrial record of stable sulphur isotopes: a review of the implications for evolution of Earth's sulphur cycle: Geological Society of London. Spec. Publ. 248, 167–177.

Farquhar, J., Peters, M., Johnston, D.T., Strauss, H., Masterson, A., Wiechert, U., Kaufman, A.J., 2007. Isotopic evidence for Mesoarchean anoxia and changing atmospheric sulphur chemistry. Nature 449, 706.

Farquhar, J., Cliff, J., Zerkle, A.L., Kamyshny, A., Poulton, S.W., Claire, M., Adams, D., Harms, B., 2013. Pathways for Neoarchean pyrite formation constrained by mass-independent sulfur isotopes. Proc. Natl. Acad. Sci. 110, 17638–17643.

Finch, E.G., Tomkins, A.G., 2017. Pyrite-Pyrrhotite Stability in a Metamorphic Aureole: Implications for Orogenic Gold Genesis. Econ. Geol. 112, 661–674.

Gregory, D.D., Meffre, S., Large, R.R., 2014. Comparison of metal enrichment in pyrite framboids from a metal-enriched and metal poor estuary. Am. Mineral. 99, 633–644.

Gregory, D.D., Large, R.R., Halpin, J.A., Baturina, E.L., Lyons, T.W., Wu, S., Bull, S.W., 2015a. Trace element content of sedimentary pyrite in black shales. Econ. Geol. 110, 1389–1410.

Gregory, D.D., Large, R.R., Halpin, J.A., Steadman, J.A., Hickman, A., Ireland, T., Holden, P., 2015b. The chemical conditions of the Late Archean Hamersley Basin inferred from whole rock and pyrite geochemistry with $\Delta^{33}S$ and $\delta^{34}S$ isotope analyses. Geochim. Cosmochim. Acta 149, 223–250.

Gregory, D.D., Large, R.R., Bath, A.B., Steadman, J.A., Wu, S., Danyushevsky, L., Ireland, T.R., 2016. Trace element content of pyrite from the Kapai Slate, St. Ives Gold District, Western Australia. Econ. Geol. 111, 1297–1320.

Golding, S.D., Groves, D.I., McNaughton, N.J., Mikuck, E.J., Sang, J.H., 1990. Source of ore fluid and ore components: sulphur isotope studies. In: Ho, S.E., Groves, D.I., Bennett, J.M. (Eds.), Gold deposits of the Archaean Yilgarn Block, Western Australia: nature, genesis and exploration guides. Publication 20. Geology Department and Extension Services, University of Western Australia, Perth, pp. 259–262.

Groves, D.I., Goldfarb, R.J., Gebre-Mariam, M., Hagemann, S., Robert, F., 1998. Orogenic gold deposits: a proposed classification in the context of their crustal distribution and relationship to other gold deposit types. Ore Geol. Rev. 13, 7–27.

Groves, D.I., Goldfarb, R.J., Knox-Robinson, C.M., Ojala, J., Gardoll, S., Yun, G.Y., Holyland, P., 2000. Late-kinematic timing of orogenic gold deposits and significance for computer-based exploration techniques with emphasis on the Yilgarn Block, Western Australia. Ore Geol. Rev. 17, 1–38.

Groves, D.I., Goldfarb, R.J., Robert, F., Hart, C.J.R., 2003. Gold deposits in metamorphic belts: overview of current understanding, outstanding problems, future research, and exploration significance. Econ. Geol. 98, 1–29.

Guy, B., Beukes, N., Gutzmer, J., 2010. Paleoenvironmental controls on the texture and chemical composition of pyrite from nonconglomerate sedimentary rocks of the Mesoarchean Witwatersrand Supergroup, South Africa. S. Afr. J. Geol. 113, 195–228.

Guy, B.M., Ono, S., Gutzmer, J., Kaufman, A.J., Lin, Y., Fogel, M.L., Beukes, N.J., 2012. A multiple sulfur and organic carbon isotope record from non-conglomeratic sedimentary rocks of the Mesoarchean Witwatersrand Supergroup, South Africa. Precambr. Res. 216, 208–231.

Hagemann, S.G., Cassidy, K.F., 2000. Archean orogenic lode gold deposits. Rev. Econ. Geol. 13, 9–68.

Helmstaedt, H., Padgham, W.A., 1986. A new look at the stratigraphy of the Yellowknife Supergroup at Yellowknife, NWT-implications for the age of gold-bearing shear zones and Archean basin evolution. Can. J. Earth Sci. 23, 454–475.

Huston, D.L., Sie, S.H., Suter, G.F., Cooke, D.R., Both, R.A., 1995. Trace elements in sulfide minerals from eastern Australian volcanic-hosted massive sulfide deposits; Part I, Proton microprobe analyses of pyrite, chalcopyrite, and sphalerite, and Part II, Selenium levels in pyrite; comparison with $\delta^{34}S$ values and implications for the source of sulfur in volcanogenic hydrothermal systems. Econ. Geol. 90, 1167–1196.

Ireland, T.R., Schram, N., Holden, P., Lanc, P., Ávila, J., Armstrong, R., Amelin, Y., Latimore, A., Corrigan, D., Clement, S., Foster, J.J., Compston, W., 2014. Charge-mode electrometer measurements of S-isotopic compositions on SHRIMP-SI. Int. J. Mass Spectrom. 359, 26–37.

Jamieson, J.W., Wing, B.A., Hannington, M.D., Farquhar, J., 2006. Evaluating isotopic equilibrium among sulfide mineral pairs in Archean ore deposits: case study from the Kidd Creek VMS deposit, Ontario, Canada. Econ. Geol. 101, 1055–1061.

Johnston, D.T., 2011. Multiple sulfur isotopes and the evolution of earth's surface sulfur cycle. Earth Sci. Rev. 106, 161–183.

Kerrich, R., 1987. The stable isotope geochemistry of Au-Ag vein deposits in metamorphic rocks. In: Kyser, T.K. (ed.) Mineralogical Association of Canada, Short Course, 13, pp. 287–336.

Kerrich, R., Fryer, B., 1979. Archaean precious-metal hydrothermal systems, Dome Mine, Abitibi Greenstone Belt. II. REE and oxygen isotope relations. Can. J. Earth Sci. 16, 440–458.

Kresse, C., Lobato, L.M., Figueiredo e Silva R.C., Hagemann, S.G., Banks, D., Vitorino, A.L. A., 2018. Fluid signature of the world-class BIF-hosted Cuiabá gold deposit in the Rio das Velhas greenstone belt, Brazil: a fluid inclusion study. Mineralium Deposita, under review.

Ladeira, E.A., 1980. Metallogenesis of gold at the Morro Velho mine and in the Nova Lima District, Quadrilatero Ferrifero, Minas Gerais, Brazil, Ontario (Ph.D. thesis). University of Western Ontario 272 p.

LaFlamme, C., Martin, L., Jeon, H., Reddy, S.M., Selvaraja, V., Caruso, S., Bui, T.H., Roberts, M.P., Voute, F., Hagemann, S., Wacey, D., Littman, S., Wing, B., Fiorentini, M., Kilburn, M.R., 2016. In situ multiple sulfur isotope analysis by SIMS of pyrite, chalcopyrite, pyrrhotite, and pentlandite to refine magmatic ore genetic models. Chem. Geol. 444, 1–15.

LaFlamme, C., Jamieson, J.W., Fiorentini, M.L., Thébaud, N., Caruso, S., Selvaraja, V., 2018. Investigating sulfur pathways through the lithosphere by tracing mass independent fractionation of sulfur to the Lady Bountiful orogenic gold deposit, Yilgarn Craton. Gondwana Res. 58, 27–38.

Large, R.R., Maslennikov, V.V., Robert, F., Danyushevsky, L.V., Chang, Z., 2007. Multistage sedimentary and metamorphic origin of pyrite and gold in the giant Sukhoi Log deposit, Lena gold province, Russia. Econ. Geol. 102, 1233–1267.

Large, R.R., Danyushevsky, L., Hollit, C., Maslennikov, V., Meffre, S., Gilbert, S., Bull, S., Scott, R., Emsbo, P., Thomas, H., Singh, B., Foster, J., 2009. Gold and trace element zonation in pyrite using a laser imaging technique: implications for the timing of gold in orogenic and Carlin-style sediment-hosted deposits. Econ. Geol. 104, 635–668.

Large, R.R., Bull, S.W., Maslennikov, V.V.A., 2011. Carbonaceous sedimentary source-rock model for Carlin-type and orogenic gold deposits. Econ. Geol. 106, 331–358.

Large, R., Thomas, H., Craw, D., Henne, A., Henderson, S., 2012. Diagenetic pyrite as a source for metals in orogenic gold deposits, Otago Schist, New Zealand. New Zealand J. Geol. Geophys. 55, 137–149.

Large, R.R., Halpin, J.A., Danyushevsky, L.V., Maslennikov, V.V., Bull, S.W., Long, J.A., Gregory, D.D., Lounejeva, E., Lyons, T.W., Sack, P.J., McGoldrick, P.J., Calver, C.R., 2014. Trace element content of sedimentary pyrite as a new proxy for deep-time ocean atmosphere evolution. Earth Planetary Sci. Lett. 389, 209–220.

Lambert-Smith, J.S., Lawrence, D.M., Vargas, C.A., Boyce, A.J., Treloar, P.J., Herbert, S., 2016. The Gounkoto Au deposit, West Africa: Constraints on ore genesis and volatile sources from petrological, fluid inclusion and stable isotope data. Ore Geol. Rev. 78, 606–622.

Lawrence, D.M., Treloar, P.J., Rankin, A.H., Harbidge, P., Holliday, J., 2013. The geology and mineralogy of the Loulo mining district, West Africa: Evidence for two distinct styles of orogenic gold mineralization. Econ. Geol. 108, 199–227.

Lobato, L.M., Vieira, F.W.R., 1998. Styles of hydrothermal alteration and gold mineralization associated with the Nova Lima Group, Quadrilátero Ferrífero: Part II, the Archaean mesothermal gold-bearing hydrothermal system. Braz. J. Geol. 28, 355–366.

Lobato, L.M., Ribeiro Rodrigues, L.C., Zucchetti, M., 2000. Geology and gold mineralization in the Rio das Velhas greenstone belt, Quadrilátero Ferrífero (Minas Gerais state, Brazil). In: 31st International Geological Congress, edited 2000 Rio de Janeiro.

Lobato, L.M., Ribeiro Rodrigues, L.C., Zucchetti, M., Noce, C.M., Baltazar, O.F., da Silva, L., Pinto, C., 2001a. Brazil's premier gold province, part I: the tectonic, magmatic, and structural setting of the Archean Rio das Velhas greenstone belt, Quadrilátero Ferrífero. Mineralium Deposita 36, 228–248.

Lobato, L.M., Ribeiro Rodrigues, L.C., Vieira, F.W.R., 2001b. Brazil's premier gold province, part II: geology and genesis of gold deposits in the Archean Rio das Velhas greenstone belt, Quadrilátero Ferrífero. Mineralium Deposita 36, 249–277.

Lobato, L.M., Ribeiro Rodrigues, L.C., Costa M.N.S., Martins, R., Lehne, E., Alves, J.V., Tassinari, C.G., Vieira, F.W.R., Biasi, E.E., Figueiredo e Silva, R.C., Pereira, V.C.A., Noce, C.M., 2001c. Geologia do depósito de ouro Cuiabá, Quadrilátero Ferrífero, Minas Gerais. In: Jost, H., Brod, J.A., Queiroz, E.T. de (eds.) Caracterização de depósitos auríferos em distritos minerais brasileiros. Departamento Nacional da Produção Mineral (DNPM) / Agência para o Desenvolvimento Tecnológico da Indústria Mineral Brasileira (ADIMB), pp. 3–77.

Lobato, L.M., Baltazar, O.F., Reis, L.B., Achtschin, A.B., Baars, F.J., Timbó, M.A., Berni, G.V., Mendonça, B.R.V., Ferreira, D.V., 2005. Projeto Geologia do Quadrilátero Ferrífero - Integração e Correção Cartográfica em SIG com Nota Explicativa. CODEMIG, CD-ROM, Belo Horizonte.

Lobato, L.M., Renger, F.E., Figueiredo e Silva R.C., Rosière C.A., Baars F.J., Rolim, V.K., 2014. Metalogênese do setor meridional do Cráton Sao Francisco. Metalogênese das províncias tectônicas brasileiras 1, 119–140.

Machado, N., Schrank, Abreu, F.R., Knauer, L.G., Almeida Abreu, P.A., 1989, Resultados preliminares da geocronologia U/Pb na Serra do Espinhaço Meridional. V Simpósio Geologia de Minas Gerais, pp. 171–174, Belo Horizonte.

Machado, N., Carneiro, M., 1992. U-Pb evidence of late Archean tectono-thermal activity in the southern São Francisco shield, Brazil. Can. J. Earth Sci. 29, 2341–2346.

Martins, R., 2000. Caracterização petrográfica e geoquímica mineral do minério da mina de ouro Cuiabá, Quadrilátero Ferrífero, Minas Gerais: Unpublished M. Sc. thesis. Belo Horizonte, Brazil, Universidade Federal Minas Gerais, p. 125.

Martins, B. S., 2016. Gênese e evolução do depósito arqueano aurífero Lamego: Mapeamento litoestrutural, modelamento 3D, geocronologia, paragênese mineral, mapas químicos e ablação a laser em sulfetos. Unpublished M. Sc. thesis, Belo Horizonte, Brazil, Universidade Federal de Minas Gerais.

Martins, B.S., Lobato, L.M., Rosière, C.A., Hagemann, S.G., Santos, J.O.S., Villanova, F.L.d.S.P., Figueiredo e Silva, R.C., Lemos, L.H., 2016. The Archean BIF-hosted Lamego gold deposit Rio das Velhas greenstone belt, QuadriláteroFerrífero: evidence for Cambrian structural modification of an Archean orogenic gold deposit. Ore Geol. Rev. 72, 963–988.

Maslennikov, V., Maslennikova, S., Large, R., Danyushevsky, L., 2009. Study of trace element zonation in vent chimneys from the Silurian Yaman-Kasy volcanic-hosted massive sulfide deposit (Southern Urals, Russia) using laser ablation-inductively coupled plasma-mass spectrometry (LA-ICPMS). Econ. Geol. 104, 1111–1141.

Molnár, F., Mänttäri, I., O'Brien, H., Lahaye, Y., Pakkanen, L., Johanson, B., Käpyaho, A., Sorjonen-Ward, P., Whitehouse, M., Sakellaris, G., 2016. Boron, sulfur and copper isotope systematics in the orogenic gold deposits of the Archaean Hattu schist belt, eastern Finland. Ore Geol. Rev. 77, 133–162.

Moreira, H., Lana, C., Nalini, H.A., 2016. The detrital zircon record of an Archean convergent basin in the southern São Francisco Craton, Brazil. Precambr. Res. 275, 84–99.

Morey, A.A., Tomkins, A.G., Bierlein, F.P., Weinberg, R.F., Davidson, G.J., 2008. Bimodal distribution of gold in pyrite and arsenopyrite: examples from the Archean Boorara and Bardoc shear systems, Yilgarn Craton, Western Australia. Econ. Geol. 103, 599–614.

Nesbitt, B.E., 1991. Phanerozoic gold deposits in tectonically active continental margins. Gold Metallogeny Explor. 104–132.

Neyedley, K., Hanley, J.J., Fayek, M., Kontak, D.J., 2017. Textural, Fluid Inclusion, and Stable Oxygen Isotope Constraints on Vein Formation and Gold Precipitation at the 007 Deposit, Rice Lake Greenstone Belt, Bissett, Manitoba, Canada. Econ.Geol. 112, 629–660.

Noce, C.M., 1995. Geocronologia dos eventosmagmáticos, sedimentares e metamórficosnaregião do Quadrilátero Ferrífero. Universidade de São Paulo, Minas Gerais.

Noce, C. M., 2013. Geochronology of the Quadrilátero Ferrífero: a review. Revista Geonomos 8, 15–23.

Noce, C.M., Zucchetti, M., Baltazar, O., Armstrong, R., Dantas, E., Renger, F.E., Lobato, L.M., 2005. Age of felsic volcanism and the role of ancient continental crust in the evolution of the Neoarchean Rio das Velhas Greenstone belt (Quadrilátero Ferrífero, Brazil): U-Pb zircon dating of volcaniclastic graywackes. Precambr. Res. 141, 67–82.

Noce, C.M., Tassinari, C., Lobato, L.M., 2007. Geochronological framework of the Quadrilátero Ferrífero, with emphasis on the age of gold mineralization hosted in Archean greenstone belts. Ore Geol. Rev. 32, 500–510.

Oduro, H., Harms, B., Sintim, H.O., Kaufman, A.J., Cody, G., Farquhar, J., 2011. Evidence of magnetic isotope effects during thermochemical sulfate reduction. Proc. Natl. Acad. Sci. 108, 17635–17638.

Ohmoto, H., Rye, R.O., 1979. Isotopes of sulfur and carbon. Geochem. Hydrothermal Ore Dep. 509–567.

Ohmoto, H., Watanabe, Y., Ikemi, H., Poulson, S.R., Taylor, B.E., 2006. Sulphur isotope evidence for an oxic Archaean atmosphere. Nature 442, 908–911.

Oliver, N.H., Thomson, B., Freitas-Silva, F.H., Holcombe, R.J., Rusk, B., Almeida, B.S.,

Dardenne, M.A., 2015. Local and regional mass transfer during thrusting, veining, and boudinage in the genesis of the giant shale-hosted Paracatu gold deposit, Minas Gerais, Brazil. Econ. Geol. 110, 1803–1834.

Ono, S., Eigenbrode, J.L., Pavlov, A.A., Kharecha, P., Rumble, D., Kasting, J.F., Freeman, K.H., 2003. New insights into Archean sulfur cycle from mass-independent sulfur isotope records from the Hamersley Basin, Australia. Earth Planet. Sci. Lett. 213, 15–30.

Ootes, L., Morelli, R.M., Creaser, R.A., Lentz, D.R., Falck, H., Davis, W.J., 2011. The timing of Yellowknife gold mineralization: A temporal relationship with crustal anatexis? Econ. Geol. 106, 713–720.

Partington, G.A., Williams, P.J., 2000. Proterozoic lode gold and (iron)-copper-gold deposits; a comparison of Australian and global examples. Rev. Econ. Geol. 13, 69–101.

Pereira, S.L.M., Lobato, L.M., Ferreira, J.E., Jardim, E.C., 2007. Nature and origin of the BIF-hosted São Bento gold deposit, Quadrilátero Ferrífero, Brazil, with special emphasis on structural controls. Ore Geol. Rev. 32, 571–595.

Pitcairn, I.K., Teagle, D.A., Craw, D., Olivo, G.R., Kerrich, R., Brewer, T.S., 2006. Sources of metals and fluids in orogenic gold deposits: insights from the Otago and Alpine Schists, New Zealand. Econ. Geol. 101, 1525–1546.

Pokrovski, G.S., Kokh, M.A., Guillaume, D., Borisova, A.Y., Gisquet, P., Hazemann, J.L., Lahera, E., Del Net, W., Proux, O., Testemale, D., Haigis, V., Jonchière, R., Seitsonen, A.P., Ferlat, G., Vuilleumier, R., Saitta, A.M., Boiron, M.C., Dubessy, J., 2015. Sulfur radical species form gold deposits on Earth. Proc. Natl. Acad. Sci. 112, 13484–13489.

Reich, M., Kesler, S.E., Utsunomiya, S., Palenik, C.S., Chryssoulis, S.L., Ewing, R.C., 2005. Solubility of gold in arsenian pyrite. Geochim. Cosmochim. Acta 69, 2781–2796.

Ribeiro, Y., Figueiredo e Silva, R.C., Lobato, L.M., Lima, L.C., Rios, F.J., Hagemann, S.G., Cliff, J., 2015. Fluid inclusion and sulfur and oxygen isotope studies on quartz-carbonate-sulfide veins of the Carvoaria Velha deposit Córrego do Sítio gold lineament, Quadrilátero Ferrífero, Minas Gerais, Brazil. Ore Geol. Rev. 67, 11–33.

Ribeiro Rodrigues, L.C., 1998. Gold mineralization in Archean banded iron-formation of the QF, Minas Gerais, Brazil-The Cuiabá Mine, Unpublished Philosophy thesis, RTWH Aachen, Aachen, p. 262.

Ribeiro Rodrigues, L.C., de Oliveira, C.G., Friedrich, G., 2007. The Archean BIF-hosted Cuiabá Gold deposit Quadrilátero Ferrífero, Minas Gerais, Brazil. Ore Geol. Rev. 32, 543–570.

Ridley, J.R., Diamond, L.W., 2000. Fluid chemistry of orogenic lode gold deposits and implications for genetic models: review. Econ. Geol. 13, 141–162.

Roerdink, D.L., Mason, P.R., Whitehouse, M.J., Brouwer, F.M., 2016. Reworking of atmospheric sulfur in a Paleoarchean hydrothermal system at Londozi, Barberton Greenstone Belt, Swaziland. Precambr. Res. 280, 195–204.

Schindler, C., Hagemann, S.G., Banks, D., Mernagh, T., Harris, A.C., 2016. Magmatic hydrothermal fluids at the sedimentary rock-hosted, intrusion-related Telfer gold-copper deposit, Paterson Orogen, Western Australia: pressure-temperature-composition constraints on the ore-forming fluids. Econ. Geol. 111, 1099–1126.

Schrank, A., Machado, N., 1996. Idades U-Pb em monazitas e zircões das minas de Morro Velho e Passagem de Mariana-Quadrilátero Ferrífero (MG). SBG Congresso Brasileiro de Geologia 39, 470–472.

Scott, R.J., Meffre, S., Woodhead, J., Gilbert, S.E., Berry, R.F., Emsbo, P., 2009. Development of framboidal pyrite during diagenesis, low-graderegional metamorphism, and hydrothermal alteration. Econ. Geol. 104, 1143–1168.

Selvaraja, V., Caruso, S., Fiorentini, M.L., LaFlamme, C.K., Bui, T.H., 2017a. Atmospheric sulfur in the orogenic gold deposits of the Archean Yilgarn Craton, Australia. Geology G39018–G39021.

Selvaraja, V., Fiorentini, M.L., LaFlamme, C.K., Wing, B.A., Bui, T.H., 2017b. Anomalous sulfur isotopes trace volatile pathways in magmatic arcs. Geology 45, 419–422.

Selvaraja, V., Fiorentini, M.L., Jeon, H., Savard, D.D., LaFlamme, C.K., Guagliardo, P., Caruso, S., Bui, T.H., 2017c. Evidence of local sourcing of sulfur and gold in an Archaean sediment-hosted gold deposit. Ore Geol. Rev. 89, 909–930.

Simard, M., Gaboury, D., Daigneault, R., Mercier-Langevin, P., 2013. Multistage gold mineralization at the Lapa mine, Abitibi subprovince: insights into auriferous hydrothermal and metasomatic processes in the Cadillac-Larder Lake fault zone. Mineralium Deposita 48, 883–905.

Spear, F.S., 1995. Metamorphic phase equilibria and pressure-temperature-time paths. Mineralogical Society of America, Washington, pp. 799.

Steadman, J.A., Large, R.R., Meffre, S., Olin, P.H., Danyushevsky, L.V., Gregory, D.D., Holden, P., 2015. Synsedimentary to early diagenetic gold in black shale-hosted pyrite nodules at the Golden Mile Deposit, Kalgoorlie, Western Australia. Econ. Geol. 110, 1157–1191.

Steadman, J.A., Large, R.R., 2016. Synsedimentary, diagenetic, and metamorphic pyrite, pyrrhotite, and marcasite at the Homestake BIF-Hosted gold deposit, South Dakota, USA: insights on Au-As ore genesis from textural and LA-ICP-MS trace element studies. Econ. Geol. 111, 1731–1752.

Sung, Y.H., Brugger, J., Ciobanu, C.L., Pring, A., Skinner, W., Nugus, M., 2009. Invisible gold in arsenian pyrite and arsenopyrite from a multistage Archaean gold deposit: Sunrise Dam, Eastern Goldfields Province, Western Australia. Mineralium Deposita 44, 765–791.

Tardani, D., Reich, M., Deditius, A.P., Chryssoulis, S., Sánchez-Alfaro, P., Wrage, J., Roberts, M.P., 2017. Copper-arsenic decoupling in an active geothermal system: a link between pyrite and fluid composition. Geochim. Cosmochim. Acta 204, 179–204.

Taylor, S.R., McLennan, S.M., 1985. The Continental Crust: Its Composition and Evolution. Blackwell, London.

Thomas, H.V., Large, R.R., Bull, S.W., Maslennikov, V., Berry, R.F., Fraser, R., Froud, S., Moye, R., 2011. Pyrite and pyrrhotite textures and composition in sediments, laminated quartz veins, and reefs at Bendigo gold mine, Australia: insights for ore genesis. Econ. Geol. 106, 1–31.

Toledo, C., 1997. Controle estructural da mineralicão aurifera na mina de Cuiabá, setor noroeste do Greenstone Belt Rio das Velhas, Quadrilátero Ferrífero: Unpublished M. Sc. thesis, Campinas, Brazil, Universidade Estadual de Campinas.

Tomkins, A.G., 2013. On the source of orogenic gold. Geology 41, 1255–1256.

Tribovillard, N., Algeo, T.J., Lyons, T., Riboulleau, A., 2006. Trace metalsas paleoredox and paleoproductivity proxies: an update. Chem. Geol. 232, 12–32.

Ushikubo, T., Williford, K.H., Farquhar, J., Johnston, D.T., Van Kranendonk, M.J., Valley, J.W., 2014. Development of in situ four-isotope analysis with multiple Faraday cup detectors by SIMS and application to pyrite grains in a Paleoproterozoic glaciogenic sandstone. Chem. Geol. 383, 86–99.

Velásquez, G., Béziat, D., Salvi, S., Siebenaller, L., Borisova, A.Y., Pokrovski, G.S., De Parseval, P., 2014. Formation and deformation of pyrite and implications for gold mineralization in the El Callao District, Venezuela. Econ. Geol. 109, 457–486.

Vial, D., 1980. Mapeamento Geológico do Nivel 3 da mina de Cuiabá, Mineração Morro Velho SA, Internal Report.

Vial, D.S., 1988a, Mina de ouro de Cuiabá, Quadrilátero Ferrífero, Minas Gerais. In: Schobenhaus-Filho, C., Coelho, C.E.S. (eds) Metais básicos não ferrosos, ouro e alumínio. (Prinicpais depositis minerais do Brasil 3): Departamento Nacional da Produção Mineral/Campanhia Vale Rio Doce, Brasília, pp. 413–419.

Vieira, F.W.R., 1988. Processos epigenéticos da formação dos depósitos auríferos e zonas de alteração hidrotermal do Grupo Nova Lima, Quadrilátero Ferrífero, Minas Gerais. In: 35th Congresso Brasileiro Geololgia. Sociedade Brasileira Geologia, Belém, Brazil, 1, pp. 76–86.

Vieira, F.W.R., 1991. Textures and processes of hydrothermal alteration and mineralization in the Nova Lima Group, Minas Gerais, Brazil, In: Ladeira EA (ed.) The economics, geology, geochemistry and genesis of gold deposits. AA Balkema, Rotterdam, The Netherlands: Brazil Gold, pp. 319–325.

Vieira, F.W.R., Oliveira, G.A.I., 1988. Geologia do Distrito Aurífero de Nova Lima, Minas Gerais. In: Schobbenhaus, C., Coelho, C.E.S. (coord.) Principals Depósitos Minerais do Brasil. Brasilia, DNPM/CVRD, 3, pp. 377–391.

Vitorino, A.L.A., 2017. Mineralização aurífera associada aos veios quartzo-carbonáticos hospedados na unidade máfica basal da Jazida Cuiabá, Greenstone Belt Rio das Velhas, Quadrilátero Ferrífero, Minas Gerais, Brasil. Unpusblished M. Sc. thesis, Belo Horizonte, Brazil, Universidade Federal de Minas Gerais.

Wacey, D., Noffke, N., Cliff, J., Barley, M.E., Farquhar, J., 2015. Micro-scale quadruple sulfur isotope analysis of pyrite from the ~ 3480Ma Dresser Formation: New insights into sulfur cycling on the early Earth. Precambr. Res. 258, 24–35.

Ward, J., Mavrogenes, J., Murray, A., Holden, P., 2017. Trace element and sulfur isotopic evidence for redox changes during formation of the Wallaby Gold Deposit, Western Australia. Ore Geol. Rev. 82, 31–48.

Whitehouse, M.J., 2013. Multiple sulfur isotope determination by SIMS: Evaluation of reference sulfides for $\Delta^{33}S$ with observations and a case study on the determination of $\Delta^{36}S$. Geostand. Geoanal. Res. 37, 19–33.

Wilson, S.A., Ridley, W.I., Koenig, A.E., 2002. Development of sulfide calibration standards for the laser ablation inductively-coupled plasma mass spectrometry technique. J. Anal. At. Spectrom. 17, 406–409.

Wood, B.L., Large, R.R., 2007. Syngenetic gold in western Victoria: Occurrence, age and dimensions. Aust. J. Earth Sci. 54, 711–732.

Xavier, R.P., Toledo, C.L.B., Taylor, B., Schrank, A., 2000. Fluid Evolution and gold deposition at the Cuiabá Mine, SE Brazil: fluid inclusions and stable isotope geochemistry of carbonates. Revista Brasileira de Geociências 30, 337–341.

Xue, Y., Campbell, I., Ireland, T.R., Holden, P., Armstrong, R., 2013. No mass-independent sulfur isotope fractionation in auriferous fluids supports a magmatic origin for Archean gold deposits. Geology 41, 791–794.

Zerkle, A.L., Claire, M.W., Domagal-Goldman, S.D., Farquhar, J., Poulton, S.W., 2012. A bistable organic-rich atmosphere on the Neoarchaean Earth. Nat. Geosci. 5, 359–363.

Zhao, H.X., Frimmel, H.E., Jiang, S.Y., Dai, B.Z., 2011. LA-ICP-MS trace element analysis of pyrite from the Xiaoqinling gold district, China: implications for ore genesis. Ore Geol. Rev. 43, 142–153.

Chapter 4

Final considerations

To finalize, we aim to establish a linkage between the hydrothermal fluid evolution of the andesite-hosted, quartz vein-associated VQZ orebody and the pyrite evolution including metal and sulfur isotope variations in sulfides from the BIF-hosted FGS orebody at the Cuiabá orogenic Au deposit. Based on microthermometry and LA-ICP-MS studies on fluid inclusions and LA-ICP-MS analyses on sulfide minerals we try to connect fluid characteristics and the possibility for the trace metal transport.

The first hydrothermal pulse (1st pulse fluid) includes the development of V1 shear to V3 extensional array veins, and is characterized by an aqueous-carbonic, low to moderate saline, high temperature fluid (Fig. 13, Chapter 2), which probably transported certain trace metals complexed with sulfur. In contrast, the second hydrothermal pulse (2nd pulse fluid), comprising the late-stage V4 development, shows an aqueous-carbonic, low to moderate saline and clearly cooler fluid (Fig. 13, Chapter 2), which probably limited the capacity of trace metals being transported as efficiently, and thus precipitated. This may explain the relative abundance of trace elements.

An attempt to attribute trace element signatures in FIAs to trace element signatures in different pyrite generations is performed. Py1 in the carbonaceous pelite does not correspond to hydrothermal stages, as we assume a syngenetic origin for Py1, and should not be considered in this final discussion. Early-stage Py2 is considered part of the 1st pulse fluid corresponding to the V2 vein development. This is based on higher As and Au contents in Py2 than in Py3 (Fig. A4, Chapter 3), as well as lower As and Au concentrations in FIAs of V2 veins compared to V1 and V4 veins 9Fig. 9, Chapter 2). This implies an early precipitation of As and Au. Main-stage Py3 is characterized by lower Ag, As and Au concentrations in comparison to early-stage Py2 (Fig. A4, Chapter 3). For example, Ag values increase in FIAs from V1/V2 to V3 extensional array veins (Fig. 9, Chapter 2), while Ag concentrations indicate a decreasing tendency from Py2 to Py3. Py3 is also related to the 1st pulse corresponding to the V3 vein development. Both late-stage Py4 and Py5 may be attributed to the 2nd pulse and non-mineralized late-stage V4 vein generation by comparing the reverse trend of lower (decreasing) Pb and Mn concentrations in FIAs trapped in V4 and higher (increasing) Pb and Mn concentrations in Py4 and Py5 (Fig. 9, Chapter 2; Fig. A4, Chapter 3). Further, analyzed Au concentrations in FIAs in late-stage V4 veins and the lack of Au values in late-stage BIF-hosted Py4 and Py5 types suggest that Au stayed in the fluid and was not

precipitated (in this case in BIF-hosted pyrites) as conditions for Au precipitation and mineralization probably were not attained at this stage.

Both studies show that the ore-forming fluid was geochemically influenced by sedimentary units of the Archean Rio das Velhas greenstone belt. Indications from the fluid inclusion work are noticeable Pb and Zn concentrations in FIAs trapped in quartz of gold mineralized veins of the VQZ orebody. The sulfide mineral study of the FGS orebody provides multiple sulfur isotope data clearly demonstrating sedimentary-derived sulfur in analyzed pyrites and pyrrhotites (Fig. 16, Chapter 3).

One of the many remaining questions is: *How does a two-pulse hydrothermal fluid evolution implicates a five-type pyrite evolution?*

Independent whether a quartz vein-associated, andesite-hosted orebody or BIF-hosted orebody, the ore-forming fluid responsible for the Archean gold mineralization at the Cuiabá orogenic gold deposit is the same. The key difference is that the VQZ orebody hosts gold mainly as free gold in quartz veins, whereby the BIF-hosted FGS orebody hosts gold mainly as lattice-bound, or even finely distributed nano inclusions in pyrite, arsenopyrite and pyrrhotite. At this, we have to consider that gold precipation can take place in different ways, pressure release and replacement. Free gold in andesite-hosted quartz veins is predominantly precipitated by pressure release as Fe-minerals (sulfide minerals) are rare, and therefore the possibility of replace Fe in sulfide minerals is not available. Commonly gold substitute the Fe site in pyrite, arsenopyrite and pyrrhotite, what is indicated by lattice-bound Au and nano inclusions, replacing sulfide minerals in the BIF-hosted FGS orebody.

Laser ICP-MS analyses demonstrate Au concentrations in FIAs trapped in V1, V2 and V4 veins indicate that not all Au was precipitated, and that therefore other ideal mechanisms for metal precipitation may have been achieved elsewhere as well. Further, future studies should involve analyzing sulfide minerals, particularly pyrite, in quartz veins of orebodies such as VQZ to determine their composition, and to have a straight comparsion of the fluid development together with the precipitation and mineralization event. Based on the obtained data of the present study we assume that pyrite in quartz veins may be depleted in trace elements since FIAs trapped in late-stage V4 veins show appreciable concentrations of As, Au, and Ag $\pm$ Pb $\pm$ Zn $\pm$ Cu (Fig. 9, Chapter 2), and late-stage BIF-hosted pyrites Py4 and Py5 display lower trace element contents compared to early- and main-stage pyrites Py2 and Py3 (Fig. A4, Chapter 3). In addition, multiple sulfur isotope studies, especially the $\delta^{33}S$-$\Delta^{34}S$ relation, indicate the tendency that the fluid/rock ratios from Py2 to Py5 decreases by an increasing $\delta^{33}S$ and $\Delta^{34}S$ values (Fig. 11, Chapter 3). This implies that sulfur is continuously buffered and exhausted via pyrite formation from Py2 to Py5.

In conclusion, Py2 and Py3 pyrite types represent the peak of the Archean gold mineralization event at the Cuiabá orogenic gold deposit, which is supported by geochemical and isotopic trends provided by LA-ICP-MS and multiple sulfur isotope analyses. In combination with the conducted fluid inclusion study, the FIA characteristics and quartz vein development may be related to the pyrite evolution, showing decreasing metal contents in the fluid and increasing tendencies in certain pyrite types and vice versa.

Chapter 5

Conclusions

The fluid inclusion and sulfide mineral study, both conducted at the Cuiabá orogenic gold deposit, support the following final considerations:

1) In general, the fluid inclusion study point out to the development of the quartz vein-associated VQZ ore body within two distinct hydrothermal pulses. The investigated ore body comprises a vein system constisting of V1 shear veins, V2 extensional vein (V1 and V2 with visible gold), and V3 extensional array and V4 extensional (late-stage) veins. Thereby, early-stage, anhedral Qz1 develops to a granoblastic Qz2, and a late-stage, euhedral Qz3 during the first hydrothermal pulse represented by V1, V2 and V3 veins. Late-stage V4 veins are interpreted to be related to the second hydrothermal pulse, where the anhedral Qz5 develops, bearing morphological and fluid inclusion characteristica similar to Qz1.

2) Microthermometric measurments, ion chromatography and LA-ICP-MS analyses on aqueous and aqueous-carbonic FIAs trapped in the different quartz types indicate a fluid signature of the ore-forming fluid responsible for the mineralized quartz veins of the VQZ ore body, which is typical for orogenic gold deposits, i.e., low- to moderate-salinity (4.0-10.0, up to 15 wt % NaCl equiv), presence of CO_2, CH_4, N_2 and minor HS^-. Intermittent phase immiscibility as well as heterogeneous entrapment resulting from intermittent partial mixing of two or more ore fluids may be considered as the principal fluid processes leading to the formation of the Cuiabá orogenic gold deposit.

3) It is clearly shown that trapped fluid inclusions do not represent the pristine fluid. Ion chromatography and LA-ICP-MS data in FIAs display the fluid-rock interactions between quartz veins, i.g. i) Na decreases in V2 relative to V1 and V3 veins; ii) Sr increases in V3 and V2 relative to V1; iii) K continously decreases from V1 to V4; and iv) Ca is relatively higher to Na and K concentrations in V2 in comparison to V1, V3 and V4. The Cuiaba orogenic gold fluids demonstrate distinct Cu, Zn and Pb enrichments in the FIAs of Cuiabá, which are similar to other deposits hosted in the RVGB (Lamego and Córrego do Sítio). These values, in the range of 100 to 1,000 ppm, may have been caused by interaction with i) metalliferous black shales; and ii) the (meta)sedimentary rocks that dominate the RVGB.

4) The fluid inclusion results provide an excellent opportunity to classify shear and extensional veins and help identify a true relative evolution of the different vein types in the orogenic gold deposits of the QF. The similar geochemical affinity of the Cuiabá veins, suggesting they are all part of the same hydrothermal

event. This event is characterised by two main pulses, with the first displaying changing physico-chemical parameters due to fluid-rock reactions and fluid dynamic processes. This particularly becomes apparent in the recorded Au concentrations of FIAs trapped in the main hosts for the mineralisation of the VQZ ore body (Qz1-V1 shear and Qz2-V2 extensional veins), but also of the Qz5-V4 late-stage veins, which may represent a paragenetically late and second Archaean hydrothermal pulse.

5) The sulfide mineral study identified five pyrite types: syngenetic, spongy Py1 (only in CP), porous, early-stage Py2 is made up of Py1 in CP, typically forms the central portion of pyrite grains in andesite and BIF., euhedral, main-stage Py3 appearing along pyrite borders and overgrows Py2, late stage Py4 and Py5 forming smooth euhedral grains in BIF.

6) LA-ICP-MS data indicate different TE signatures of pyrite types: Py1 has high As, Co, Ni, Pb and Ag concentrations, indicating syngenetic metal enrichments. Py2 shows high trace element concentrations with a large variability, which may be interpreted as unbuffered conditions and dissolution-reprecipitation reactions at this stage. Py2 and Py3 show an increase of Co and Ni, but a decrease of Au and As. Py4 is characterized by lower trace element concentrations; Py5 indicates an enrichment in As, Bi, Co, Ni and Pb.

7) Paragenetic evidence of timing and geochemical behavior of trace elements in early-, main-, and late-stage pyrite types in carbonaceous pelite, BIF and andesite indicate a five-stage evolution.

8) Multiple sulfur isotope data on pyrite show $\delta^{34}S$ values range from 1.78 to +6.90 ‰, $\Delta^{33}S$ from –2.28 to +1.73 ‰, and $\Delta^{36}S$ from –2.04 to +3.19 ‰. Noticeable are 1) Negative $\Delta^{33}S$ values for the syngenetic Py1 in carbonaceous pelite, 2) Only positive $\Delta^{33}S$ values for other pyrite types in all other host units, 3) Lack of negative $\delta^{34}S$ values for samples analyzed. These values may indicate that Py1 of the CP was deposited in a seawater environment (non-zero $\Delta^{33}S$), later mixed with mantle sulfur carrying a near-zero $\Delta^{33}S$ signature or alternatively a different sedimentary source with a positive $\Delta^{33}S$ (Py-CP). Early-, main- and late-stage hydrothermal pyrite types (Py2, Py3, Py4 and Py5) in BIF and andesite present a continuous process of crustal assimilation (only positive $\delta^{34}S$ and $\Delta^{33}S$ values).

Chapter 6

References (those used in the chapter 1)

Bühn, B., Santos, R.V., Dardenne, M.A., de Oliveira, C.G., 2012, Mass-dependent and mass independent sulfur isotope fractionation (δ34S and δ33S) from Brazilian Archean and Proterozoic sulfide deposits by laser ablation multi-collector ICP-MS. Chem. Geol. v. 312, p. 163–176.

Bierlein, F. P., and Crowe, D. E., 2000, Phanerozoic orogenic lode gold deposits: Gold, v. 13, p. 103-139.

Cabral, R.A., Jackson, M.G., Rose-Koga, E.F., Koga, K.T., Whitehouse, M.J., Antonelli, M.A., Farquhar, J., Day, J.M.D., Hauri, E.H., 2013, Anomalous sulphur isotopes in plume lavas reveal deep mantle storage of Archaean crust. Nature v. 496, p. 490–494.

Eiler, J.M., Graham, C., Valley, J.W., 1997, SIMS analysis of oxygen isotopes: matrix effects in complex minerals and glasses. Chem. Geol. v. 138, p. 221–244.

Farquhar, J., Bao, H., Thiemens, M., 2000, Atmospheric influence of earth's earliest sulfur cycle. Science v. 28, p. 756–758.

Farquhar, J., Wing, B.A., 2003, Multiple sulfur isotopes and evolution of the atmosphere. Earth Planet. Sci. Lett. v. 213, p. 1–13.

Farquhar, J., Johnston, D.T., Wing, B.A., 2007, Implications of conservation of mass effects on mass-dependent isotope fractionations: influence of network structure on sulfur isotope phase space of dissimilatory sulfate reduction. Geochim. Cosmochim. Acta v. 71, p. 5862–5875

Farquhar, J., Cliff, J., Zerkle, A.L., Kamyshny, A., Poulton, S.W., Claire, M., Adams, D., Harms, B., 2013, Pathways for Neoarchean pyrite formation constrained by mass-independent sulfur isotopes. Proc. Natl. Acad. Sci. v. 110, p. 17638–17643.

Goldfarb RJ, Baker T, Dube B, Groves DI, Hart CJ, Gosselin P (2005) Distribution, character, and genesis of gold deposits in metamorphic terranes. Econ Geol 100: 407-450

Groves DI, Goldfarb RJ, Gebre-Mariam M, Hagemann S, Robert F (1998) Orogenic gold deposits: a proposed classification in the context of their crustal distribution and relationship to other gold deposit types. Ore Geol Rev 13: 7-27

Hauri, E.H., Papineau, D.,Wang, J., Hillion, F., 2016, High-precision analysis of multiple sulfur isotopes using NanoSIMS. Chem. Geol. v. 420, p. 148–161.

Ireland, T.R., Schram, N., Holden, P., Lanc, P., Ávila, J., Armstrong, R., Amelin, Y., Latimore, A., Corrigan, D., Clement, S., Foster, J.J., Compston,W., 2014, Charge-mode electrometer measurements of S-isotopic compositions on SHRIMP-SI. Int. J. Mass Spectrom. v. 359, p. 26–37.

Johnston, D.T., 2011, Multiple sulfur isotopes and the evolution of earth's surface sulfur cycle. Earth-Sci. Rev. v. 106, p. 161–183.

Kerrich R, Fyfe B (1981) Archean precious-metal hydrothermal systems, Dome Mine, Abitibi Greenstone Belt. II. REE and oxygen isotope relations. Can J Earth Sci 16:440-458

Nesbitt, B. E., 1991, Phanerozoic gold deposits in tectonically active continental margins: Gold metallogeny and exploration, p. 104-132.

Phillips, G. N., and Groves, D. I., 1983, The nature of Archaean gold-bearing fluids as deduced from gold deposits of Western Australia: Journal of the Geological Society of Australia, v. 30, p. 25-39.Stern, R.A., 2008, An introduction to secondary ion mass spectrometry (SIMS) in geology. Mineralogical Association of Canada Short Course v. 41, p. 1–18.

Ridley, J. R., Diamond, L. W., 2000, Fluid chemistry of orogenic lode gold deposits and implications for genetic models: Review Economic Geology v. 13, p. 141-162

Ushikubo, T.,Williford, K.H., Farquhar, J., Johnston, D.T., Van Kranendonk,M.J., Valley, J.W., 2014, Development of in situ four-isotope analysis with multiple Faraday cup detectors by SIMS and application to pyrite grains in a Paleoproterozoic glaciogenic sandstone. Chem. Geol. v. 383, p. 86–99.

Whitehouse, M., 2013, Multiple sulfur isotope determination by SIMS: evaluation of reference sulfides for Δ33S with observations and a case study on the determination of Δ^{36}S. Geostand. Geoanal. Res. v. 37, p. 19–33.

Yardley BWD, Bodnar RJ (2014) Fluids in the continental crust. Geochem Perspect 3: 1-127